DOCTORAL DISSERTATION

博士論文

CONSTITUTIVE MODEL FOR CRUSHBALE SOILS AND ITS APPLICATION TO GEOTECHNICAL PROBLEMS

破壊性土の構成則と地盤工学の諸問題への適用

Yokohama National University

Graduate School of Urban Innovation

国立大学法人横浜国立大学大学院都市イノベーション学府

NGUYEN PHAM QUANG VU

グェン ファム ワン ヴォー

September 2018

2018 年 9 月

CONSTITUTIVE MODEL FOR CRUSHABLE SOILS AND ITS APPLICATION TO GEOTECHNICAL PROBLEMS

破壊性土の構成則と地盤工学の諸問題への適用

by

NGUYEN PHAM QUANG VU

グェン ファム ワン ヴォー

A Dissertation Submitted to the Graduate School of Urban Innovation, Yokohama National University in Partial Fulfillment of the Requirement for the Degree of

Doctor of Engineering

Yokohama National University, Graduate School of Urban Innovation

国立大学法人横浜国立大学大学院都市イノベーション学府

Examination Committee

Associate Professor, Dr. Mamoru KIKUMOTO (Chair)

Professor, Dr. Kimitoshi HAYANO

Professor, Dr. Hitoshi YAMADA

Associate Professor, Dr. Ying CUI

Associate Professor, Dr. Toshiyasu UNNO

Assistant Professor, Dr. Hiroyuki KYOKAWA

September 2018

2018 年 9 月

ABSTRACT

It has been long recognized that particle crushing leads to a significant change in the properties of sensitive crushable soil. Thus, it is essential to study the deformation and failure of ground exhibiting particle crushing. The aims of this study are (1) to establish a mutual relationship between particle size distribution curve and grading index (2) to develop a new elastoplastic constitutive model considering particle crushing using grading index I_G and its evolutional rule (3) to analyze the deformation and failure of ground exhibiting particle crushing using the proposed model.

In the first part of this research, an elastoplastic constitutive model considering particle crushing . Next, the effect of particle crushing was implemented to the critical state soil model (Roscoe, Schofield et al. (1963), Muir Wood (1990)) by incorporating the grading index I_G and its evolution law due to crushing. Finally, the model was extended to incorporate the effect of density on the stress-strain characteristics by employing the concept of subloading surface (Hashiguchi and Ueno (1977)). The validation of the proposed model via a number of experimental laboratory triaxial tests under isotropic consolidation, consolidated undrained, and consolidated drained conditions has revealed the good performance of the model to capture the response of crushable soil. Furthermore, the effect of fine contents on the behavior of uncrushable soil was also discussed by our model. The advantage of our model is not only shearing and compression effect, but consolidation effect was also considered to the initiation of particle crushing. Also, the model can be used to study the behavior of both crushable and uncrushable soils.

The second part of this study is to numerically analyze the deformation and failure of ground exhibiting particle crushing. To solve the non-linear equations with boundary conditions, the widely used numerical technique, Finite Element Method (FEM) was chosen. However, to overcome the volumetric locking problem in FEM with low order elements when dealing with critical state model, modified B-bar method (Commend, Truty et al. (2004)) was applied in this paper. The first practical application in this study is the analysis of bearing capacity of strip footing on Dogs Bay sand, a crushable soil. Parametric studies were conducted to evaluate the effects of parameters of the soil model to the bearing capacity of strip footing. It was found that (1) with 15 cm settlement, bearing capacity of strip footing slightly reduced (~10%) due to particle crushing in case of Dogs Bay sand, (2) the less crushing effect was observed for the larger the width of foundation. (3) with a specific allowable settlement, the effect of crushing on bearing capacity decreased when the footing size increased. (4) scale effect was also observed in our simulation; however, the ultimate bearing capacity was not observed in the simulation of Dogs Bay sand. (5) when assuming the bearing capacity under a certain settlement was “ultimate” bearing capacity, one interesting finding was that (the bearing capacity factor N_γ – strip footing width B) line of crushable soil in (log_{10}-log_{10}) scale was a straight line being shifted

downward from the (N_γ-B) line of uncrushable soil. The second application is the analysis of passive and active earth pressure on Dogs Bay sand, a crushable soils. From the simulation results, it is observed that the occurrence of particle crushing significantly reduced passive earth pressure coefficient, around 25% (from 7.4 to 5.8, to be more specific). On the other hand, active earth pressure is not much affected by particle crushing phenomenon.

ACKNOWLEDGEMENTS

Firstly, I would like to express my sincere gratitude to Associate Professor Mamoru Kikumoto for the opportunity to work in the Civil Engineering Department of Yokohama National University, for his supervision, guidance and support during my graduate study. He always inspires me to do research with immense passion through thoughtful discussions as well as innovative ideas. His guidance helped me in all the time of research and writing of this thesis.

To Associate Professor Kikumoto, Professsor Konagai and Associate Professor Ying Cui, I would like to express my deepest appreciation for your assistance and guidance during my study. I would like to extend my sincere appreciation to all committee member: Professor Hitoshi Yamada, Associate Professor Toshiyasu Unno, Assistant Professor Hiroyuki Kyokawa for their comments and suggestions to improve the quality of this thesis.

I would like to give special thanks to the financial support from the Ministry of Education, Culture and Sport, Science and Technology, Japan during my Master and PhD courses at Yokohama National University.

My special thanks to Dr. Keita Nakamura for guiding me during me study about constitutive model, Finite Element Method as well as programming languages. We shared a lot of good experiences not only in academic research but also in daily life for almost five years in the same laboratory.

I am also grateful to all my friends at Yokohama National University for their direct and indirect help. My student life has not been this colorful without them.

Finally, I would like to give special thanks to my wife, Thao, for her love, understanding and support during these 5 years at Yokohama. We both are grateful to our parents for their love and encouragement during my graduate study.

TABLE OF CONTENTS

LIST OF FIGURES

LIST OF TABLES

Chapter 1 : Introduction

1.1 Research background

1.1.1 Particle crushing effect on geotechnical structures

There are a number of geotechnical structures in which soil beneath them exhibit particle crushing, such as highway embankments, earth dam (Tatsuoka (1991), Hattamleh, Al-Deeky et al. (2013)), or driven piles (Datta, Gulhati et al. (1980), Poulos and Chua (1985) , Alba and Audibert (1999)). Several examples of construction sites exhibiting particle crushing are (a) cone penetrometer test on carbonate soil in Dubai (Lees, King et al. (2013)), (b) piled foundations on carbonate soil at the North West Shelf, Australia (Senders, Banimahd et al. (2013)), etc. During their lives of operation or construction stages, soil particles can be broken into smaller ones due to large external forces or weak structure of the soil (Figure 1-1). Therefore, the initial physical properties of soil supporting these structures will change significantly. This crushing will greatly affect the soil strength and its stress-strain behavior at the elementary level (Hardin (1985)) because the soil after being crushed can significantly change its physical behavior. The increased level of crushing leads to a decrease in soil's peak strength and a decrease in soil dilation angle (Hattamleh, Al-Deeky et al. (2013)). The variation in the original engineering properties can put the stability of such structures in danger. Hence, a proper consideration of particle crushing effect in soil properties of such geotechnical structures is vitally important to enable a safe design.

There are two main kinds of crushable soils: the first one is coarse-grained volcanic soils, for instance; volcanic soils from Hokkaido and Kyushu (Miura, Yagi et al. (2003)); the second one is carbonate soil, for instance, Dogs Bay sand from the west coast of Ireland is a highly crushable marine sediment. The Dogs Bay sand contained highly angular particles with a 94% carbonate content (Golightly and Hyde (1988)).

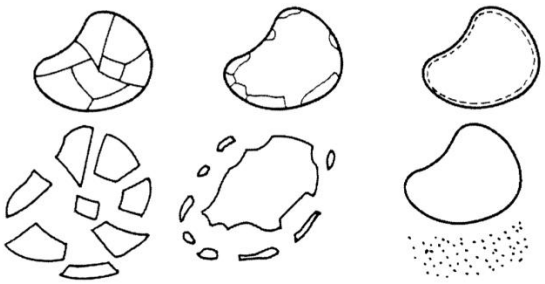

Figure 1-1: Different modes of grain breakage.(Daouadji et al, 2001)

1.1.2 Grading index I_G

For a soil with an initial single sized grading, after being loaded to a large magnitude of s train, the initial PSD will gradually change to its limiting PSD in which the soil is not be able to be crushed anymore (for instance, Dog's Bay sand in Figure 1-2). The key purpose of the study of particle breakage is to determine the degree of crushing that the particles are exhibiting. Thus, there have been many researchers attempting to propose a good grading index. There are two primary kinds of crushing indices in the literature, accounting for a particular particle size or the whole PSD. This part briefly reviews the existing grading indices and explains the reason why we choose grading index I_G Muir Wood (2007) for our model.

Lee and Farhoomand (1967) recommended the "relative crushing" index B_{15} which is the ratio of D_{15i}/D_{15a}, where D_{15i} and D_{15a} represent D_{15} size before and after crushing, respectively. Later, Lade, Yamamuro et al. (1996) proposed a similar index, B_{10}. Marsal (1967) defined breakage index B_M as the maximum percentage difference between the PSD curves before and after crushing at one certain diameter. Although these indices are easy to use, it is only able to observe a particular point on the PSD which is difficult to grasp the whole picture of crushable soil. Thus, a better approach is to use the parameter that can describe the whole picture of PSD.

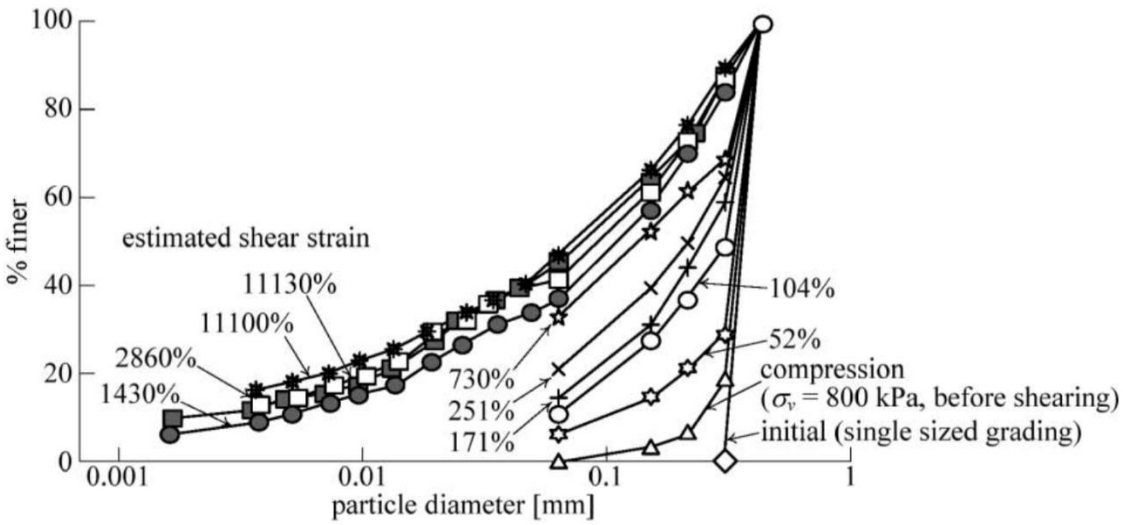

Figure 1-2: Evolution of particle size distribution in ring shear tests on Dog's Bay sand (after Coop et at., 2004)

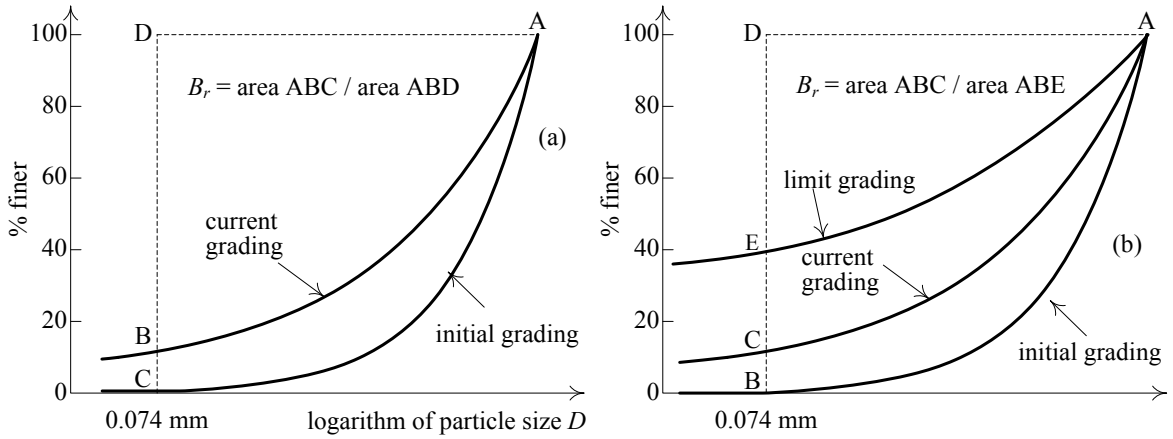

Figure 1-3: a) Definition of grading index B_r. b) Definition of the modified grading index B_r

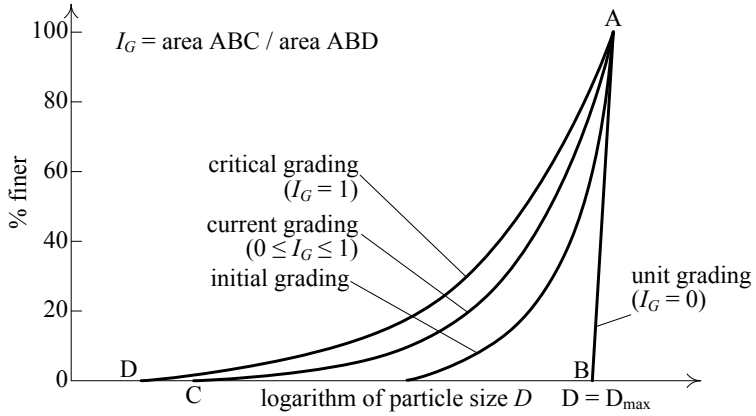

Figure 1-4: Definition of grading index I_G.

Hardin (1985) proposed a relative breakage index B_r which is described in Figure 1-3a. The value of B_r corresponding to the initial grading (AC curve), and the critical grading with maximum crushing level (AD line) are set to be 0 and 1, respectively. The value of B_r at any other soil states ($0 < B_r < 1$) is determined as the ratio between ABC area and ACD area in Figure 1-3a:

$$B_r = \frac{S_{ABC}}{S_{ACD}} \tag{1-1}$$

Acknowledging that in reality, there is no PSD curve corresponding to $B_r = 1$ in the way that Hardin proposed, and that the PSD should be bounded by a limiting distribution of PSD, Einav (2007) proposed a modified version of B_r based on the alternatively breakage potential (B_r equals the ratio of ABC area over ABE area in Figure 1-3b)

A lot of researchers have utilized B_r index to measure the level of crushing. However, B_r index is always equal to 0 for the initial soil state, regardless of different PSDs.

Thus, the disadvantage of B_r is that it is not possible to estimate the state of soil PSD based on only B_r index. Muir Wood (2007) proposed a grading index I_G whose definition is clarified in Figure 1-4**.** Similar to the modified version of B_r index Einav (2007a), Wood assumed that for each kind of

soil, the PSD gradually changes from the unit grading (vertical line AB) to a critical grading (AD curve) that the soil tends to not exhibit any further significant crushing. In other words, during the loading process, each kind of soil is assumed to gradually reach its fractal critical PSD in which the soil will not exhibit any further crushing, irrespective of its initial grading. For unit grading and the critical grading, I_G is set to be 0 and 1, respectively. Then, the crushing index I_G corresponding to any arbitrary soil state ($0< I_G <1$) is defined as:

$$I_G = \frac{S_{ABC}}{S_{ABD}} \tag{1-2}$$

According to the definition of I_G, the state of PSD of soil will be the same as long as they possess the same value of I_G, regardless of their initial grading. Thus, it is able to observe the soil's PSD state based on grading index. Therefore, in this research, the grading index I_G will be used in the formulation of the soil model considering particle crushing.

1.1.3 Grading indices and elastoplastic soil constitutive model considering particle crushing

The particle size distribution (PSD), which is one of the most widely measured properties of soil in laboratory tests, has been acknowledged to significantly control soil's stress-strain relationship (Lade, Yamamuro et al. (1996), McDowell and Bolton (2000)). However, few models have incorporated the grain size evolution to consider particle crushing phenomenon. Yao, Yamamoto et al. (2008) developed a constitutive model considering crushing on sand based on Cam Clay model and a hardening parameter which is a revised plastic volumetric strain, depending on mean stress and volumetric plastic strain and crushing stress. Even though this model can capture crushable soil's stress-strain behavior as well as the dilatancy of soil under different levels of stress and strain, there is no consideration of PSD in his model. Einav (2007a)proposed a modified version of the breakage index B_r, which was originally proposed by Hardin (1985)and then used it to formulate a crushing model in the framework of thermodynamics. Unfortunately, it is unable to predict the PSD of soil based on B_r grading index because the initial B_r is always 0 irrespective of its initial PSD. Later, Kikumoto, Wood et al. (2010) extended the Severn Trent sand model (Gajo and Muir Wood (1999)) with an additional grading index parameter I_G to take into account the effect of particle breakage due to the evolution of PSD. However, the mutual relationship between grading index I_G and particle size distribution curve has not been established. Also, the effect of compression and shearing on crushing were considered separately, which complicated the understanding of the model. Furthermore, the performance of Severn Trent sand based soil model considering crushing has not been validated with experimental results.

1.1.4 Critical state framework and particle crushing

Based on experimental tests by Coop (1993) on Dogs Bay sand considering isotropic compression test (Figure 1-5) and critical state after shearing (Figure 1-6), it can be seen that the state boundary surface, which contains the NCL and CSL, does exist for sand. Sasitharan, Robertson et al. 1994, also found that state boundary surface exists for sand.

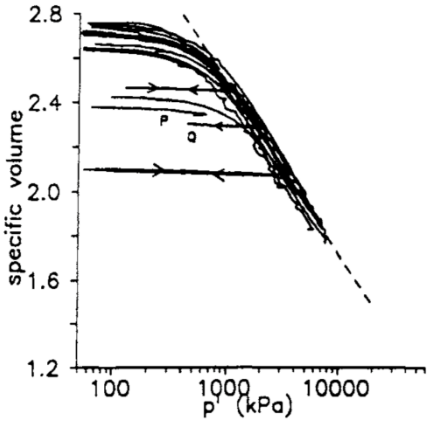

Figure 1-5. Isotropic compression data of Dogs Bay sand (after Coop, 1993)

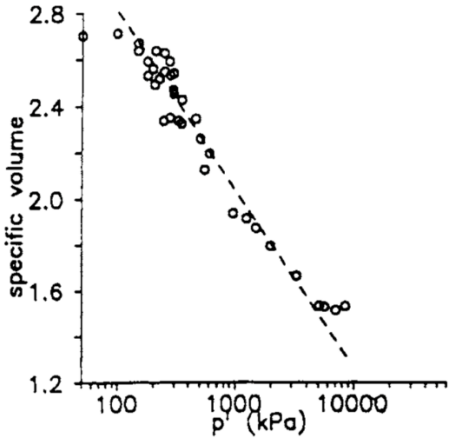

Figure 1-6 Critical state of Dogs Bay sand (after Coop, 1993)

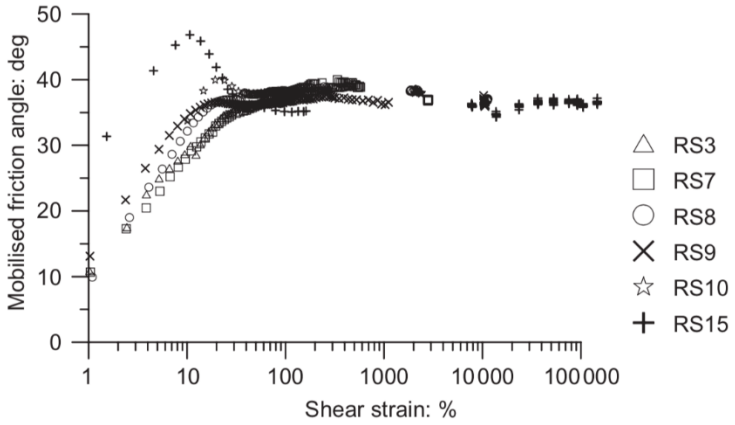

Figure 1-7: Evolution of mobilized angle of shearing resistance with shear train of ring shear test (after Coop, 2004)

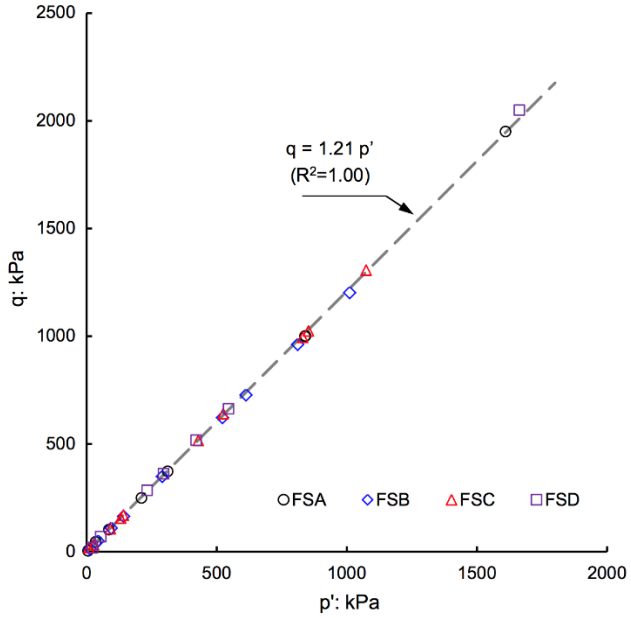

Figure 1-8: Locus of critical states in stress space (Yang and Luo, 2018) (FSA, FSB, FSC, FSD are the same soil with different gradings)

Particle crushing appears to have little effect on critical state friction angle (Coop (1990), Ghafghazi, Shuttle et al. (2014)). Also, the mobilized friction angle of shearing resistance is observed to be constant in ring shear test in Figure 1-7 (Coop, 2004). Similarly, Yang and Luo (2018) found in triaxial test with Fujian sand that the critical state friction angle is constant with different grading levels (for the same soil). Thus, critical state framework can be applied to particle crushing problems based on the assumption that critical state is reached in triaxial apparatus represent a balance between the volumetric compression by particle crushing and volumetric dilation arising from particle rearrangement, as suggested by Chandler (1985).

Regarding the movement of CSL due to particle crushing, it is observed that crushing caused a downward parallel shift in CSL in e-log(p') space (Daouadji, Hicher et al. (2001), Muir Wood and Maeda (2007), Ghafghazi, Shuttle et al. (2014)). In this research, a critical state based soil constitutive model is developed with the assumption that the critical state line and the limited isotropic compression line are downward parallel shifted as crushing occurs. These downward movement is corresponding to the evolution of particle size distribution curve via the changing of grading index I_G (Muir Wood (2007)). Then, the performance of the model is validated with the experimental results of Dogs Bay sand experimental elementary tests. The advantages of our proposed constitutive model are that (1) it can consider both shearing and consolidation in crushing phenomenon (2) it can be easily implemented into FEM code to simulate geotechnical structure problems.

1.1.5 Finite element method and volumetric locking issue in 2D plane strain condition

The numerical method FEM is widely used among engineers due to its high accuracy and stability. Unfortunately, when dealing with incompressible materials, the displacement based FEM formulation may exhibit an unrealistically stiff behavior. Similarly, elastoplastic soil constitutive models in which constant volume is predicted at critical state also witness this unrealistic stiffness in FEM. This is usually known as "volumetric locking" phenomenon. Volumetric locking problem occurs due to Gauss integration, a programming-friendly numerical integration technique in FEM. This volumetric locking occurs when a finite element mesh uses low order elements, such as constant strain triangle elements, or 4 nodes isoparametric quadrilateral element (Quad4). Zienkiewicz, Taylor et al. (1971) proposed the reduced integration method to resolve this volumetric locking. The idea of reduce the integration is simple: because the fully integrated elements cannot make the strain field volume preserving at all the integration points, it is tempting to reduce the number of integration points so that the constraint can be met. The slight loss of accuracy is counteracted by the improvement in approximation to real life behavior. However, this uniform-reduced integration may lead to the rank deficiency of the stiffness matrix (Hughes, Cohen et al. (1978)). Thus, the selective reduced integration (SRI) was proposed to overcome this rank deficiency problem (Hughes, Cohen et al. (1978)). The premise in SRI procedure is to use reduced integration only for the part of the stiffness that locks volumetric stiffness. While the SRI method is very efficient for isotropic elastic materials, in which it is easy to split up the stress into deviatoric and dilational parts, it is not straightforward to apply for the elastoplastic model in which the volumetric and deviatoric parts of the constitutive mode are coupled. An alternative method for SRI is B-bar method developed by Hughes (1980). Similar to SRI, the B-bar method works by treating the volumetric and deviatoric parts of the stiffness matrix separately. Instead of separating the volume integral into two parts, however, the B-bar method evaluates separately the shear and volumetric contribution of strain to element stiffness by modifying the definition of the strain in the element. In this method, shear strain is calculated with full integration as the normal FEM;

however, the volumetric strain is calculated with one order lower than that of standard FEM. In the plane strain condition, because B-bar method only satisfies the condition of zero strain in the out-of-plane direction in a weak sense, it is essential to modify B-bar method to strictly satisfy the plane strain condition. In this research, the modified B-Bar method (Commend, Truty et al. (2004)) is used as a countermeasure to volumetric locking in FEM.

1.1.6 Strip footing bearing capacity on crushable soil

One example of the application of our proposed model is to analyze the bearing capacity of footings on crushable soils. The bearing capacity analysis foundation is one of the most significant problems in geotechnical engineering. The bearing capacity equations of the widely used pile foundation and strip footing have been long established. The equation for estimating the bearing capacity of pile foundations is the summation of skin friction and pile end-bearing capacity. The famous equation for estimating the ultimate bearing capacity of shallow strip foundation by Terzaghi (1944) is the summation of three distinct components: (1) the cohesive component of shear strength of the soil, (2) the surcharge pressure adjacent to the foundation, (3) the frictional resistance of the soil beneath the foundation. However, these equations do not consider crushing phenomenon in soil particles.

In the context of bearing capacity of foundations, the applied pressures can cause the particle crushing phenomenon in soil particles, especially for the soils that are sensitive to crushing as mentioned in Section 1.1.1. This particle crushing phenomenon will result in the reduction of the footing's bearing capacity. Thus, geotechnical engineers may jeopardize the safety of strip foundation in crushable soil areas. Several studies have attempted to consider particle crushing on the pile end-bearing capacity (Zhang, Nguyen et al. (2013), Kuwajima, Hyodo et al. (2009), Yasufuku and Hyde (1995)). These studies analyzed the reduction of end-bearing capacity due to particle crushing. Nevertheless, to the knowledge of the authors, there has been no or few studies considering the particle crushing effect on the bearing capacity of shallow foundations. Therefore, the aim of this study is to perform the numerical analysis of the particle crushing effect on the bearing capacity of strip footings.

1.1.7 Lateral earth pressure coefficient on crushable soils

The second application of our proposed model is to analyze the effect of particle crushing phenomenon on the analysis of active and passive earth pressure coefficients, K_a and K_p, respectivrely, on crushable soils. This is also a fundamental problem in geotechnical engineering. The famous equations for estimating active and passive earth pressures has been proposed by Rankine. However, his solution didn't consider particle crushing phenomenon. In the case of passive earth pressure, under high stress, the soil particle may be crushed and the soil strength reduced. I expected that this will lead

to the reduction of K_p,. The active earth pressure K_a, on the other hand, is not expected to suffer a significant effect of crushing.

Even though, experimental testing is an attractive approach to study the effect of particle crushing to strip footing's bearing capacity and lateral earth pressure coefficients; experimental validation is not a straightforward way because 1) it does not provide a simple way to visualize the evolution of this phenomenon. On the other hand, computer simulation can show this visualization. 2) the study of the effect of particle crushing on bearing capacity of foundations, will necessarily require the experimental tests of one type of uncrushable soil and another soil with the same set of parameters as this uncrushable soil, but exhibiting crushing phenomenon under loading. Apparently, this requirement cannot be satisfied in practice. This study, therefore, performed the numerical analysis to study the effect of particle crushing on 1) strip footing bearing capacity 2) lateral earth pressure coefficients.

1.2 Research objectives

The primary objectives of this research are (1) to develop a simple constitutive soil model considering particle crushing, and (2) to analyze the bearing capacity of strip footing on crushable soil based on the proposed model: The steps to obtain the above mentioned objectives are follows:

1. To establish the mutual relationship between PSD curve and grading index I_G. To do this, we propose a simple method to obtain the PSD curve based on the current value of grading index I_G. (*Chapter 2*)
2. To develop an elastoplastic constitutive model for crushable soils based on critical state framework by incorporating the evolution of grading index I_G due to particle crushing. (*Chapter 2*)
3. To validate the proposed model based on elementary tests of Dogs Bay sand, a crushable soil, by triaxial tests under isotropic consolidation, consolidated undrained, and consolidated drained conditions. (*Chapter 3*)
4. To overcome the volumetric locking problem in FEM with Quad4 element in 2D plane strain condition by employing the modified B-bar method. (*Chapter 4*)
5. To analyze the strip footing bearing capacity on crushable soils based on our proposed constitutive model for crushable soil and FEM with modified B-bar approach (*Chapter 5*)
6. To analyze the effect of particle crushing on the active and passive earth pressure coefficients on crushable soils based on our proposed constitutive model and FEM method. (*Chapter 6*)

1.3 Outline of dissertation

Chapter 1 Introduction

Research background and research objectives of this study are described in this chapter including the outline of this dissertation

Chapter 2: A constitutive model for soil considering particle crushing

Chapter 2 explains the principle concepts used to develop the elastoplastic constitutive model for crushable soils. Firstly, an overview of the available grading indices is presented, and appropriate grading index is chosen for our model formulation. Then, a simple but effective method to obtain the PSD corresponding to a value of grading index is proposed. This method clarifies the mutual relationship between PSD and grading index. After that, the formulation of the particle crushing constitutive model in the framework of critical state theory utilizing the evolution of PSD due to crushing is described in detail.

Chapter 3: Validation of soil constitutive model considering particle crushing

In this chapter, the validation of the proposed model with experimental elementary tests and the parametric calibration of material parameters governing the crushing behavior is presented. Although the model is formulated in a simple way, it can not only capture stress-strain behavior of uncrushable soils but also can be used to observe the evolution of PSD curve. The parametric studies and parameter calibration is also presented in this chapter

Chapter 4: Volumetric locking problem in FEM and its countermeasures

When dealing with critical state soil model, FEM with low order elements may face volumetric locking problem, which leads to the inexact solution. Thus, this section reviews the characteristics of volumetric locking in FEM and its countermeasures including reduced integration, selective reduced integration, B-bar method. Finally, modified B-bar method, which is an appropriate method to deal with volumetric locking problem in 2D plane strain is described in detail. Also, the detail formulation of the modified B-bar method approach for Quad4 element is presented. The performance of FEM with the modified B-bar is validated in the appendix. There are two validation examples in this section including the beam bending problem and the strip footing bearing capacity with VonMises yielding criteria.

Chapter 5: Analysis of strip footing bearing capacity on crushable soil

Chapter 5 presents a numerical study of the strip footing bearing capacity on Dogs Bay Sand, a crushable soil, is conducted by using our particle crushing model and FEM with B-bar method. The parametric studies are also conducted to study the effect of material parameters to the strip footing bearing capacity. The scale effect of the calculation of bearing capacity of strip footing is also discussed in Chapter 5.

Chapter 6: Active and passive earth pressure coefficient analysis on crushable soils

This chapter studies the effect of particle crushing on the analysis of active and passive earth pressure coefficients analysis. In the first part of this chapter, FEM code is validated by comparing the analytical result of Rankine with the numerical simulation using Drucker-Prager model, with the parameters calibrated to be the same as Mohr Coloumb yield criteria under plane strain condition. Then, the developed soil model considering particle crushing is implemented to this FEM code.

Chapter 7: Concluding remarks and future research

Chapter 6 concludes the substantive findings and novelty of this research and provides the prospects for future research.

1.4 Notations and symbols

As for the notations and symbols, bold letters denote vectors and matrices; "·" denotes an inner product of two vectors (e.g., $\mathbf{a} \cdot \mathbf{b} = a_i b_i$) or a single contraction of adjacent indices of two tensors (e.g., $(\mathbf{c} \cdot \mathbf{d})_{ij} = c_{ik} d_{kj}$); ":" denotes an inner product of two second-order tensors (e.g., $\mathbf{c}: \mathbf{d} = c_{ij} d_{ij}$) or a double contraction of adjacent indices of tensors of rank two and higher (e.g., $(\mathbf{e}: \mathbf{c})_{ij} = e_{ijkl} c_{kl}$); $\otimes$ denotes a tensor product of two vectors (e.g., $(\mathbf{a} \otimes \mathbf{b})_{ij} = a_i b_j$) or a tensor product of two second-order tensors (e.g., $(\mathbf{c} \otimes \mathbf{d})_{ijkl} = a_{ij} b_{kl}$); "$\| \ \|$" denotes the norm of a first-order tensor (e.g., $\|\mathbf{a}\| = \sqrt{\mathbf{a}: \mathbf{a}} = \sqrt{a_i a_i}$) or a second-order tensor (e.g., $\|\mathbf{c}\| = \sqrt{\mathbf{c}: \mathbf{c}} = \sqrt{c_{ij} c_{ij}}$); $\mathbf{1}$ is the second-order identity tensor; $\boldsymbol{I}$ is the fourth-order identity tensor $\left(I_{ijkl} = \frac{1}{2}\left(\delta_{ik}\delta_{jl} + \delta_{il}\delta_{jk}\right)\right)$; "$\dot{}$" denotes the time derivative; and the subscript zero denotes the initial state (e.g., e_0 = initial void ratio).

Chapter 2 : A Constitutive Model for Soil Considering Particle Crushing

2.1 Grading index and particle size distribution curve

2.1.1 Mutual relationship between particle size distribution curve & grading index I_G

From the definition of grading index, I_G the initial value of I_G can be determined from the current PSD and the assumption of the critical PSD, unit PSD for a particular soil. This section presents a simple method to obtain the mutual relation between PSD and I_G. In other words, from a single value of I_G obtained in the simulation during loading processes, the corresponding PSD can also be obtained automatically by our proposed method.

Due to the importance of PSD in the study of granular material, a lot of researchers have made efforts to propose a number of PSD equations. For example, Andreasen and Andersen (1930) proposed an equation describing the PSD grading down from the maximum diameter to a diameter equal to zero as follows:

$$f(D) = \left(\frac{D}{D_{max}}\right)^n \tag{2-1}$$

where D is particle diameter, $D_{max}$is the maximum particle diameter, n is a constant parameter. The Equation 2-1 followed fractal particle size distribution with the dimension of n (Tyler & Stephen (1992))

In an attempt to better describe the curvature of PSD, Jaky (1944) proposed the equation of PSD as:

$$f(D) = \exp\left[-\frac{1}{p^2} ln\left(\frac{D}{D_0}\right)^2\right] \tag{2-2}$$

in which D_0 = 2mm and p is a constant parameter.

Recognizing that there is a limited minimum diameter of PSD for each kind of granular soil in practical situations, Dinger and Funk (1994) came up with a modified version to account for the minimum particle size (D_{min}):

$$f(D) = \frac{D^n - D_{min}^n}{D_{max}^n - D_{min}^n} \tag{2-3}$$

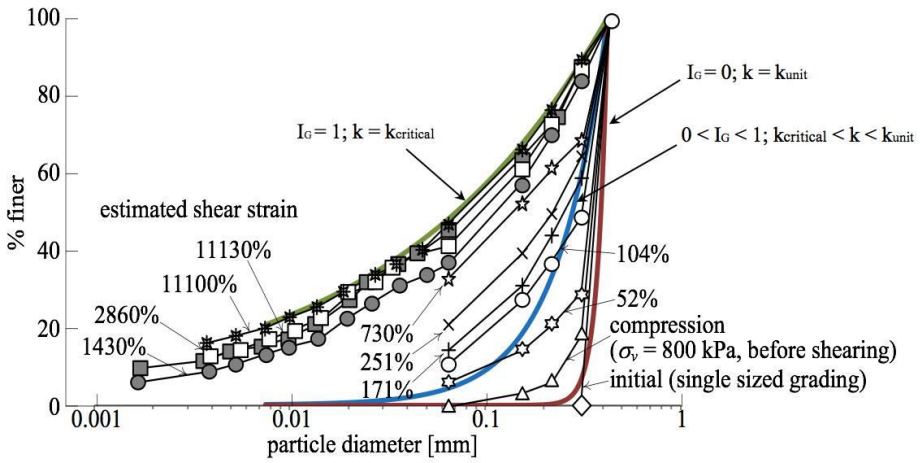

Figure 2-1: A comparison between particle size distribution curve by experimental test (Coop, 2004) and by using Eq. (2-4)

Table 2-1: Material parameters for PSD curve

D_{max}	0.425
k_{unit}	20
$k_{critical}$	0.9

To take the advantage of the preceding formulas, we proposed a simple equation for PSD considering both D_{max}, D_{min} and a good curvature. Furthermore, to consider the practical experiment tests in which the minimum size of the particle is controlled by the sieve's size, we introduced a modified form of the PSD equation by Jaky (1944) but further considering $D_{max}, D_{min-limit}$:

$$f(D,k) = \exp\left[k log_{10}\frac{D}{D_{max}}\right]; D = [D_{min-limit}, D_{max}] \quad (2\text{-}4)$$

in which the variable k denotes curvature coefficient of PSD. Particle diameter D ranges from the maximum diameter D_{max} of PSD, to the minimum size $D_{min-limit}$ of PSD limited by the experiment of sieve analysis. Acknowleged that D_{max} and $D_{min-limit}$ are constants in this equation, and PSD is just a function of the coefficient of the curvature of PSD and particle diameter. Our proposed equation for PSD is illustrated with the PSD of Dogs Bay Sands tested by Coop, Sorensen et al. (2004) as in Figure 2-1 with the material parameters for PSD curve described in Table 2-1. In chapter 5 of this thesis, we will also use Dogs Bay Sand for our model validation.

Notice that Eq. (2-4) can be rewritten as:

$$f(D,k) = \left(\frac{D}{D_{max}}\right)^{k log_{10} e}; D = [D_{min\_limit}, D_{max}] \quad (2\text{-}4a)$$

Thus, we assumed that our proposed PSD is always obey to the fractal distribution. Because fractal distribution has the form $\left(\frac{D}{D_{max}}\right)^{3-d}$, d is the dimension of fractal distribution. Our proposed equation

has a dimension of $(3 - klog_{10}e)$ during loading process. So, we assumed the fractal distribution rule for PSD during the whole process of loading, not just the critical PSD.

Based on curve fitting method, it is easy to obtain two constant parameters $k_{critical}$ and k_{unit}, corresponding to the curvature coefficients of critical PSD and unit PSD for each kind of soil, respectively.

Grading index I_G, as explained in the previous section, is defined by three different particle size cumulative functions: the current, unique, and ultimate cumulative functions as follows:

$$I_G = \frac{S(k_{current}) - S(k_{unit})}{S(k_{critical}) - S(k_{unit})} \tag{2-5}$$

where S is the area of the segment which is defined by integrating the area of cumulative function over the $log_{10}\, D$ scale,

$$S = \int_{D_{min}}^{D_{max}} f(k, D) d(\log_{10} D) \tag{2-6}$$

Note that when $k = k_{critical}$, $I_G = 1$; $k = k_{unit}$, $I_G = 0$. When $k_{critical} \leq k \leq k_{unit}$, S is the area of the segment between the PSD and x-axis form from D_{min} to D_{max}. Therefore, $S(k_{unit})$ and $S(k_{critical})$ are known values.

Substituting Eq. (2-4) into Eq. (2-6) , we can derive the equation for S as follows:

$$S = \frac{1}{k}\left[1 - exp\left(klog_{10}\frac{D_{min}}{D_{max}}\right)\right] \tag{2-7}$$

The current value of k can be numerically obtained by using bisection algorithm from Eqs. (2-5) & (2-7). Finally, from the obtained current k, the current PSD is readily to be plotted. Until now, the mutual relation between I_G and PSD curve has been clarified. The initial value of I_G can be determined from the initial PSD. Later, the variation of I_G can be used to check the variation of PSD. This mutual relationship is particularly useful in studying the behavior of crushable soils.

For example, in the 1D compression test, a crushable soil with material properties described in Table 2-2 after exhibiting a large compressive stress, the occurrence of soil particle crushing results in the changing of PSD. This variation of PSD leads to a change in the grading index I_G. In turn, the new value of I_G can be used to plot the new PSD (see Figure 2-2). Thus, during the loading process, we can not only observe stress-strain relationship of soil, but also, the evolution of PSD by using this method.

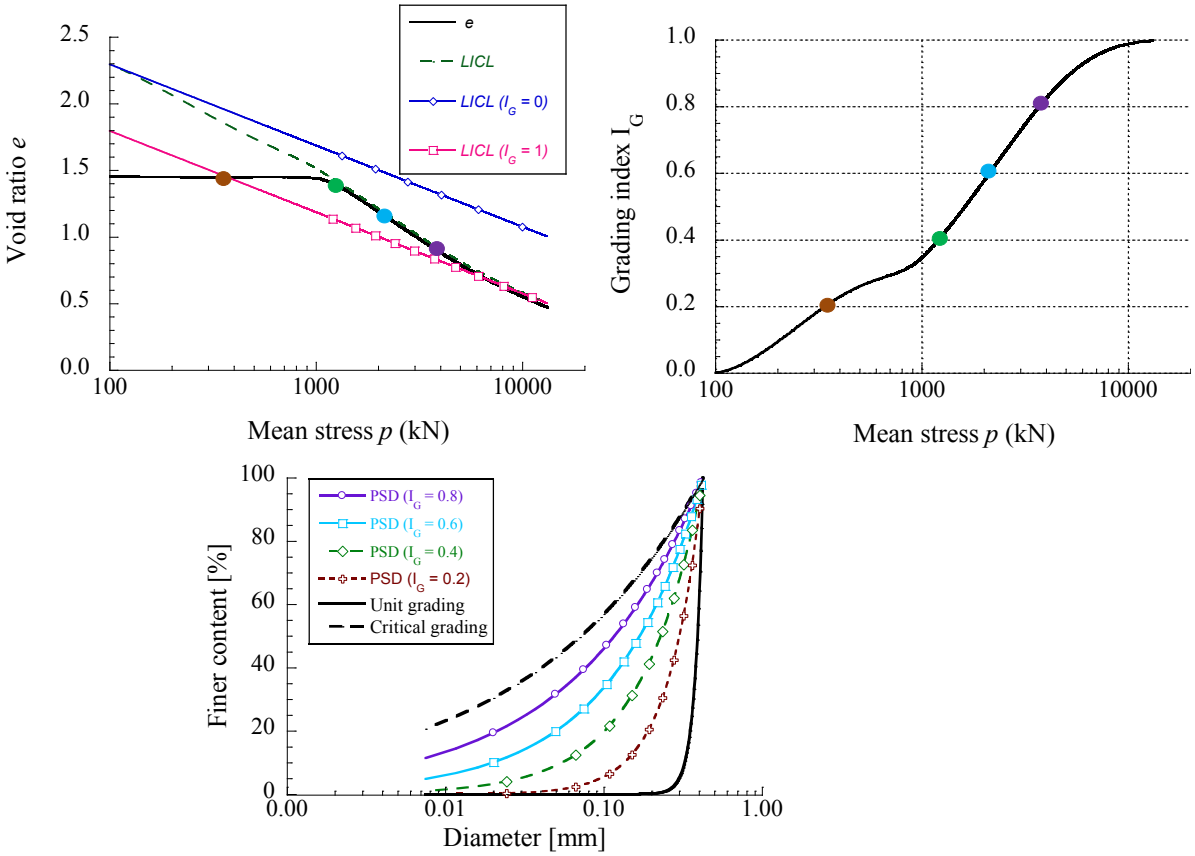

Figure 2-2 Isotropic consolidation of crushable soil and its variation of PSD & grading index I_G

Table 2-2: Material parameters of crushable soil

Parameter	Description	Classification	Value
λ	Compression index		0.265
κ	Recompression index		0.0015
N	Specific volume on NCL at p = 98 kPa	Modified Cam Clay	1.8
M	Critical stress ratio		1.65
ν	Poisson ratio		0.2
a	Parameter controlling density effect	Subloading Concept	500
p_r	Parameter controlling crushing resistance		1250
M_x	Parameter controlling the shape of crushing surface	Particle Crushing	0.58
ξ	Volumetric distance between NCL of I_G = 0 and I_G = 1		0.55
p_{x0}	Crushing stress when I_G = 0: (kN/m^2)		1000

* Initial soil state (e_0 = 2.5, p_0 = 0.01 kPa, I_{G0} = 0) before applying the loading process

2.1.2 Evolution law of grading index I_G

Now, the evolution law of I_G is necessary Fortunately, because of the existence of a direct relation between I_G and the evolution law of PSD due to the rushing effect, it is natural to relate I_G to the crushing stress that the soil is exhibited

$$I_G = 1 - exp\left(-\frac{p_x - p_{x0}}{p_r}\right) \tag{2-8}$$

Where, p_x is the crushing stress at the time that particle crushing happens p_{x0} is a constant material parameter representing the magnitude of mean stress that is necessary for the onset of particle crushing in the isotropic consolidation test of soil with unit grading (Figure 2-3a). p_r denotes a constant parameter which controls the rate of particle crushing or the rate of convergence from 0 to 1 of I_G after crushing has been initiated (Figure 2-3) As the magnitude of p_r decreases, i e as the soil weakens, the value of I_G converges faster to 1 The crushing behavior of soil particles obviously depends on the properties of individual grains (such as mineralogy, hardness, shape and size) and environmental conditions (such as packing density, particle size distribution, stress level, and mobilized friction), which would be to some extent reflected in soil parameters p_r and p_{x0}. Eq (2-8) ensures that I_G monotonically increases from 0 to 1 with an increase in p_x with its asymptote being infinity (Figure 2-3) Finally, I_G is a stress dependent coefficient, and its evolution law can be derived as follows:

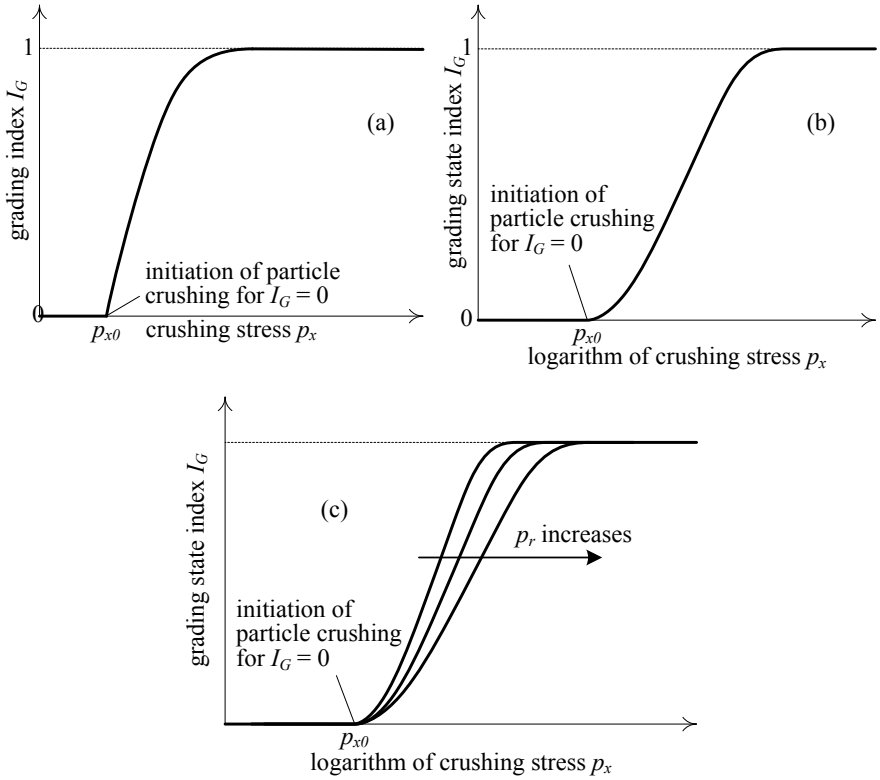

Figure 2-3: Variation of the grading index I_G with the increase of crushing

$$\dot{I}_G = \frac{1}{p_r} exp\left(-\frac{p_x - p_{x0}}{p_r}\right)\dot{p}_x = \frac{1 - I_G}{p_r}\dot{p}_x \tag{2-9}$$

In case of isotropic consolidation, particle crushing happens when the soil stress reaches crushing stress p_x However, in case the soil exhibits shearing after isotropic consolidation, the combined effect of shearing and compressive stress will determine the occurrence of particle crushing For the sake of simplicity, to judge the occurrence of particle crushing with the simultaneous effect of compressive and shearing stress, we proposed the crushing surface f_x as:

$$f_x = lnp + \frac{2}{\alpha} ln\left\{1 + \left(\frac{\eta}{M_x}\right)^{\alpha}\right\} - lnp'_x \tag{2-10}$$

where, M_x is a material parameter that dictates the speed of crushing by controlling the slope of crushing surface Compared to the larger value of M_x, the crushing surface with a smaller M_x is smaller in size in comparison with a larger M_x (Figure 2-4). In other words, the smaller value of M_x implies that under a certain effective mean stress, the magnitude of shearing stress required to initiate particle crushing is smaller.

When particle crushing occurs, $f_x(\sigma_{ij}, p_x) = 0$ & $dp_x > 0$, the consistency condition of f_x requires that $df_x(\sigma_{ij}, p_x) = 0$, which leads to:

$$\dot{p}_x = p_x \frac{\partial f_x}{\partial \boldsymbol{\sigma}_{ij}} \dot{\boldsymbol{\sigma}}_{ij} \tag{2-11}$$

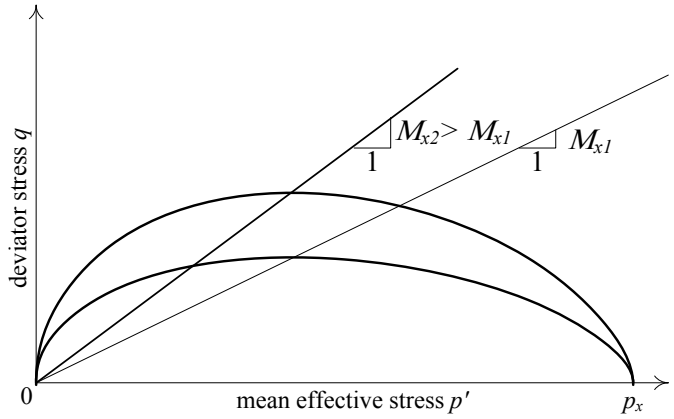

Figure 2-4: M_x parameter & crushing surface

From this basic idea of the proposed evolution law of grading index I_G, we can incorporate to any model to considering particle crushing.

2.2 A constitutive soil model considering particle crushing

An elastoplastic constitutive model exhibiting particle crushing is developed based on continuum mechanics. The proposed model is formulated based on the extension of critical state soil model (Roscoe, Schofield et al. (1963) and Muir Wood (1990)) to incorporate the effect of packing density on the stress-strain characteristics by introducing the concept of subloading surface. Then, the effect of particle crushing is further implemented by considering the evolution of particle size distribution due to crushing stress change and its effect on the constitutive behavior.

2.2.1 Small strain assumption

First of all, we assume additive decomposition of the total strain rate tensor as:

$$\dot{\boldsymbol{\varepsilon}} = \dot{\boldsymbol{\varepsilon}}^{\mathrm{e}} + \dot{\boldsymbol{\varepsilon}}^{\mathrm{p}} \tag{2-12}$$

where $\dot{\boldsymbol{\varepsilon}}^{\mathrm{e}}$ and $\dot{\boldsymbol{\varepsilon}}^{\mathrm{p}}$ are elastic and plastic strain rate tensors, respectively

2.2.2 Elastic stress-strain relationship

For elastic stress–strain relationship, we assume a conventional, nonlinear elastic bulk modulus K given as:

$$K = \frac{v_0}{\kappa} p' \tag{2-13}$$

where, v_0 is initial specific volume, κ is swelling index that represents the slope of elastic volumetric relationship in semi-logarithmic ln p'–v plane and p' is mean effective stress given by $trace(\boldsymbol{\sigma}')$ where $\boldsymbol{\sigma}'$ is the Cauchy's effective stress tensor The shear modulus G is given as:

$$G = \frac{3K(1-2v_e)}{2(1+v_e)} \tag{2-14}$$

where the Poisson's ratio v_e is assumed to be constant in this model

Thus, the rate form of the elastic relationship is derived as:

$$\dot{\boldsymbol{\sigma}}' = \boldsymbol{D}^{\boldsymbol{e}}:\dot{\boldsymbol{\varepsilon}}^{\boldsymbol{e}} = \boldsymbol{D}^{\boldsymbol{e}}:(\dot{\boldsymbol{\varepsilon}} - \dot{\boldsymbol{\varepsilon}}^{\boldsymbol{p}}) \tag{2-15}$$

where $\boldsymbol{D}^{\mathrm{e}}$ denotes the elastic stiffness tensor given as:

$$\boldsymbol{D}^{\boldsymbol{e}} = K\mathbf{1}\otimes\mathbf{1} + 2G\left(\boldsymbol{I} - \frac{\mathbf{1}}{\mathbf{3}}\mathbf{1}\otimes\mathbf{1}\right) \tag{2-16}$$

As an inverse tensor of the elastic stiffness tensor always exists, we get,

$$\dot{\boldsymbol{\varepsilon}}^{\boldsymbol{e}} = (\boldsymbol{D}^{\boldsymbol{e}})^{-\mathbf{1}}:\dot{\boldsymbol{\sigma}}' \tag{2-17}$$

Taking the trace on both sides of Eq. (2-15), we get the elastic volumetric strain as:

$$\boldsymbol{\varepsilon}_{\boldsymbol{v}}^{\boldsymbol{e}} = \frac{\kappa}{1+e_0} ln\frac{p'}{p_0'} \tag{2-18}$$

2.2.3 Yield function

Critical state is an ultimate condition towards which all states of soil finally approach when the soil is sheared. The critical state line (*CSL*) has been chosen as linear in a semi-logarithmic compression plane, which is the specific volume, v (= 1+e), versus the logarithm of mean effective stress, ln p'. Similar to the critical state line (*CSL*), Limiting Isotropic Consolidation Line (*LICL*) is a reference line in the v-ln p' plane where any stress state finally approaches under isotropic compression. It is customary to utilize the sstate boundary surface containing *CSL* and *LICL* (Figure 2-5) in the formation of critical state model Roscoe, Schofield et al. (1963). Specific volume on the state boundary surface, v_{sbs}, which defines the loosest state of soil at the current stress (p,η) is given by considering the combined effects of compression and dilation as:

$$v_{sbs} = N - \lambda ln\frac{p'}{p_a} + (\Gamma - N)\zeta(\eta) \tag{2-19}$$

where, $\eta(=q/p')$ is stress ratio, q is deviator stress, $p_a(=98kPa)$ denotes atmospheric pressure, λ is compression index, $\zeta(\eta)$ is a monotonic increasing function of stress ratio η satisfying $\zeta(0)$=0 on *LICL* and $\zeta(M)=1$ on *CSL*. M is critical state stress ratio (=η_{cs}). N and Γ represent specific volumes on *LICL* (η = 0) and *CSL* (η = M) at $p'=p_a$, respectively. It is postulated that different functions of $\zeta(\eta)$ are used for different versions of critical state models (Figure 2-6):

$$\zeta(\eta) = \frac{ln\left\{1+\left(\frac{\eta}{M}\right)^{\alpha}\right\}}{ln2} \tag{2-20}$$

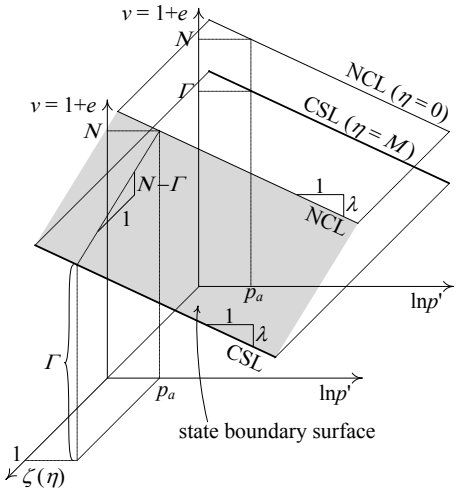

Figure 2-5 : Specific volume of soils in loosest state

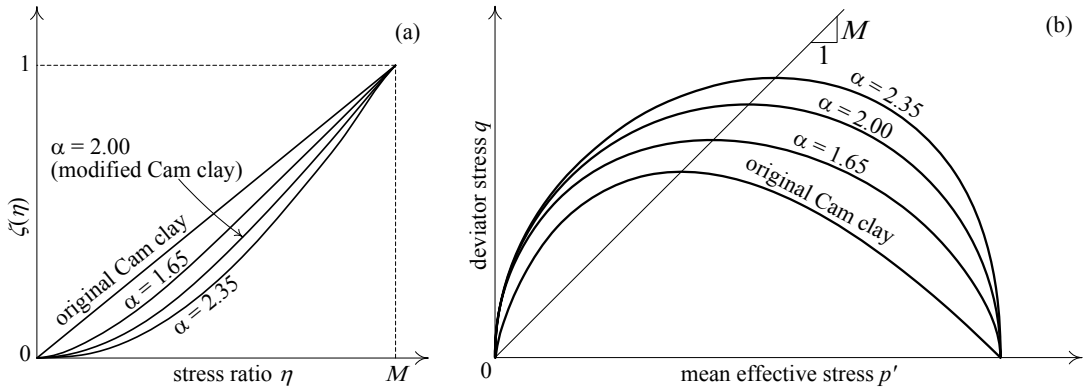

Figure 2-6: a) Variation of $\zeta(\eta)$ with respect to α. b) Different shapes of yield function with respect to α

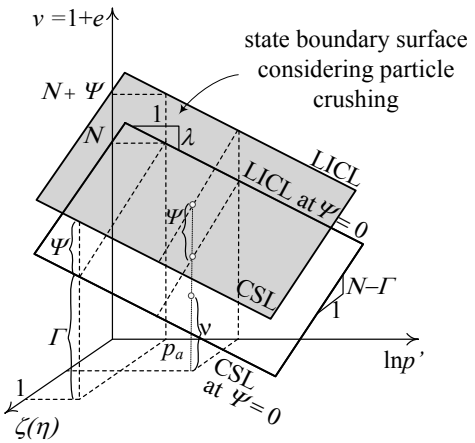

Figure 2-7: State boundary surface considering particle crushing effect

The particle crushing effect on soil behavior is then incorporated by extending the critical state concept. As noticed by a lot of researchers, breakage caused a downward parallel shift in the CSL in *e*-log*p'* space (Daouadji, Hicher et al. (2001), Wood and Maeda (2008), Ghafghazi, Shuttle et al. (2014), Bandini and COOP (2011)) and that the downward shift is a parallel shift of CSL in *e*-log *p'*

space (Ghafghazi, Shuttle et al. 2014). The occurrence of particle crushing will lead to a denser state of the soil; therefore, our key concept in the formulation the model for particle crushing here is that the particle crushing effect of soils is considered by the downward parallel movement of the state boundary surface in the volumetric plane of p' and v. For this purpose, a state variable ψ is newly introduced to represent the downward shift of the state boundary surface in the $(lnp', \zeta(\eta), v)$ space as indicated in Figure 2-7 . From this, the state parameter ψ is a non-negative variable defined as the volumetric distance between the state boundary surfaces for soil with and without crushing effect. ψ works as a state variable controlling the elastoplastic response in the constitutive model. The specific volume on the state boundary surface of crushed soil, $v_{sbs}^{crushed}$, is thus given in a similar way as Eq. (2-19).

$$v_{sbs}^{crushed} = v_{NC} + \psi = \mathrm{N} - \lambda ln\frac{p'}{p_a} + (\Gamma - \mathrm{N})\zeta(\eta) + \psi \tag{2-21}$$

Since the soil whose states lie under the state boundary surface do exhibit plastic strain together with elastic strain, subloading surface concept proposed by Hashiguchi and Ueno (1977) is further introduced to portray this behavior. Using a state parameter Ω, the combination of specific volume and mean effective stress to describe the changing strength and stiffness is incorporated in this model. As all states of soil locate on or below the state boundary surface in Figure 2-8, the state boundary surface defines the loosest, upper limit of specific volume of soils. Consequently, the state parameter Ω is thus defined as the specific volume difference between the current state and the loosest state under the same stress (p, η) on the state boundary surface as shown in Figure 2-8.

According to this concept, soil exhibits irreversible deformation below the state boundary surface and gradually approaches the state boundary surface with loading Taking a state variable Ω that is the difference between the specific volume of the current state and that on the state boundary surface under the same stress (p', η), we can represent an arbitrary specific volume v:

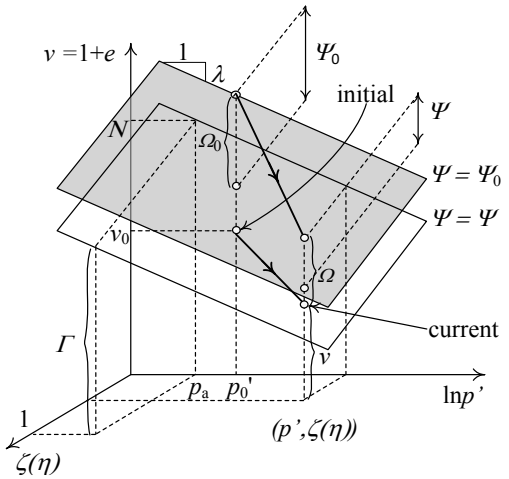

Figure 2-8: Modeling of volumetric behavior of soil considering particle crushing and density effect

$$v = v_{sbs}^{crushed} - \Omega = \mathrm{N} - \lambda \frac{lnp'}{p_a} + (\Gamma - \mathrm{N})\zeta(\eta) + \psi - \Omega \tag{2-22}$$

The definition of the state variable $\Omega \geq 0$ is illustrated in Figure 2-8. Though Been and Jefferies (1985) proposed a similar state parameter as volumetric distance of the soil from the reference state on the steady state line under current mean effective stress, our parameter Ω always refers to the volumetric distance from the current state to the loosest state of soil (specific volume on the state boundary surface) under the current stress condition p' and q and the current state parameter for crushing level ψ

During plastic flow Ω decreases gradually with the development of plastic deformation and finally converges to zero An evolution law of Ω can, therefore, be chosen as:

$$\frac{\dot{\Omega}}{v_0} = -Q(\Omega)\|\dot{\boldsymbol{\varepsilon}}^{\boldsymbol{p}}\| \tag{2-23}$$

where, $\dot{\boldsymbol{\varepsilon}}^{p}$ is plastic strain rate tensor and $Q(\Omega)$is a function of Ω given as:

$$Q(\Omega) = \omega\Omega|\Omega| \tag{2-24}$$

where ω is a parameter controlling the effect of density

From the current specific volume v by Eq (2-22), we can also calculate the initial specific volume v_0 by substituting the initial states: $= v_0, \psi = \psi_0, \Omega = \Omega_0,\ p' = p'_0, q = q_0$:

$$v_0 = \mathrm{N} - \lambda \frac{lnp'_0}{p_a} + \psi_0 - \Omega_0 \tag{2-25}$$

Total volumetric strain (compression is taken to be positive) generated from the initial state to the current state is given by:

$$\varepsilon_v = -\frac{dv}{v_0} = \frac{v_0 - v}{v_0} \tag{2-26}$$

By substituting Eqs (2-22) and (2-25) for Eq (2-26), we get,

$$\varepsilon_v = \frac{1}{v_0}\left\{\lambda ln\frac{p'}{p_0} + (\mathrm{N} - \Gamma)\zeta(\eta) - (\psi - \psi_0) + (\Omega - \Omega_0)\right\} \tag{2-27}$$

Plastic volumetric strain can be determined by taking a difference between the total volumetric strain given by Eq (2-27) and the elastic volumetric strain is given by Eq (2-14):

$$\varepsilon_v^p = \frac{1}{v_0}\left\{(\lambda - \kappa) ln\frac{p'}{p_0} + (\mathrm{N} - \Gamma)\zeta(\eta) - (\psi - \psi_0) + (\Omega - \Omega_0)\right\} \tag{2-28}$$

From Eq (2-28), yield function f for soil considering the effect of particle crushing can be written as follows:

$$f = \frac{1}{v_0}\left\{(\lambda - \kappa) ln\frac{p'}{p_0} + (\mathrm{N} - \Gamma)\zeta(\eta) - (\psi - \psi_0) + (\Omega - \Omega_0)\right\} - \varepsilon_v^p \tag{2-29}$$

2.2.4 Flow rule

Assuming associated flow rule in the proposed model, we obtain the plastic strain rate tensor as:

$$\dot{\boldsymbol{\varepsilon}}^{\boldsymbol{p}} = \langle \dot{\Lambda} \rangle \frac{\partial f}{\partial \boldsymbol{\sigma}'} \tag{2-30}$$

where $\dot{\Lambda}$ is the rate of the plastic multiplier The loading criterion is thus given by $\dot{\Lambda} > 0$ As unlimited distortional strain is exhibited at critical state without any change in stress or volume, $trace(\partial f/\partial \boldsymbol{\sigma})$becomes zero when η is equal to M. (N − Γ)is thus equal to $2ln2(\lambda - \kappa)/\alpha)$ in case Eq. (2-20) is applied and the yield function is finally given as follows:

$$f = \frac{\lambda - \kappa}{\upsilon_0}\left[ln\frac{p'}{p_0} + \frac{2}{\alpha}ln\left\{1 + \left(\frac{\eta}{M}\right)^{\alpha}\right\}\right] - \frac{\psi - \psi_0}{\upsilon_0} + \frac{\Omega - \Omega_0}{\upsilon_0} - \varepsilon_v^p \tag{2-31}$$

Notice that if subloading effect is necessary in this model if the crushing surface is smaller than yield surface. This is because plastic strain due to crushing phenomenon occurs even when the soil state locates inside the yield surface. On the other hand, if yield surface is smaller than crushing surface, then subloading concept is not a must in the formulation of this model. However, because plastic strain is always observed in the behavior of soil, regardless of the occurrence of crushing, subloading concept should be implemented in the model

2.2.5 Hardening rule

Evidently, particle crushing will increase the soil's density Since we know I_G accounts for the level of particle crushing and ψ. is responsible for the packing & density effect on soil, I_G and ψ has a close relationship Thus, it is possible to relate I_G and ψ as follows: (see Figure 2-9)

$$\psi = \xi(1 - I_G) \tag{2-32}$$

In which ξ is the distance from the NCL of the initial state of soil to NCL of the soil when PSD reaches its critical grading.

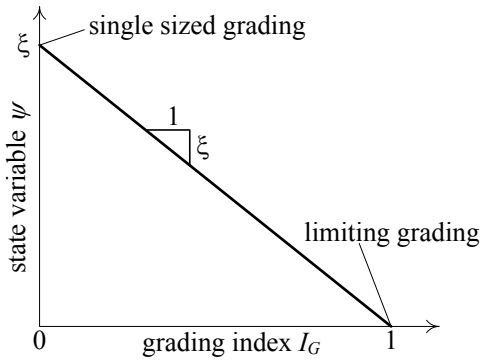

Figure 2-9: Relationship between grading index I_G and state parameter ψ

The evolution law of ψ is derived by taking the time derivative of both sides of Eq (2-32):

$$\dot{\psi} = \xi \dot{I}_G \tag{2-33}$$

From Eqs (2-33), (2-9) and (2-11) we obtain:

$$\dot{\psi} = \frac{\partial \psi}{\partial I_G}\frac{\partial I_G}{\partial p_x}\frac{\partial p_x}{\partial \boldsymbol{\sigma}_{ij}}\dot{\boldsymbol{\sigma}}_{ij} = -\frac{\xi}{p_r}(1-I_G)p_x\frac{\partial f}{\partial \boldsymbol{\sigma}_{ij}}\dot{\boldsymbol{\sigma}}_{ij} \tag{2-34}$$

2.2.6 Elastoplastic stiffness matrix

During purely elastic regime, the rate of the multiplier $\langle \dot{\Lambda} \rangle$ remains zero. Meanwhile, during elastoplastic deformation, the stress state remains to stay on the yield surface and the yield function f remains zero. The time derivative of the yield function $\dot{f}$ consequently vanishes whenever the rate of the plastic multiplier $\langle \dot{\Lambda} \rangle$ is positive. Hence, we can write the consistency condition that has a general validity regardless of elastic or elastoplastic deformation as:

$$0 = \langle \dot{\Lambda} \rangle \dot{f} \tag{2-35}$$

During plastic flow, we apply the consistency condition to the time derivative of the yield function $\dot{f}\left(\boldsymbol{\sigma}', \varepsilon_{\mathrm{v}}^{\mathrm{p}}, \Psi, \Omega\right)$ calculated from Eq (2-31) as:

$$\dot{f} = \frac{\partial f}{\partial \boldsymbol{\sigma}'}:\dot{\boldsymbol{\sigma}}' + \frac{\partial f}{\partial \psi}:\dot{\psi} + \frac{\partial f}{\partial \Omega}:\dot{\Omega} + \frac{\partial f}{\partial \varepsilon_v^p}:\dot{\varepsilon}_v^p = \frac{\partial f}{\partial \boldsymbol{\sigma}'}:\dot{\boldsymbol{\sigma}}' - \frac{\dot{\psi}}{v_0} + \frac{\dot{\Omega}}{v_0} - \dot{\varepsilon}_v^p = 0 \tag{2-36}$$

Inserting Eqs. (2-23), (2-30), (2-34) into Eq. (2-36), we get,

$$\left[\frac{\partial f}{\partial \boldsymbol{\sigma}'} + \frac{1}{v_0}\frac{\xi}{p_r}(1-I_G)p_x\frac{\partial f}{\partial \boldsymbol{\sigma}'}\right]:\boldsymbol{\sigma}' + \left[Q(\Omega)\left\|\frac{\partial f}{\partial \boldsymbol{\sigma}'}\right\| - tr\left(\frac{\partial f}{\partial \boldsymbol{\sigma}'}\right)\right]\langle \dot{\Lambda} \rangle = 0 \tag{2-37}$$

Thus, we obtain the plastic multiplier as:

$$\langle \dot{\boldsymbol{\Lambda}} \rangle = \langle \frac{\left[\frac{\partial f}{\partial \boldsymbol{\sigma}'} + \frac{1}{v_0}\frac{\xi}{p_r}(1-I_G)p_x\frac{\partial f}{\partial \boldsymbol{\sigma}'}\right]:\boldsymbol{D^e}:d\boldsymbol{\varepsilon}}{Q(\Omega)\left\|\frac{\partial f}{\partial \boldsymbol{\sigma}'}\right\| - tr\left(\frac{\partial f}{\partial \sigma'}\right) + \left[\frac{\partial f}{\partial \boldsymbol{\sigma}'} + \frac{1}{v_0}\frac{\xi}{p_r}(1-I_G)p_x\frac{\partial f}{\partial \boldsymbol{\sigma}'}\right]:D^e:\frac{\partial f}{\partial \boldsymbol{\sigma}'}} \rangle \tag{2-38}$$

Consequently, the rate form of the elastoplastic stress-strain relationship is obtained from Eqs (2-15), (2-30)and (2-38):

$$\dot{\boldsymbol{\sigma}}' = \left[\boldsymbol{D^e} - \langle \frac{\left[\frac{\partial f}{\partial \sigma'} + \frac{1}{v_0}\frac{\xi}{p_r}(1-I_G)p_x\frac{\partial f}{\partial \sigma'}\right]:\boldsymbol{D^e}:d\boldsymbol{\varepsilon}}{Q(\Omega)\left\|\frac{\partial f}{\partial \boldsymbol{\sigma}'}\right\| - tr\left(\frac{\partial f}{\partial \boldsymbol{\sigma}'}\right) + \left[\frac{\partial f}{\partial \boldsymbol{\sigma}'} + \frac{1}{v_0}\frac{\xi}{p_r}(1-I_G)p_x\frac{\partial f}{\partial \boldsymbol{\sigma}'}\right]:\boldsymbol{D}^e:\frac{\partial f}{\partial \boldsymbol{\sigma}'}} \rangle\right]:\dot{\boldsymbol{\varepsilon}} \tag{2-39}$$

When the rate of the plastic multiplier $\dot{\Lambda} = 0$ the soil's behavior is purely elastic with the elastic stiffness $\boldsymbol{D}^e$. On the contrary, when the rate of the plastic multiplier is $\dot{\Lambda} > 0$, the soil exhibits deformation under elastoplastic deformation. Then, the occurrence of particle crushing will be available if $(df_x > 0 \;\&\; p_x = 0)$. In this case, it can be identified that the soil exhibits particle crushing phenomenon together with plastic flow under the elastoplastic stiffness $\boldsymbol{D}_1^{ep}$:

$$\boldsymbol{D}_{\mathbf{1}}^{\boldsymbol{ep}} = \boldsymbol{D}^{\boldsymbol{e}} - \frac{\left[\frac{\partial f}{\partial \boldsymbol{\sigma}'} + \frac{1}{v_0}\frac{\xi}{p_r}(1-I_G)p_x\frac{\partial f}{\partial \boldsymbol{\sigma}'}\right]:\boldsymbol{D}^{\boldsymbol{e}}:d\boldsymbol{\varepsilon}}{Q(\Omega)\left\|\frac{\partial f}{\partial \boldsymbol{\sigma}'}\right\| - tr\left(\frac{\partial f}{\partial \boldsymbol{\sigma}'}\right) + \left[\frac{\partial f}{\partial \boldsymbol{\sigma}'} + \frac{1}{v_0}\frac{\xi}{p_r}(1-I_G)p_x\frac{\partial f}{\partial \boldsymbol{\sigma}'}\right]:\boldsymbol{D}^{\boldsymbol{e}}:\frac{\partial f}{\partial \boldsymbol{\sigma}'}} \tag{2-40}$$

Nevertheless, if particle crushing does not occur ($f_c < 0$), then $dp_c = 0$ which in turn lead to the fact that soil exhibits elastoplastic deformation with the stiffness $\boldsymbol{D}_{\mathbf{2}}^{\boldsymbol{ep}}$ as follows:

$$\boldsymbol{D}_{\mathbf{2}}^{\boldsymbol{ep}} = \boldsymbol{D}^{\boldsymbol{e}} - \frac{\frac{\partial f}{\partial \boldsymbol{\sigma}'}:\boldsymbol{D}^{\boldsymbol{e}}:d\boldsymbol{\varepsilon}}{Q(\Omega)\left\|\frac{\partial f}{\partial \boldsymbol{\sigma}'}\right\| - tr\left(\frac{\partial f}{\partial \boldsymbol{\sigma}'}\right) + \frac{\partial f}{\partial \boldsymbol{\sigma}'}:\boldsymbol{D}^{\boldsymbol{e}}:\frac{\partial f}{\partial \boldsymbol{\sigma}'}} \tag{2-41}$$

2.3 Conclusion

A simple model considering the particle crushing phenomenon for soil has been developed in the framework of continuum mechanics. The key strength of this model is that the consideration of the effect of particle crushing during consolidation and shearing in a unique manner. Furthermore, the evolution of the particle sized distribution due to particle crushing is fully obtained by a single grading state index in our model. Also, the easy adoption of the model to FEM reveals the large applicability of the model.

Chapter 3 : Validation of Soil Constitutive Model Considering Particle Crushing

3.1 Purpose

Table 3-1: Material parameters for numerical simulation of Dogs Bay Sand

λ	0.2650	parameters for Cam clay	compression index
κ	0.0015		swelling index
M	1.65		critical state stress ratio (= η_{cs})
N	2.80		specific volume v on NCL at p = 98 kPa
v	0.20		Poisson's ratio
α	1.65	parameter for subloading surface	shape of the yield surface
a	500		effect of density
p_{ci} [kPa]	100	parameters for particle crushing mechanism	crushing strength for single sized grading
p_r [kPa]	5000		crushing resistance
M_c	0.58		effect of shearing on crushing
ξ	0.55		volumetric distance between state boundary surfaces for I_G = 0 and 1

This section presents the performance of the proposed model in capturing the behavior of Dogs Bay Sand, a crushable soil, via experimental tests by Coop and Lee (1993). These elementary tests used in this chapter include isotropic consolidation triaxial test, consolidated undrained triaxial tests, consolidation drained triaxial tests with constant mean stresses, and consolidated drained triaxial tests with constant radial stresses. The material parameterss for simulation are listed in Table 3-1. The calibration process to obtain these material parameters will alsobe explained in section 3.2.

3.1.1 Isotropic consolidation triaxial test

Coop and Lee (1993), carried out the isotropic consolidation test on Dogs Bay Sand, from a unit grading at initial state, up to a high value of mean stress. As observed in Figure 3-1 , the variation of grading index I_G revealed that the soil had been crushed during loading process. The simulation showed the movement of LICL with respect to the changing of PSD state of soil from unit grading (I_G = 0) to critical grading (I_G = 1). This numerical simulation showed that our model can capture not only stress-strain behavior but also the variation of grading index of the crushable soil. In this experiment, I_G value did not reach its maximum value, which means the soil has not reached its critical PSD. However, in the following sections of CD and CU tests, the soil is initially isotropically compressed, and then sheared up to its critical PSD

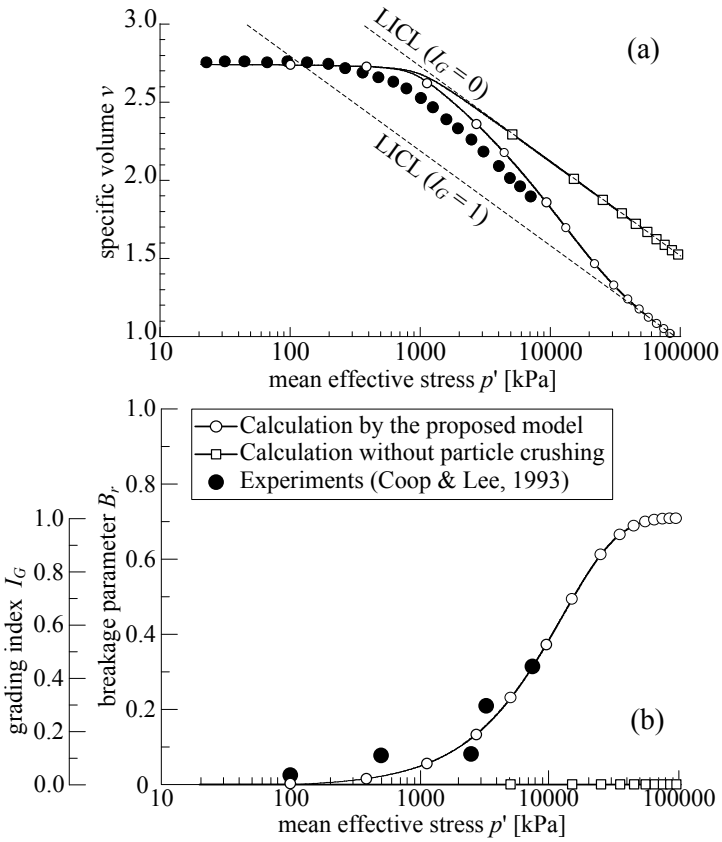

Figure 3-1: Isotropic consolidation test of soil (Coop & Lee, 1993) and its corresponding simulation

3.1.2 Consolidated undrained triaxial tests

Figure 3-2 and Figure 3-3 showed the results of experimental CU test under high and low confining pressures, respectively by Coop and Lee (1993) and their corresponding simulation by our model. In high confining pressure CU test, crushing occurs much more (I_G = 0.6) than with relative low confining pressure (I_G is approximately 0.15).

The corresponding B_r index (Hardin (1985)) is also shown in Figure 3-4. By observing the simulation results, we can see that the model could depict very well the stress-strain behavior of soil under high confining pressure (with crushing phenomenon) and low confining pressure (without crushing) with different confining pressures via controlling crushing parameters. Furthermore, Figure 3-3b revealed that the critical state of the crushable soil was unique, by experimental tests and this was captured by our proposed model.

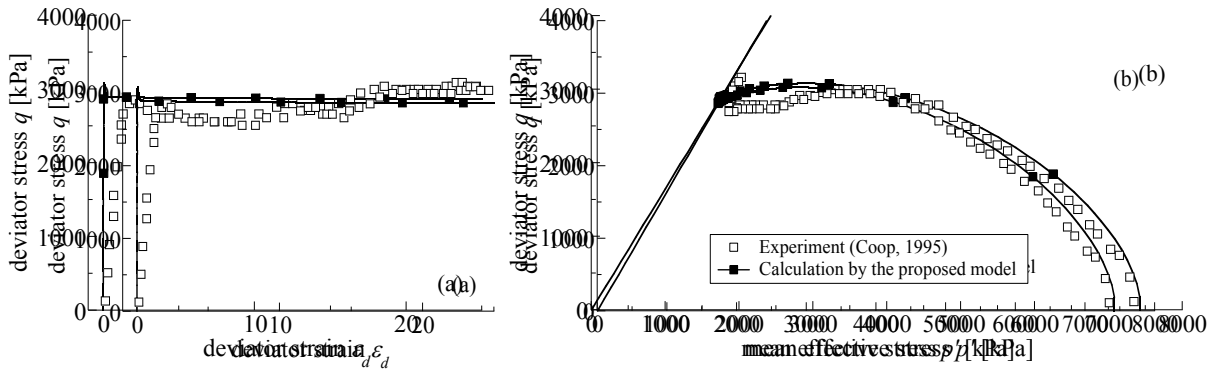

Figure 3-2: Undrained shearing tests of crushable soil (Coop & Lee, 1993) and their simulations under high confining stress

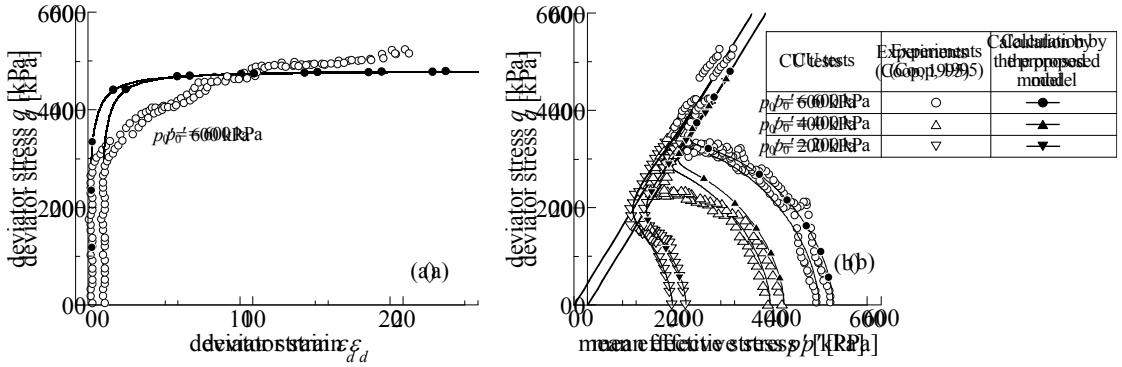

Figure 3-3: Undrained shearing tests of crushable soil (Coop & Lee, 1993) and their simulations under low confining stress

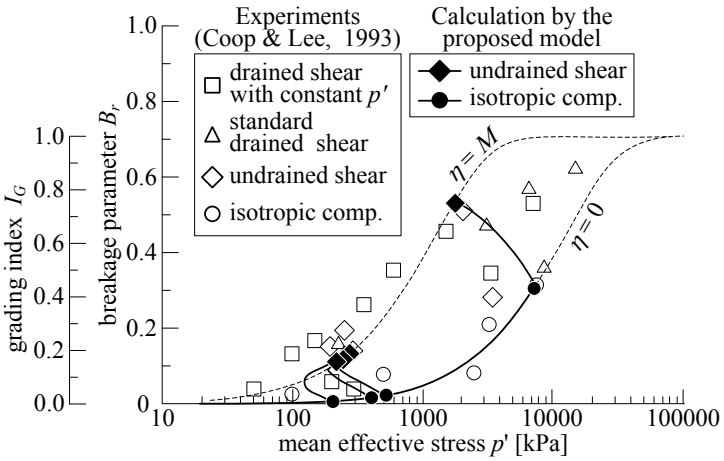

Figure 3-4: Variations of grading index I_G in CU tests

3.1.3 Consolidated drained triaxial tests

Luzzani and MR (2002) presented constant mean effective stress CD triaxial test and constant confining pressure CD triaxial test of high values of confining pressure to assure the occurrence of crushing in Dog Bay Sand. In these tests, the confining pressures were very high (more than 3200 kPa), which caused the significant crushing of soil. Thus these simulations assumed that the soil reached its critical grading after being shearing at such a high confining pressures of CD test with constant radial stresses. Figure 3-5 and Figure 3-6 compared the experimental data and its corresponding simulation results by our proposed model. Our model showed good performance when capturing well the overall trend of the negative dilatancy behavior of soil exhibiting particle crushing under CD elementary test (both constant mean stress CD trixial test and constant confining pressure CD test) as shown in the figures.

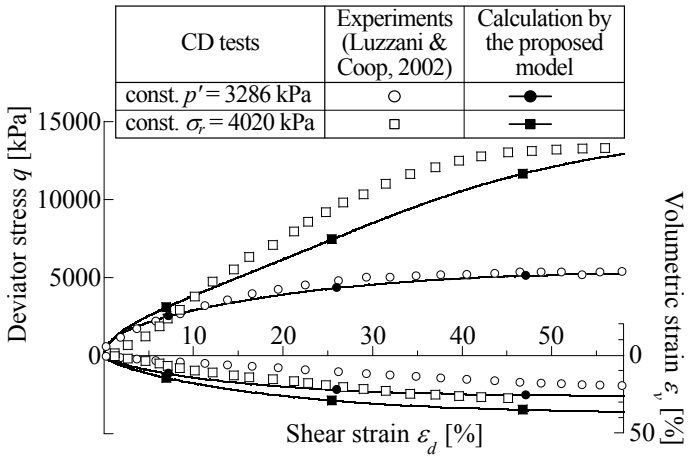

Figure 3-5: A comparison between simulation results and experimental results by Luzzani & Coop, 2002

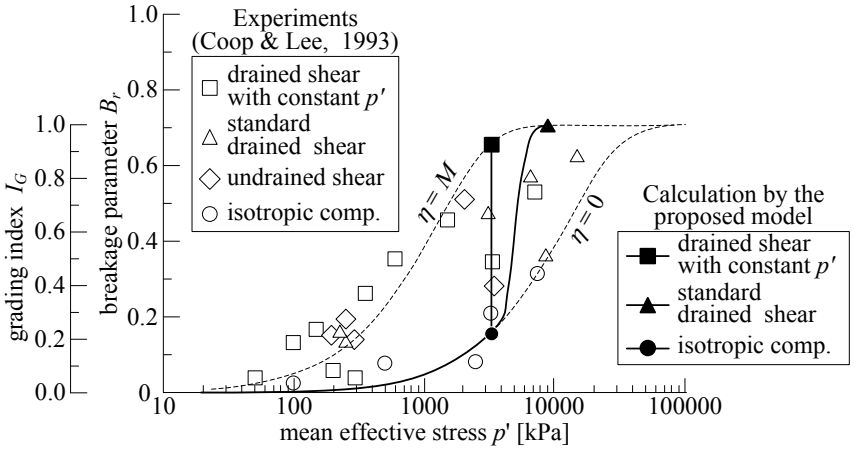

Figure 3-6: Variation of I_G in CD tests

3.1.4 The non-uniqueness of critical state line for crushable soil under loading

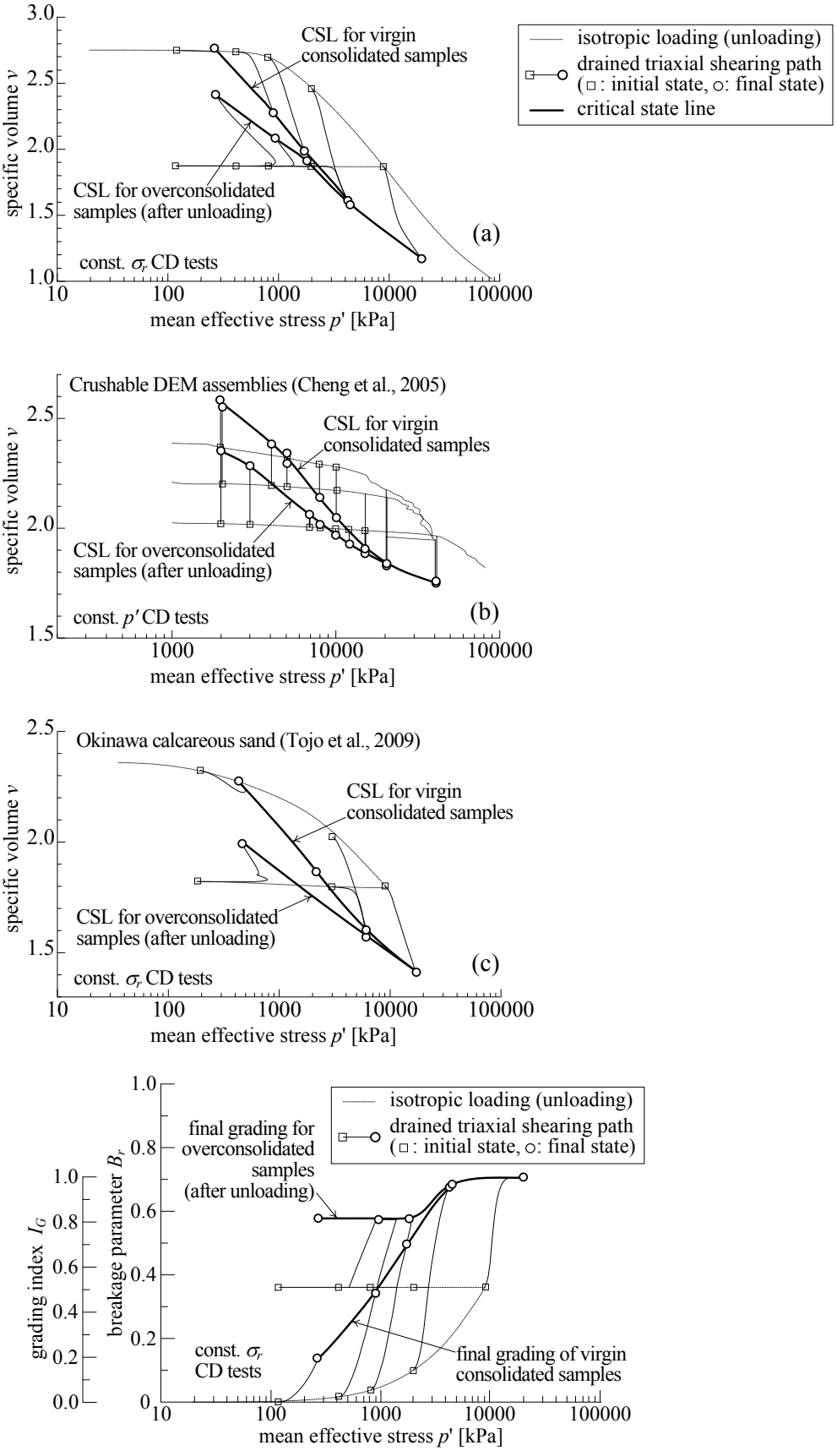

Figure 3-7: The non-unique of critical state line observed by numerical simulation results

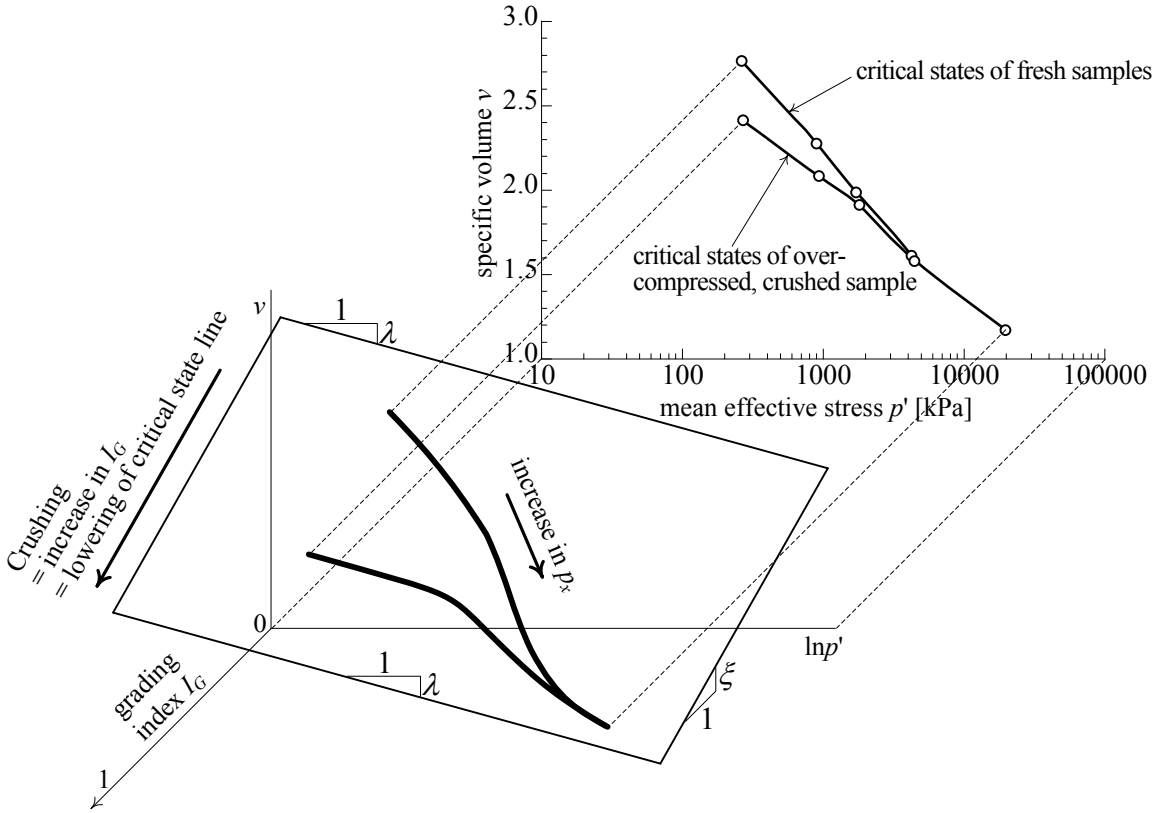

Figure 3-8: Correlation between from the critical state surface of normally consolidated soil to that of the overconsolidated soil

The non-unique CSL of crushable soil during loading process was observed in experimental tests by Tojo, Yamada et al. (2009) (Figure 3-7c) as well as the DEM simulation by Cheng, Bolton et al. (2005) (Figure 3-7b). Firstly, the CSL of NC soil was obtained by compressing NC soil isotropically, then shearing it up to its critical state. After that, the CSL of OC soil was also checked by firstly compressing NC soil up to large mean stress then unloading it to a small magnitude of mean stress, following by shearing it to its critical state. Tojo, Yamada et al. (2009) indicated that the CSL of NC soil and OC soil when they exhibit crushing effect is not unique. Similarly, our model could also describe the non-uniqueness characteristic of CSL when simulating the behavior of NC and OC crushable soil in the same process. In our model, after being compressed to large mean stresses, the occurrence of crushing move the state boundary surface down which resulted in the downward movement of CSL. The movement of CSL with respect to the level of crushing in our model was explained in Figure 3-8. The more crushing the soil exhibited, the farther the new CSL was from the original CSL. On the way moving down of CSL due to crushing, when shearing processes were applied, the final critical states were obtained in Figure 3-8. The CSL in Figure 3-8 was the CSL of difference I_G values, in which CSL of each I_G value was a straight parallel line.

3.1.5 Effect of fine contents to soil behavior

Another possible application of our model is to study the behavior of the same soil with different fine contents. Zlatović and Ishihara (1995) experimentally studied the effect of fine content to the behavior of Toyoura sand via CU tests by analyzing the stress-path with a variety of PSD with respect to a wide range of fine content F_c (Figure 3-9c). The different CU stress paths (Figure 3-9b) of Toyoura sand with different silt contents were observed in Figure 3-9a. On the basis of his experimental observations, we can conclude that the same soil with a large number of fine content should have a weaker strength in comparison with the soil with a small amount of fine content. In the same way, our proposed model was able to check the behavior of the same soil material exhibiting no crushing, but with different particle size distribution corresponding to various fine contents (Figure 3-9a).

The simulation results indicated that among the soils that were only different in I_G but the same in other properties, the soil that has a small value of I_G grading index showed the larger shear strength.

xOverall, the simulation results in this section revealed the good performance of this model in (1) capturing the behavior of crushable soil in various elementary tests such as isotropic consolidation,

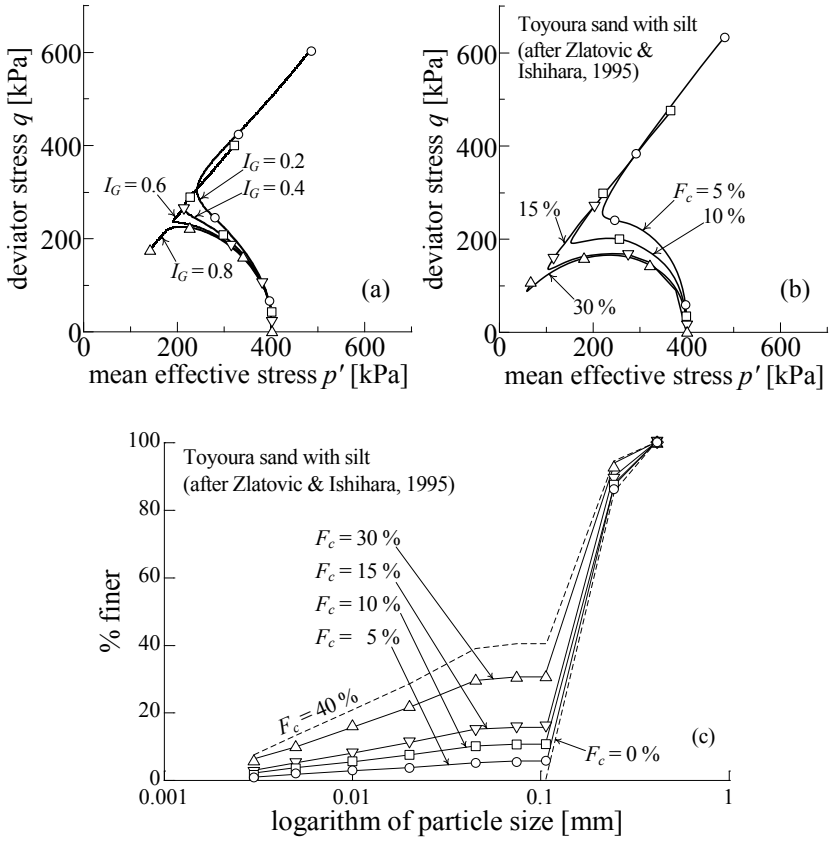

Figure 3-9: Stress path simulation of the same soil 102.with different PSD curve exhibiting non-crushing under CU test

CU, CD test (2) capturing the non-unique of CSL of crushable soil during loading processes. (3) depicting the behavior of uncrushable soil with different amounts of fine contents.

3.2 Parametric studies & parameter calibrations

3.2.1 Initiation of crushing under isotropic compression stress.

p_{x0} is a material parameter representing the maximum magnitude of mean stress that the soil with uniform grading can suffer without particle crushing. A wide range of initial particle crushing p_{x0} from 100kPa to 10000kPa has been simulated to study its effect on stress-strain relationship and the grading index I_G (Figure 3-10). Simulation results illustrated the definition of p_{x0} when showing that the larger p_{x0} is, the slower the onset of crushing is initiated, and the stronger crushing resistant the material is. As such, the stronger to the initiation of crushing the soil is, the larger value of p_{x0} parameter should be. From this simulation, p_{x0} can be obtained by performing isotropic consolidation test up to a high magnitude of mean stress and checking the PSD by sieve analysis. The level of mean stress that initiates the evolution of PSD is p_{x0}.

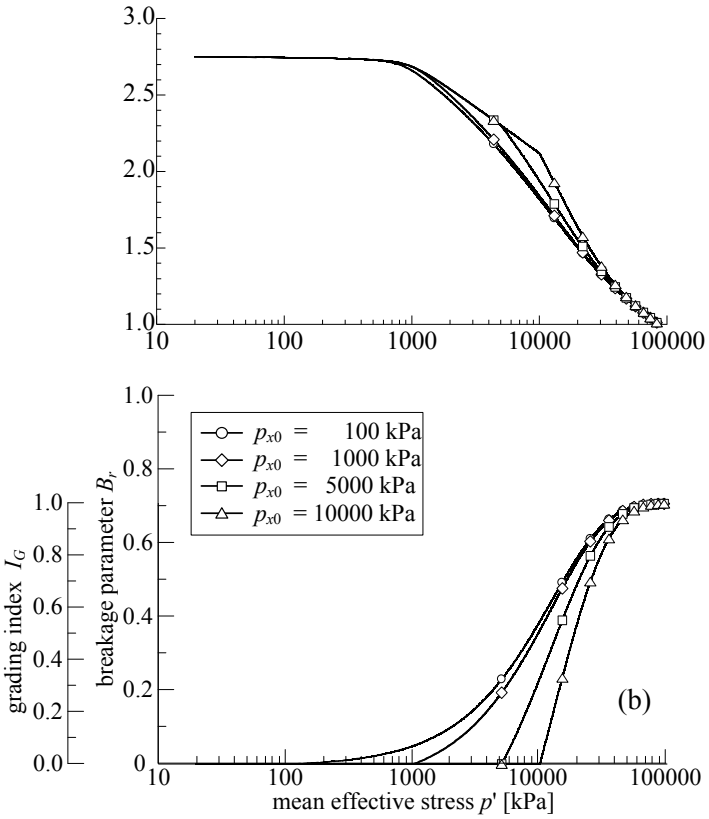

Figure 3-10: Effect of crushing stress p_{x0} material parameters on the model responses

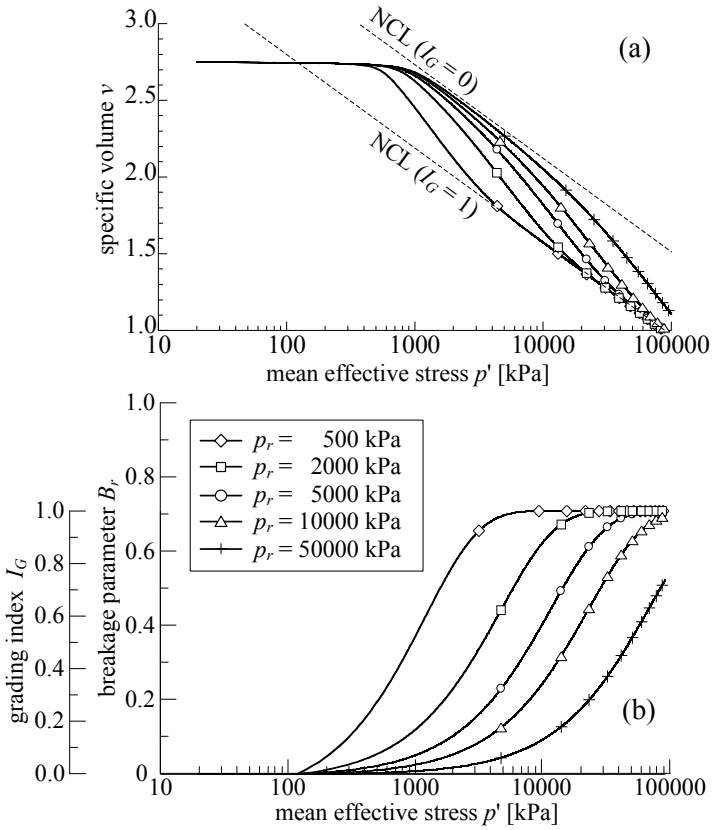

Figure 3-11: Effect crushing resistance p_r material parameter on the model response

3.2.3 Particle crushing resistance

The dependence of I_G on the material parameter p_r on the process of monotonic changing from its initial value to its maximum value (I_G = 1) in Eq. (2-8) is also clarified in Figure 3-11. As can be seen, the smaller the value of p_r be, the faster I_G will convergent to 1. Therefore, after the onset of crushing, the speed of crushing of each kind of material is governed by this p_r parameter. From this isotropic consolidation simulation, it can be recognized that after obtaining the above p_{x0} parameter, the curve fitting method of $I_G - p'$ curve can be used to determine p_r parameter.

3.2.4 Effect of shearing stress on the initiation of crushing

In order to understand how M_x affect stress-strain relationship and the variation of I_G value, CU test simulations were conducted with two different values of M_x The soil's strength was smaller with a smaller value of M_x as shown in Figure 3-12. Materials that are stronger to crushing when suffering shearing stress should have a high value of M_x, and M_x parameter can be determined by the curve fitting method of stress paths in CU test of crushable soils.

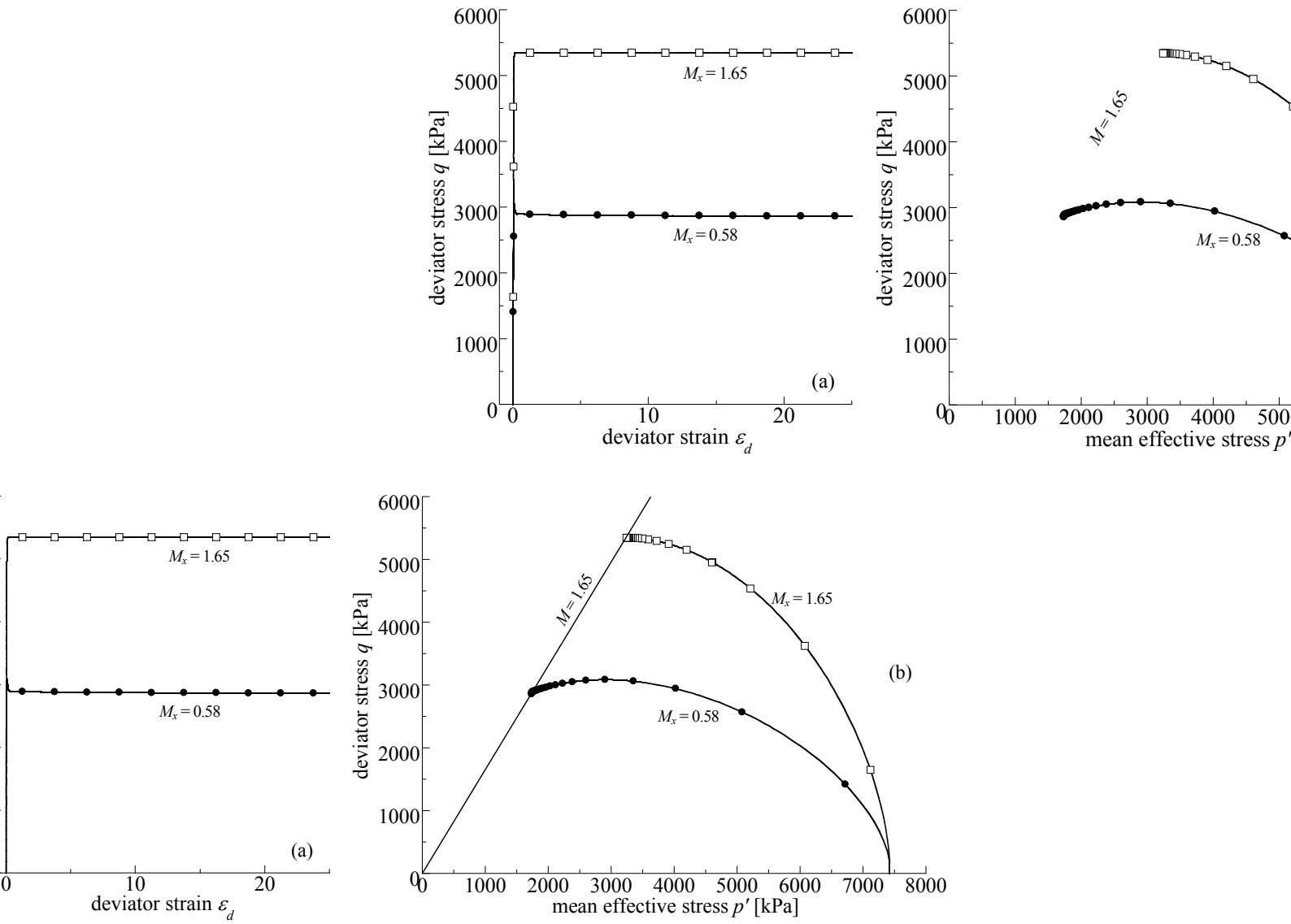

Figure 3-12: Effect of the constitutive parameter on the shearing behavior in CU test (M_x – slope of crushing surface in p-q plane)

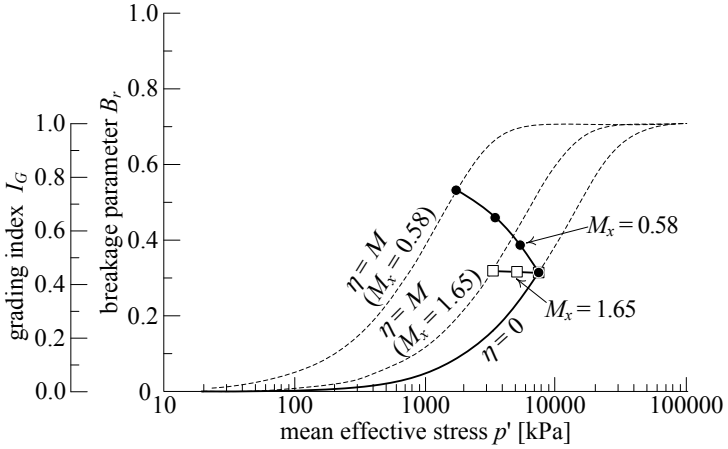

Figure 3-13: Effect of the constitutive parameter on the shearing behavior in CU test (M_x – slope of crushing surface in p-q plane)

3.3 Potential of the model to simulate crushable and uncrushable soil

The ability of the proposed model to predict both the behavior of crushing soil and that of soil exhibiting no crushing can be seen in Figure 3-14. For the soil exhibiting no crushing or too hard to be crushed, we can either set the resistance to crushing p_r or p_{x0} parameter of soil to large values. The combined effect of shearing stress and compressive stress on crushing can be visualized in Figure 3-15. When only compressive stress is applied, the variation of I_G index corresponds to $\eta = 0$ line. When the $\eta = M$ stress path is used, the soil is crushed with a faster convergence to 1 of I_G. For the same mean stress, the larger the value of deviator stress, the larger the effect of crushing will occur.

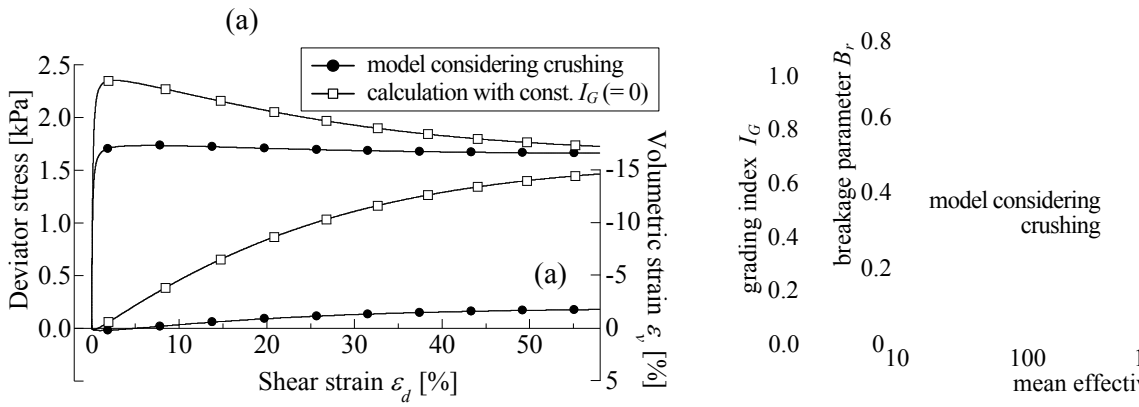

Figure 3-14: Effect of particle crushing on the response in CD test (calculation results by the proposed model and the model in which I_G is kept constant (I_G =0.0-unit grading)

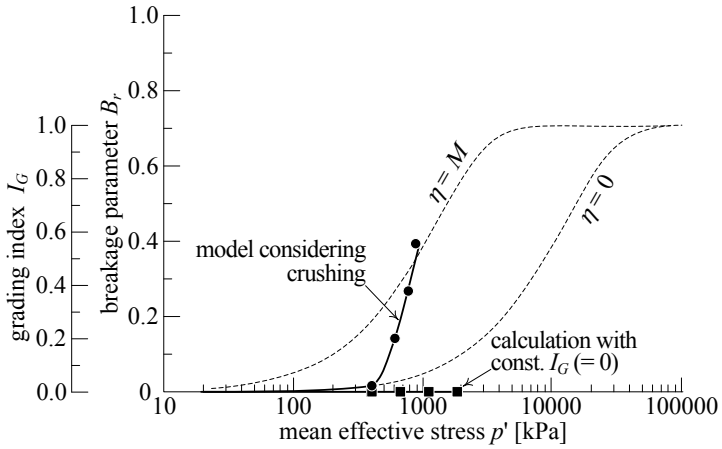

Figure 3-15: Grading index evolution law for crushing and non-crushing soils

3.4 Conclusions

. A number of validations of the proposed model via experimental tests have proved the potential of the model to well predict the crushing soil behavior under different loading conditions: isotropic compression test, consolidated undrained tests, isotropic consolidation test. Not only stress-strain behavior, but also the changing of grading index are well depicted by our proposed model. Furthermore, the advantage of this model is that it can be used both for crushable soil and uncrushable soil.

Chapter 4 : Volumetric Locking Problem in Finite Element Method & Its Countermeasures

4.1 Review of the framework of Finite Element Method

4.1.1 Strong form of mechanical problems

The equilibrium equations in the general 3D case:

$$\begin{cases} \dfrac{\partial \sigma_{xx}}{\partial x} + \dfrac{\partial \tau_{xy}}{\partial y} + \dfrac{\partial \tau_{xz}}{\partial z} + b_x = 0 \\ \dfrac{\partial \tau_{xy}}{\partial x} + \dfrac{\partial \sigma_{yy}}{\partial y} + \dfrac{\partial \tau_{yz}}{\partial z} + b_y = 0 \\ \dfrac{\partial \sigma_{xz}}{\partial x} + \dfrac{\partial \tau_{yz}}{\partial y} + \dfrac{\partial \sigma_{zz}}{\partial z} + b_z = 0 \end{cases} \tag{4-1}$$

Or in contract form:

$$\nabla_S^T \boldsymbol{\sigma} + \boldsymbol{b} = 0 \tag{4-2}$$

Constitutive equation:

$$\boldsymbol{\sigma} = \boldsymbol{D} : \boldsymbol{\varepsilon} \tag{4-3}$$

Kinematic equation:

$$\boldsymbol{\varepsilon} = \boldsymbol{\nabla_s u} \tag{4-4}$$

Thus, (4-1) can be rewritten as:

$$\nabla_S^T (\boldsymbol{D} : \nabla_s \boldsymbol{u}) + \boldsymbol{b} = \boldsymbol{0} \tag{4-5}$$

in which,

$$\nabla_S^T = \begin{bmatrix} \partial/\partial x & 0 & 0 & \partial/\partial y & 0 & \partial/\partial z \\ 0 & \partial/\partial y & 0 & \partial/\partial x & \partial/\partial z & 0 \\ 0 & 0 & \partial/\partial z & 0 & \partial/\partial y & \partial/\partial x \end{bmatrix}, \quad \nabla_S = \begin{bmatrix} \partial/\partial x & 0 & 0 \\ 0 & \partial/\partial y & 0 \\ 0 & 0 & \partial/\partial z \\ \partial/\partial y & \partial/\partial x & 0 \\ 0 & \partial/\partial z & \partial/\partial y \\ \partial/\partial z & 0 & \partial/\partial x \end{bmatrix}$$

$$\boldsymbol{\sigma} = \begin{Bmatrix} \sigma_{xx} \\ \sigma_{yy} \\ \sigma_{zz} \\ \tau_{yx} \\ \tau_{yz} \\ \tau_{zx} \end{Bmatrix} \text{ (stress vector), } \boldsymbol{b} = \begin{Bmatrix} b_x \\ b_y \\ b_z \end{Bmatrix} \text{ (force vector), } \boldsymbol{u} = \begin{Bmatrix} u \\ v \\ w \end{Bmatrix} \text{ (displacement vector),}$$

$$\boldsymbol{D} = \begin{bmatrix} D_{11} & D_{12} & D_{13} & D_{14} & D_{15} & D_{16} \\ & D_{22} & D_{23} & D_{24} & D_{25} & D_{26} \\ & & D_{33} & D_{34} & D_{35} & D_{36} \\ & & & D_{44} & D_{45} & D_{46} \\ & \text{sym} & & & D_{55} & D_{56} \\ & & & & & D_{66} \end{bmatrix} \text{ (stiffness matrix)}$$

Boundary condition:

We consider the boundary condition $\Gamma = \Gamma_t \cup \Gamma_u$. In which, Γ_t is the boundary where the traction is prescribed, and Γ_u is the portion of the boundary where the displacement is prescribed. The traction boundary condition is described as:

$$\boldsymbol{n}: \boldsymbol{\sigma} = \bar{\boldsymbol{t}} \text{ on the boundary } \Gamma_t \tag{4-6}$$

in which $\boldsymbol{n}$ is the normal vector.

The displacement boundary condition is described as:

$$\boldsymbol{u} = \bar{\boldsymbol{u}} \text{ on the boundary } \Gamma_u \tag{4-7}$$

4.1.2 Derive weak form from strong form

In Finite Element Method, our purpose is to find an approximate solution of the strong form equation (4-5), with boundary equations (4-6) and (4-7). The approximation solution may not satisfy the partial derivative equation exactly at every point inside the domain. The residual of the solution is:

$$\nabla_S^T (\boldsymbol{D}: \nabla_S \boldsymbol{u}) + \boldsymbol{b} = \boldsymbol{R} \tag{4-8}$$

We want to minimize the residual $\boldsymbol{R}$ by multiplying the (4-8) with a weight function $\boldsymbol{v}^T(x) = [v_1 \ v_2 \ v_3]$ and integrating over the domain. By doing that, we obtain a continuous weak form:

$$\int_{\Omega} \boldsymbol{R} \boldsymbol{v} dx = 0 \tag{4-9}$$

If it satisfies for any $\boldsymbol{v}$ then **R** will approach zero, and the maximum solution will approach the exact solution. In the above equation, $\boldsymbol{v}$ is an arbitrary function, and equation (4-9) has to fulfill for all functions of $\boldsymbol{v}$**.** The arbitrariness of test function $\boldsymbol{v}$ is crucial as otherwise a weak form is not equivalent to the strong form. Now, (4-9) becomes:

$$\int_{\Omega}\left[v^{T}\cdot\nabla_{S}^{T}\left(\boldsymbol{D}:\nabla_{S}\boldsymbol{u}\right)\right]d\Omega+\int_{\Omega}\left(v^{T}\cdot\boldsymbol{b}\right)d\Omega=0 \tag{4-10}$$

Recall the integration by parts:

$$\int_{a}^{b}v\frac{du}{dx}dx=\int_{a}^{b}\frac{d}{dx}(uv)dx-\int_{a}^{b}\frac{dv}{dx}udx \tag{4-11}$$

Also, recall Divergence theorem:

$$\int_{\Omega}\nabla f d\Omega=\int_{S}nfdS \tag{4-12}$$

in which, S is the boundary of the domain Ω, and n is the normal vector of the domain Ω

Firstly, integration by parts is applied to (4-10):

$$\int_{\Omega}\left[\nabla_{S}\left(\boldsymbol{v}^{T}\cdot\boldsymbol{\sigma}\right)\right]d\Omega-\int_{\Omega}\left[\left(\nabla_{S}\boldsymbol{v}\right)^{T}\cdot\left(\boldsymbol{D}:\nabla_{S}\boldsymbol{u}\right)\right]d\Omega+\int_{\Omega}\left(\boldsymbol{v}^{T}\cdot\boldsymbol{b}\right)d\Omega=0 \tag{4-13}$$

Notice that in the above equation is stress tensor [3x3]

Next, Divergence theorem is applied to (4-13):

$$\int_{\Gamma}\left(\boldsymbol{v}^{T}:n:\boldsymbol{\sigma}\right)d\Gamma-\int_{\Omega}\left(\nabla_{S}\boldsymbol{v}\right)^{T}\cdot\left(\boldsymbol{D}:\nabla_{S}\boldsymbol{u}\right)d\Omega+\int_{\Omega}\left(\boldsymbol{v}^{T}\cdot\boldsymbol{b}\right)d\Omega=0 \tag{4-14}$$

Notice that in the above equation has size [6x1]

Because $\Gamma=\Gamma_{t}\cup\Gamma_{u}$, (4-14) becomes:

$$\int_{\Gamma_{u}}\left(\boldsymbol{v}^{T}:n:\boldsymbol{\sigma}\right)d\Gamma_{u}+\int_{\Gamma_{t}}\left(\boldsymbol{v}^{T}:n:\boldsymbol{\sigma}\right)d\Gamma_{t}-\int_{\Omega}\left(\nabla_{S}\boldsymbol{v}\right)^{T}\cdot\left(\boldsymbol{D}:\nabla_{S}\boldsymbol{u}\right)d\Omega+\int_{\Omega}\left(\boldsymbol{v}^{T}\cdot\boldsymbol{b}\right)d\Omega=0 \tag{4-15}$$

As $\boldsymbol{v}$ is arbitrary, we choose $\boldsymbol{v}$ that is vanished on the boundary Γ_{u} .Also, using (4-7) condition, (4-15) is simplified as:

$$\int_{\Gamma_{t}}\left(\boldsymbol{v}^{T}\cdot\bar{t}\right)d\Gamma_{t}-\int_{\Omega}\left(\nabla_{S}\boldsymbol{v}\right)^{T}\cdot\left(\boldsymbol{D}:\nabla_{S}\boldsymbol{u}\right)d\Omega+\int_{\Omega}\left(\boldsymbol{v}^{T}\cdot\boldsymbol{b}\right)d\Omega=0 \tag{4-16}$$

Finally, the continuous weak form is derived as:

$$\underbrace{\int_{\Omega}\left(\nabla_{S}\boldsymbol{v}\right)^{T}\cdot\left(\boldsymbol{D}:\nabla_{S}\boldsymbol{u}\right)d\Omega}_{\alpha(v,u)}=\underbrace{\int_{\Omega}\left(\boldsymbol{v}^{T}\cdot\boldsymbol{b}\right)d\Omega+\int_{\Gamma_{t}}\left(\boldsymbol{v}^{T}\cdot\bar{t}\right)d\Gamma_{t}}_{f(v)} \tag{4-17}$$

The name “weak form” comes from the fact that solutions to the weak form need not to be as smooth as solutions of the strong form, i.e. they have weaker continuity requirements. Furthermore, the second derivative equation in strong form (4-5) is transferred into the first derivative equation in weak form (4-17).

4.1.3 Shape function matrix of elements

Displacement components of element $\boldsymbol{u}^e$ are interpolated from the node displacement $\boldsymbol{d}^e$ through shape function matrix of elements $\boldsymbol{N}^e(x)$:

$$\boldsymbol{u}^e = \boldsymbol{N}^e(\boldsymbol{x})\boldsymbol{d}^e \tag{4-18}$$

in which:

$$\boldsymbol{u}^e = \begin{bmatrix} u_1^e(x) \\ u_2^e(x) \\ \vdots \\ u_{n_d}^e(x) \end{bmatrix} \tag{4-19}$$

In the calculation in FEM, we usually arrange the displacement vector $\boldsymbol{d}^e$ of element Ω^e in the nodal order:

$$\boldsymbol{d}^e = \begin{bmatrix} d_{11}^e \\ d_{21}^e \\ \vdots \\ d_{n_d 1}^e \end{bmatrix} \Big\} n_d \text{ displacement component of node 1} \quad \begin{bmatrix} d_{11}^e \\ d_{21}^e \\ \vdots \\ d_{n_d 1}^e \end{bmatrix} \Big\} n_d \text{ displacement component of node 2} \quad \vdots \quad \begin{bmatrix} d_{11}^e \\ d_{21}^e \\ \vdots \\ d_{n_d 1}^e \end{bmatrix} \Big\} n_d \text{ displacement component of node } n_n \tag{4-20}$$

Shape function $\boldsymbol{N}^e(x)$ matrix of element Ω^e is described as:

$$\boldsymbol{N}^e(x)=\begin{bmatrix} N_1^e(\boldsymbol{x}) & 0 & 0 & 0 & N_2^e(\boldsymbol{x}) & 0 & 0 & 0 & \dots & N_{n_n}^e(\boldsymbol{x}) & 0 & 0 & 0 \\ 0 & N_1^e(\boldsymbol{x}) & 0 & 0 & 0 & N_2^e(\boldsymbol{x}) & 0 & 0 & \dots & 0 & N_{n_n}^e(\boldsymbol{x}) & 0 & 0 \\ \vdots & \vdots & \vdots & \vdots & \vdots & \vdots & \vdots & \vdots & \vdots & \vdots & \vdots & \vdots & \vdots \\ \underbrace{0 \quad 0 \quad 0 \quad N_1^e(\boldsymbol{x})}_{\text{Node 1 (n}_\text{d}\text{ components)}} & & & & \underbrace{0 \quad 0 \quad 0 \quad N_2^e(\boldsymbol{x})}_{\text{Node 1 (n}_\text{d}\text{ components)}} & & & & \dots & \underbrace{0 \quad 0 \quad 0 \quad N_{n_n}^e(\boldsymbol{x})}_{\text{Node } n_n \text{ (n}_\text{d}\text{ components)}} & & & \end{bmatrix} \tag{4-21}$$

Or in concise form:

$$\boldsymbol{N}^e(x)=\begin{bmatrix} \boldsymbol{N}_1^e(x) & \boldsymbol{N}_2^e(x) & \cdots & \boldsymbol{N}_{n_n}^e(x) \end{bmatrix} \tag{4-22}$$

in which $\boldsymbol{N}_I^e(x)$, $I=1,\ 2,\ ...,\ n_n$ is shape function matrix of element Ω^e corresponding to node I:

$$\boldsymbol{N}_I^e(x)=\begin{bmatrix} \boldsymbol{N}_I^e(\boldsymbol{x}) & 0 & \cdots & 0 \\ 0 & \boldsymbol{N}_I^e(\boldsymbol{x}) & \cdots & 0 \\ \vdots & \vdots & \ddots & \vdots \\ 0 & 0 & \cdots & \boldsymbol{N}_I^e(\boldsymbol{x}) \end{bmatrix} \tag{4-23}$$

Strain-displacement matrix of element $\boldsymbol{\varepsilon}^e=\dfrac{d\boldsymbol{u}^e}{d\boldsymbol{x}}=\dfrac{\partial \boldsymbol{N}^e(\boldsymbol{x})}{\partial \boldsymbol{x}}\boldsymbol{d}^e=\boldsymbol{B}^e(\boldsymbol{x})\boldsymbol{d}^e$:

$$\begin{aligned} \boldsymbol{B}^e(x)&=\nabla_S\boldsymbol{N}^e(x)=\begin{bmatrix} \nabla_S\boldsymbol{N}_1^e(x) & \nabla_S\boldsymbol{N}_2^e(x) & \cdots & \nabla_S\boldsymbol{N}_{n_n}^e(x) \end{bmatrix} \\ &=\begin{bmatrix} \boldsymbol{B}_1^e(x) & \boldsymbol{B}_2^e(x) & \cdots & \boldsymbol{N}_{n_n}^e(x) \end{bmatrix} \end{aligned} \tag{4-24}$$

in which $\boldsymbol{B}_I^e(x)$ is strain-displacement matrix of the element corresponding to node I.

4.1.4 Derivation of system equations

From the continuous weak form, we will change it to a discrete one. In other words, instead of finding an unknown function, we want to find "*n*" unknowns. We will need a system of discrete equations, and eventually obtain the system equation in the form: KU = F. K is the stiffness of the system, U is the displacement vector of nodes. F is the vector of forces applied to the systems. The following will describe the process in detail.

Interpolation of displacements by using shape function $\boldsymbol{N}(\boldsymbol{x})$ and nodal displacement, d:

$$\boldsymbol{u}=\boldsymbol{N}(\boldsymbol{x})\boldsymbol{d}=[\boldsymbol{N}_1(\boldsymbol{x})\ \ \boldsymbol{N}_2(\boldsymbol{x})...\boldsymbol{N}_{N_n}(\boldsymbol{x})]\begin{Bmatrix} \boldsymbol{d}_1 \\ \boldsymbol{d}_2 \\ \vdots \\ \boldsymbol{d}_{N_n} \end{Bmatrix} \tag{4-25}$$

Interpolation of strain by using strain-displacement matrix $\boldsymbol{B}(\boldsymbol{x})$:

$$\boldsymbol{\varepsilon} = \frac{d\boldsymbol{u}}{d\boldsymbol{x}} = \frac{\partial \boldsymbol{N}(\boldsymbol{x})}{\partial \boldsymbol{x}}\boldsymbol{d} = \boldsymbol{B}(\boldsymbol{x})\boldsymbol{d} = \begin{bmatrix} \boldsymbol{B}_1(x) & \boldsymbol{B}_2(x) & \dots & \boldsymbol{B}_{N_n}(x) \end{bmatrix} \begin{Bmatrix} \boldsymbol{d}_1 \\ \boldsymbol{d}_2 \\ \vdots \\ \boldsymbol{d}_{N_n} \end{Bmatrix} \tag{4-26}$$

From continuous weak form, we choose N_n test functions $v_1(x), v_2(x), ..., v_{Nn}(x)$. Each function gives one equation, thus, we obtain N_n equations. In Galerkin FEM method, we simply choose the test functions $v_1(x), v_2(x), ..., v_N(x)$ the same as shape functions $N_1(x), N_2(x), ..., N_{N_n}(x)$. Substituting these N_n functions of $v(x)$ into (4-17):

$$\int_{\Omega} (\nabla_S \boldsymbol{N}_I)^T \cdot (\boldsymbol{D} : \nabla_S \boldsymbol{u}) d\Omega = \int_{\Omega} \left(\boldsymbol{N}_I^T \cdot \boldsymbol{b} \right) d\Omega + \int_{\Gamma_t} \left(\boldsymbol{N}_I^T \cdot \bar{\boldsymbol{t}} \right) d\Gamma \tag{4-27}$$

ni which , $\mathrm{I} = 1, 2, ..., \mathrm{N_n}$.

Using $\boldsymbol{B}(\boldsymbol{x}) = \nabla_S \boldsymbol{N}(\boldsymbol{x})$ and substituting (4-26) into (4-27), we obtain,

$$\left(\int_{\Omega} \boldsymbol{B}_I^T : \boldsymbol{D} : \boldsymbol{B} d\Omega \right) d = \int_{\Omega} \left(\boldsymbol{N}_I^T \cdot \boldsymbol{b} \right) d\Omega + \int_{\Gamma_t} \left(\boldsymbol{N}_I^T \cdot \bar{\boldsymbol{t}} \right) d\Gamma, \quad \mathrm{I} = 1, 2, ..., \mathrm{N_n} \tag{4-28}$$

in which the transpose of the global strain-displacement matrix is:

$$\boldsymbol{B}^T = \begin{bmatrix} \boldsymbol{B}_1^T \\ \boldsymbol{B}_2^T \\ \vdots \\ \boldsymbol{B}_{N_n}^T \end{bmatrix} \tag{4-29}$$

We can expand (4-28) into a system of equations:

$$\begin{cases} \left(\int_{\Omega} \boldsymbol{B}_1^T \boldsymbol{D}[\boldsymbol{B}_1\ \boldsymbol{B}_2\ \ldots\ \boldsymbol{B}_{N_n}]\mathrm{d}\Omega\right)\boldsymbol{d} = \int_{\Omega} \boldsymbol{N}_1^T \boldsymbol{b}\ d\Omega + \int_{\Gamma_t} \boldsymbol{N}_1^T \boldsymbol{t}\ d\Gamma \\ \left(\int_{\Omega} \boldsymbol{B}_2^T \boldsymbol{D}[\boldsymbol{B}_1\ \boldsymbol{B}_2\ \ldots\ \boldsymbol{B}_{N_n}]\mathrm{d}\Omega\right)\boldsymbol{d} = \int_{\Omega} \boldsymbol{N}_2^T \boldsymbol{b}\ d\Omega + \int_{\Gamma_t} \boldsymbol{N}_2^T \boldsymbol{t}\ d\Gamma \\ \vdots \\ \left(\int_{\Omega} \boldsymbol{B}_{N_n}^T \boldsymbol{D}[\boldsymbol{B}_1\ \boldsymbol{B}_2\ \ldots\ \boldsymbol{B}_{N_n}]\mathrm{d}\Omega\right)\boldsymbol{d} = \int_{\Omega} \boldsymbol{N}_{N_n}^T \boldsymbol{b}\ d\Omega + \int_{\Gamma_t} \boldsymbol{N}_{N_n}^T \boldsymbol{t}\ d\Gamma \end{cases} \tag{4-30}$$

Or we can write the matrix form of (4-30):

$$\begin{cases} \begin{bmatrix} \int_{\Omega} \boldsymbol{B}_1^T \boldsymbol{D}\boldsymbol{B}_1\,\mathrm{d}\Omega & \int_{\Omega} \boldsymbol{B}_1^T \boldsymbol{D}\boldsymbol{B}_2\,\mathrm{d}\Omega & \cdots & \int_{\Omega} \boldsymbol{B}_1^T \boldsymbol{D}\boldsymbol{B}_{N_n}\,\mathrm{d}\Omega \\ \int_{\Omega} \boldsymbol{B}_2^T \boldsymbol{D}\boldsymbol{B}_1\,\mathrm{d}\Omega & \int_{\Omega} \boldsymbol{B}_2^T \boldsymbol{D}\boldsymbol{B}_2\,\mathrm{d}\Omega & \cdots & \int_{\Omega} \boldsymbol{B}_2^T \boldsymbol{D}\boldsymbol{B}_{N_n}\,\mathrm{d}\Omega \\ \vdots & \vdots & \ddots & \vdots \\ \int_{\Omega} \boldsymbol{B}_{N_n}^T \boldsymbol{D}\boldsymbol{B}_1\,\mathrm{d}\Omega & \int_{\Omega} \boldsymbol{B}_{N_n}^T \boldsymbol{D}\boldsymbol{B}_2\,\mathrm{d}\Omega & \ldots & \int_{\Omega} \boldsymbol{B}_{N_n}^T \boldsymbol{D}\boldsymbol{B}_{N_n}\,\mathrm{d}\Omega \end{bmatrix} \begin{bmatrix} \boldsymbol{d}_1 \\ \boldsymbol{d}_2 \\ \vdots \\ \boldsymbol{d}_N \end{bmatrix} = \begin{bmatrix} \int_{\Omega} \boldsymbol{N}_1^T \boldsymbol{b}\ d\Omega + \int_{\Gamma_t} \boldsymbol{N}_1^T \boldsymbol{t}\ d\Gamma \\ \int_{\Omega} \boldsymbol{N}_2^T \boldsymbol{b}\ d\Omega + \int_{\Gamma_t} \boldsymbol{N}_2^T \boldsymbol{t}\ d\Gamma \\ \vdots \\ \int_{\Omega} \boldsymbol{N}_N^T \boldsymbol{b}\ d\Omega + \int_{\Gamma_t} \boldsymbol{N}_N^T \boldsymbol{t}\ d\Gamma \end{bmatrix} \end{cases} \tag{4-31}$$

Eq. (4-31) can be further simply written as:

$$\boldsymbol{K}\boldsymbol{d} = \boldsymbol{F} \tag{4-32}$$

in which, global stiffness matrix is expressed as:

$$\boldsymbol{K} = \begin{bmatrix} \boldsymbol{K}_{11} & \boldsymbol{K}_{12} & \ldots & \boldsymbol{K}_{1N_n} \\ \boldsymbol{K}_{11} & \boldsymbol{K}_{12} & \ldots & \boldsymbol{K}_{1N_n} \\ \vdots & \vdots & \ddots & \vdots \\ \boldsymbol{K}_{11} & \boldsymbol{K}_{12} & \ldots & \boldsymbol{K}_{1N_n} \end{bmatrix} = \begin{cases} \begin{bmatrix} \int_{\Omega} \boldsymbol{B}_1^T \boldsymbol{D}\boldsymbol{B}_1\,\mathrm{d}\Omega & \int_{\Omega} \boldsymbol{B}_1^T \boldsymbol{D}\boldsymbol{B}_2\,\mathrm{d}\Omega & \cdots & \int_{\Omega} \boldsymbol{B}_1^T \boldsymbol{D}\boldsymbol{B}_{N_n}\,\mathrm{d}\Omega \\ \int_{\Omega} \boldsymbol{B}_2^T \boldsymbol{D}\boldsymbol{B}_1\,\mathrm{d}\Omega & \int_{\Omega} \boldsymbol{B}_2^T \boldsymbol{D}\boldsymbol{B}_2\,\mathrm{d}\Omega & \cdots & \int_{\Omega} \boldsymbol{B}_2^T \boldsymbol{D}\boldsymbol{B}_{N_n}\,\mathrm{d}\Omega \\ \vdots & \vdots & \ddots & \vdots \\ \int_{\Omega} \boldsymbol{B}_{N_n}^T \boldsymbol{D}\boldsymbol{B}_1\,\mathrm{d}\Omega & \int_{\Omega} \boldsymbol{B}_{N_n}^T \boldsymbol{D}\boldsymbol{B}_2\,\mathrm{d}\Omega & \ldots & \int_{\Omega} \boldsymbol{B}_{N_n}^T \boldsymbol{D}\boldsymbol{B}_{N_n}\,\mathrm{d}\Omega \end{bmatrix} \end{cases} \tag{4-33}$$

Force vector is described as:

$$\boldsymbol{f} = \begin{bmatrix} \int_{\Omega} \boldsymbol{N}_1^T \boldsymbol{b}\ d\Omega + \int_{\Gamma_t} \boldsymbol{N}_1^T \boldsymbol{t}\ d\Gamma \\ \int_{\Omega} \boldsymbol{N}_2^T \boldsymbol{b}\ d\Omega + \int_{\Gamma_t} \boldsymbol{N}_2^T \boldsymbol{t}\ d\Gamma \\ \vdots \\ \int_{\Omega} \boldsymbol{N}_N^T \boldsymbol{b}\ d\Omega + \int_{\Gamma_t} \boldsymbol{N}_N^T \boldsymbol{t}\ d\Gamma \end{bmatrix} \tag{4-34}$$

In the calculation of FEM:

$$\boldsymbol{K} = \int_{\Omega} \boldsymbol{B}^T \boldsymbol{D}\boldsymbol{B} d\Omega = \sum_{e=1}^{N_e} \int_{\Omega_e} \boldsymbol{B}^T \boldsymbol{D}\boldsymbol{B} d\Omega \tag{4-35}$$

In FEM, we will calculate the components of stiffness matrix K_{ij} in which $I, J = 1,\ 2,\ \ldots,\ N_n$ based on the elements Ω_e and assemble them together:

$$\boldsymbol{K}_{IJ} = \int_{\Omega} \boldsymbol{B}_I^T \boldsymbol{D}\boldsymbol{B}_J d\Omega = \sum_{e=1}^{N_e} \underbrace{\int_{\Omega_e} \boldsymbol{B}_I^T \boldsymbol{D}\boldsymbol{B}_J d\Omega}_{K_{IJ}^e} \tag{4-36}$$

The calculation of $\boldsymbol{K}_{IJ}^e$ is only based on the element Ω_e, thus, we only consider the component inside the element in the integration, and ignored the others outside. Thus, the element stiffness matrix becomes:

$$\boldsymbol{K}_{IJ}^e = \int_{\Omega_e} \left(\boldsymbol{B}_I^e\right)^T \boldsymbol{D}\boldsymbol{B}_J^e d\Omega \tag{4-37}$$

in which $\boldsymbol{B}_I^e$ is the portion of $\boldsymbol{B}_I$ in the element Ω_e,

$$\boldsymbol{B}_I^e = \nabla_S \boldsymbol{N}_I^e \tag{4-38}$$

Similarly, the force vector is calculated as:

$$\boldsymbol{f}_J = \int_{\Omega} \boldsymbol{N}_J^T \boldsymbol{b}\ d\Omega + \int_{\Gamma_t} \boldsymbol{N}_J^T \boldsymbol{t}\ d\Gamma = \sum_{e=1}^{N_e} \int_{\Omega} \boldsymbol{N}_J^T \boldsymbol{b}\ d\Omega + \int_{\Gamma_t} \boldsymbol{N}_J^T \boldsymbol{t}\ d\Gamma \tag{4-39}$$

The element force vector is expressed as:

$$\boldsymbol{f}_J^e = \int_{\Omega} \boldsymbol{N}_J^T(\boldsymbol{x}) \boldsymbol{b}\ d\Omega + \int_{\Gamma_t} \boldsymbol{N}_J^T(\boldsymbol{x}) \boldsymbol{t}\ d\Gamma \tag{4-40}$$

$$\boldsymbol{f}_J^e = \int_{\Omega_e} \left(\boldsymbol{N}_J^e(\boldsymbol{x})\right)^T \boldsymbol{b}\ d\Omega + \int_{\Gamma_t^e} \left(\boldsymbol{N}_J^e(\boldsymbol{x})\right)^T \boldsymbol{t}\ d\Gamma \tag{4-41}$$

4.2 Volumetric locking introduction

Section 4.1 described the numerical method FEM which is widely used among engineers due to its accuracy and stability. Unfortunately, when dealing with an incompressible material, the displacement based FEM formulation can exhibit an unrealistic stiff behavior. In the similar manner, elastoplastic soil constitutive models in which constant volume is predicted at critical state, also witness this unrealistic stiffness in FEM This is usually known as "volumetric locking" phenomenon (Hughes (2012)). Volumetric locking problem occurs due to Gauss integration, a programming-friendly numerical integration technique in FEM. This volumetric locking occurs when a finite element mesh

with low order element, such as constant strain triangle elements, or Quad4 elements, with full integration to model incompressible material. While simple Quad8 elements or other higher order elements can provide good results for both bending and high incompressibility, they use much more computational cost. To obtain a theoretically accurate solution with less computational cost, several countermeasures have been proposed to address volumetric locking in FEM.

Firstly, Zienkiewicz, Taylor et al. (1971) proposed the reduced integration to resolve this volumetric locking. The idea behind the reduced integration is very simple: because the fully integrated elements cannot satisfy the constant volumetric strain conditions at all the integration points, the number of integration points are reduced to meet the constraints. The slightly loss of accuracy is counteracted by the improvement in approximation to real-life behavior. However, this uniform-reduced integration may lead to the rank deficiency of the stiffness matrix (Hughes, Cohen et al. (1978)) (for instance, in Quad4 element). Thus, the selective reduced integration (SRI) was proposed to overcome this rank deficiency problem (Hughes, Cohen et al. (1978)). The premise in SRI procedure is that we only use reduced integration for the part of the stiffness that locks volumetric stiffness. While the SRI method is very efficient for isotropic elastic materials, in which it is easy to split up the stress into deviatoric and dilational parts, it is not straightforward to apply for the elastoplastic model in which the volumetric and deviatoric parts of the constitutive model are coupled.

4.3 B-bar method

The SRI method is effective to prevent the volumetric locking for incompressible materials, without the effect of the rank deficiency. Nevertheless, this method is only efficient for isotropic elastic materials, it may not be possible to extend the SRI to the case in which the volumetric and deviatoric parts of the constitutive model are coupled. For this reason, another method, called the B-bar method (Hughes (1980)), is commonly used. Similar to SRI method, the B-bar method treats the volumetric and deviatoric part of the stiffness matrix separately.

However, instead of separating the volumetric integral into two parts, the B-bar method modified the definition of the strain in the element. In this B-bar method, while shear strain is calculated with full integration as normal FEM, volumetric strain is calculated with one order lower than that of the standard FEM.

4.3.1 B-bar method formulation:

Recall the element stiffness:

$$\boldsymbol{K}^{e} = \int_{\Omega^{e}} \boldsymbol{B}^{T} \boldsymbol{D} \boldsymbol{B} d\Omega \tag{4-42}$$

in which B is the strain-displacement matrix given as:

$$\boldsymbol{B} = [\boldsymbol{B}_1 \ \boldsymbol{B}_2 \ \ldots \boldsymbol{B}_{nnodes}] \tag{4-43}$$

where n_{en} is the number of element nodes. In 3D analysis, a typical submatrix may be written as:

$$\boldsymbol{B}_a = \begin{bmatrix} B_1 & 0 & 0 \\ 0 & B_2 & 0 \\ 0 & 0 & B_3 \\ B_1 & B_2 & 0 \\ 0 & B_2 & B_3 \\ B_3 & 0 & B_1 \end{bmatrix} \tag{4-44}$$

in which

$$B_i = \partial N_a / \partial x_i, \quad i \le 1 \le 3 \tag{4-45}$$

where, N_a is the shape function associated with node a , and x_i is the i^{th} Cartersian coordinate.

To be able to apply to nearly incompressible cases, these expressions must be modified. Let B_a^{dil} denote the dilational part of $\boldsymbol{B}_a$. The deviatoric part of $\boldsymbol{B}_a$ is then defined by:

$$\boldsymbol{B}_a^{dev} = \boldsymbol{B}_a - \boldsymbol{B}_a^{dil} \tag{4-46}$$

$$\boldsymbol{B}_a^{dev} = \begin{bmatrix} \frac{2}{3}B_1 & -\frac{1}{3}B_2 & -\frac{1}{3}B_3 \\ -\frac{1}{3}B_1 & \frac{2}{3}B_2 & -\frac{1}{3}B_3 \\ -\frac{1}{3}B_1 & -\frac{1}{3}B_2 & \frac{2}{3}B_3 \\ B_2 & B_1 & 0 \\ 0 & B_3 & B_2 \\ B_3 & 0 & B_1 \end{bmatrix} \tag{4-47}$$

To achieve an effective formulation for nearly incompressible application, $\boldsymbol{B}_a^{dil}$ need to be replaced by an "improved" dilational contribution, which we shall denote by $\overline{\boldsymbol{B}}_a^{dil}$:

$$\overline{\boldsymbol{B}}_a^{dil} = \frac{1}{3}\begin{bmatrix} \overline{B}_1 & \overline{B}_2 & \overline{B}_3 \\ \overline{B}_1 & \overline{B}_2 & \overline{B}_3 \\ \overline{B}_1 & \overline{B}_2 & \overline{B}_3 \\ 0 & 0 & 0 \\ 0 & 0 & 0 \\ 0 & 0 & 0 \end{bmatrix} \tag{4-48}$$

Instead of $\boldsymbol{B}_a$, we now use,

$$\overline{\boldsymbol{B}}_a = \boldsymbol{B}_a^{dil} + \overline{\boldsymbol{B}}_a^{dev} \tag{4-49}$$

$$\overline{\boldsymbol{B}}_a = \begin{bmatrix} \frac{1}{3}\overline{B}_1 + \frac{2}{3}B_1 & \frac{1}{3}\overline{B}_2 - \frac{1}{3}B_2 & \frac{1}{3}\overline{B}_3 - \frac{1}{3}B_3 \\ \frac{1}{3}\overline{B}_1 - \frac{1}{3}B_1 & \frac{1}{3}\overline{B}_2 + \frac{2}{3}B_2 & \frac{1}{3}\overline{B}_3 - \frac{1}{3}B_3 \\ \frac{1}{3}\overline{B}_1 - \frac{1}{3}B_1 & \frac{1}{3}\overline{B}_2 - \frac{1}{3}B_2 & \frac{1}{3}\overline{B}_3 - \frac{1}{3}B_3 \\ B_2 & B_1 & 0 \\ 0 & B_3 & B_2 \\ B_3 & 0 & B_1 \end{bmatrix} \tag{4-50}$$

4.3.2 Drawback of B-bar method

If we deal with 2D plane strain problem, by reducing the traditional B-bar method described above from 3D to 2D, then:

$$\varepsilon_{33} = \left(\frac{1}{3}\overline{B}_1 - \frac{1}{3}B_1\right)u_1 + \left(\frac{1}{3}\overline{B}_2 - \frac{1}{3}B_2\right)u_2 + \left(\frac{1}{3}\overline{B}_3 - \frac{1}{3}B_2\right)u_3 \tag{4-51}$$

The condition $\varepsilon_{33} = 0$ is not strictly kept in this way.

4.4 Modified B-bar method for 2D plane strain condition

4.4.1 Formulation

A modified B-bar method for plane strain condition can be developed by modifying the standard B-Bar method which satisfies $\varepsilon_{33} = 0$ condition only in a weak sense. To exactly satisfy $\varepsilon_{33} = 0$ at any point within the element, the B-Bar method can be constructed by replacing $\boldsymbol{B}_{dil}$ matrix by $\boldsymbol{B}_{mean}$ matrix (Commend, Truty et al. (2004)).

$$\boldsymbol{B}_{mean} = \frac{1}{2}\begin{bmatrix} B_1 & B_2 \\ B_1 & B_2 \\ 0 & 0 \end{bmatrix} \tag{4-52}$$

and the $\boldsymbol{B}_{dev}$ and $\overline{\boldsymbol{B}}^{*}$ are expressed as follows:

$$\boldsymbol{B}_{dev} = \begin{bmatrix} \frac{1}{2}B_1 & -\frac{1}{2}B_2 \\ -\frac{1}{2}B_1 & \frac{1}{2}B_2 \\ 0 & 0 \\ B_2 & B_1 \end{bmatrix} \tag{4-53}$$

$$\overline{\boldsymbol{B}}^{*} = \begin{bmatrix} \frac{1}{2}\overline{B}_1 + \frac{1}{2}B_1 & \frac{1}{2}\overline{B}_2 - \frac{1}{2}B_2 \\ \frac{1}{2}\overline{B}_1 - \frac{1}{2}B_1 & \frac{1}{2}\overline{B}_2 + \frac{1}{2}B_2 \\ B_2 & B_1 \end{bmatrix} \tag{4-54}$$

Which corresponds to use of a "modified" mean strain $\varepsilon_m^* = \frac{1}{2}(\varepsilon_1 + \varepsilon_2)$ instead of the standard mean strain $\varepsilon_m = \frac{1}{3}(\varepsilon_1 + \varepsilon_2 + +\varepsilon_3)$.

In 3D form, we can choose B_{mean} and B_{dev} as:

$$\boldsymbol{B}_{mean} = \frac{1}{2}\begin{bmatrix} B_1 & B_2 & B_3 \\ B_1 & B_2 & B_3 \\ 0 & 0 & 0 \\ 0 & 0 & 0 \\ 0 & 0 & 0 \\ 0 & 0 & 0 \end{bmatrix} \tag{4-55}$$

$$\boldsymbol{B}_{dev} = \begin{bmatrix} \frac{1}{2}B_1 & -\frac{1}{2}B_2 & -\frac{1}{2}B_3 \\ -\frac{1}{2}B_1 & \frac{1}{2}B_2 & -\frac{1}{2}B_3 \\ 0 & 0 & B_3 \\ B_2 & B_1 & 0 \\ 0 & B_3 & B_2 \\ B_3 & 0 & B_1 \end{bmatrix} \tag{4-56}$$

At every single point inside the element, this modified B-bar satisfies:

$$e_{kk} = (B_{11}^{dev} + B_{21}^{dev} + B_{31}^{dev})u_1 + (B_{12}^{dev} + B_{22}^{dev} + B_{32}^{dev})u_2 + (B_{13}^{dev} + B_{23}^{dev} + B_{33}^{dev})u_3 = 0 \tag{4-57}$$

$$\varepsilon_{33} = B_3 u_3 = 0 \tag{4-58}$$

Finally, stiffness matrix is calculated as follows:

$$\boldsymbol{K}_{el} = \int_{V_{el}} \overline{\boldsymbol{B}}^T \boldsymbol{D} \overline{\boldsymbol{B}} dV \tag{4-59}$$

Notice that ε_v in the element is everywhere equal to its mean value in B-bar method.

4.4.2 Quad4 element – 2D plane strain – Modified B-bar method

This section presents in detail the modified B-bar matrix of Quad4 element, which is used in this study to analyze the bearing capacity of strip footing. Quad4 element has 4 nodes. Each node has two translation displacements and one rotation displacement. Therefore, the strain-displacement B matrix of Quad4 element is expressed as follows:

$$\boldsymbol{B} = \begin{bmatrix} \frac{\partial N_1}{\partial x} & 0 & \frac{\partial N_2}{\partial x} & 0 & \frac{\partial N_3}{\partial x} & 0 & \frac{\partial N_4}{\partial x} & 0 \\ 0 & \frac{\partial N_1}{\partial y} & 0 & \frac{\partial N_2}{\partial y} & 0 & \frac{\partial N_3}{\partial y} & 0 & \frac{\partial N_4}{\partial y} \\ \frac{\partial N_1}{\partial y} & \frac{\partial N_1}{\partial x} & \frac{\partial N_2}{\partial y} & \frac{\partial N_2}{\partial x} & \frac{\partial N_3}{\partial y} & \frac{\partial N_3}{\partial x} & \frac{\partial N_4}{\partial y} & \frac{\partial N_4}{\partial x} \end{bmatrix} \tag{4-60}$$

When applying modified B-bar method, we separate B matrix into:

$$\boldsymbol{B} = \boldsymbol{B_{dev}} + \boldsymbol{B_{mean}} \tag{4-61}$$

in which,

$$\boldsymbol{B_{dev}} = \begin{bmatrix} \frac{1}{2}\frac{\partial N_1}{\partial x} & -\frac{1}{2}\frac{\partial N_1}{\partial y} & \frac{1}{2}\frac{\partial N_2}{\partial x} & -\frac{1}{2}\frac{\partial N_2}{\partial y} & -\frac{1}{2}\frac{\partial N_3}{\partial x} & -\frac{1}{2}\frac{\partial N_3}{\partial y} & \frac{1}{2}\frac{\partial N_4}{\partial x} & -\frac{1}{2}\frac{\partial N_4}{\partial y} \\ -\frac{1}{2}\frac{\partial N_1}{\partial x} & \frac{1}{2}\frac{\partial N_1}{\partial y} & -\frac{1}{2}\frac{\partial N_2}{\partial x} & \frac{1}{2}\frac{\partial N_2}{\partial y} & -\frac{1}{2}\frac{\partial N_3}{\partial x} & \frac{1}{2}\frac{\partial N_3}{\partial y} & -\frac{1}{2}\frac{\partial N_4}{\partial x} & \frac{1}{2}\frac{\partial N_4}{\partial y} \\ \frac{\partial N_1}{\partial y} & \frac{\partial N_1}{\partial x} & \frac{\partial N_2}{\partial y} & \frac{\partial N_2}{\partial x} & \frac{\partial N_3}{\partial y} & \frac{\partial N_3}{\partial x} & \frac{\partial N_4}{\partial y} & \frac{\partial N_4}{\partial x} \end{bmatrix} \tag{4-62}$$

$$B_{\boldsymbol{mean}} = \begin{bmatrix} \frac{1}{2}\frac{\partial \overline{N}_1}{\partial x} & \frac{1}{2}\frac{\partial \overline{N}_1}{\partial y} & \frac{1}{2}\frac{\partial \overline{N}_2}{\partial x} & \frac{1}{2}\frac{\partial \overline{N}_2}{\partial y} & \frac{1}{2}\frac{\partial \overline{N}_3}{\partial x} & \frac{1}{2}\frac{\partial \overline{N}_3}{\partial y} & \frac{1}{2}\frac{\partial \overline{N}_4}{\partial x} & \frac{1}{2}\frac{\partial \overline{N}_4}{\partial y} \\ \frac{1}{2}\frac{\partial \overline{N}_1}{\partial x} & \frac{1}{2}\frac{\partial N_1}{\partial y} & \frac{1}{2}\frac{\partial \overline{N}_2}{\partial x} & \frac{1}{2}\frac{\partial \overline{N}_2}{\partial y} & \frac{1}{2}\frac{\partial \overline{N}_3}{\partial x} & \frac{1}{2}\frac{\partial \overline{N}_3}{\partial y} & \frac{1}{2}\frac{\partial \overline{N}_4}{\partial x} & \frac{1}{2}\frac{\partial \overline{N}_4}{\partial y} \\ 0 & 0 & 0 & 0 & 0 & 0 & 0 & 0 \end{bmatrix} \tag{4-63}$$

In this thesis, I utilize Quad4 element, in which volumetric strain is integrated with only 1 Gauss point, and shear strain is fully integrated with 4 Gauss point. Take as the reduced rule the one-point Gauss rule, then the value of $\boldsymbol{B_{mean}}$ at any location, (ξ, η). in the interior of the element, is set equal to the value of the specific array at the origin of the element, $(\xi = 0, \eta = 0)$. In other words, the strain-displacement array of the element is defined as follows:

$$\boldsymbol{B}(\xi,\eta) = \boldsymbol{B_{dev}}(\xi,\eta) + \boldsymbol{B_{mean}}(\xi,\eta) = \boldsymbol{B_{dev}}(\xi,\eta) + \boldsymbol{B_{mean}}(0,0) \tag{4-64}$$

Chapter 5 : Analysis of bearing capacity of strip footings on crushable soils

5.1 Validation of the implementation of soil constitutive model considering particle crushing to FEM code

To simulate the bearing capacity of strip footing. our proposed soil model considering particle crushing has been implemented in FEM code. However, the validation of this implementation is needed to be conducted before the simulation of strip footing of bearing capacity. Therefore, in this section, the simulation results of oedometer test between elementary tests and FEM simulations are compared. The Dogs Bays sand parameters calibrated in this research are listed in Table 5-1. The initial soil state condition used in these simulations is also described in Table 5-1.

*Table 5-1: Material parameters of Dog Bays sand and its initial condition for oedometer test simulation**

Parameter	Description	Classification	Value
λ	Compression index		0.265
κ	Recompression index		0.0015
N	Specific volume on NCL at p = 98 kPa	Modified Cam Clay	1.8
M	Critical stress ratio		1.65
ν	Poisson ratio		0.2
a	Parameter controlling density effect	Subloading Concept	500
p_r	Parameter controlling crushing resistance	Particle Crushing	5000
M_x	Parameter controlling the shape of crushing surface		0.58
ξ	Volumetric distance between NCL of I_G = 0 and I_G = 1		0.55
p_{x0}	Crushing stress when I_G = 0: (kN/m^2)		98

* These material parameters of Dogs Bay Sand were calibrated from the elementary triaxial tests. The initial soil state (e_0 = 1.75, p_0 = 98 kPa, I_{G0} = 0)

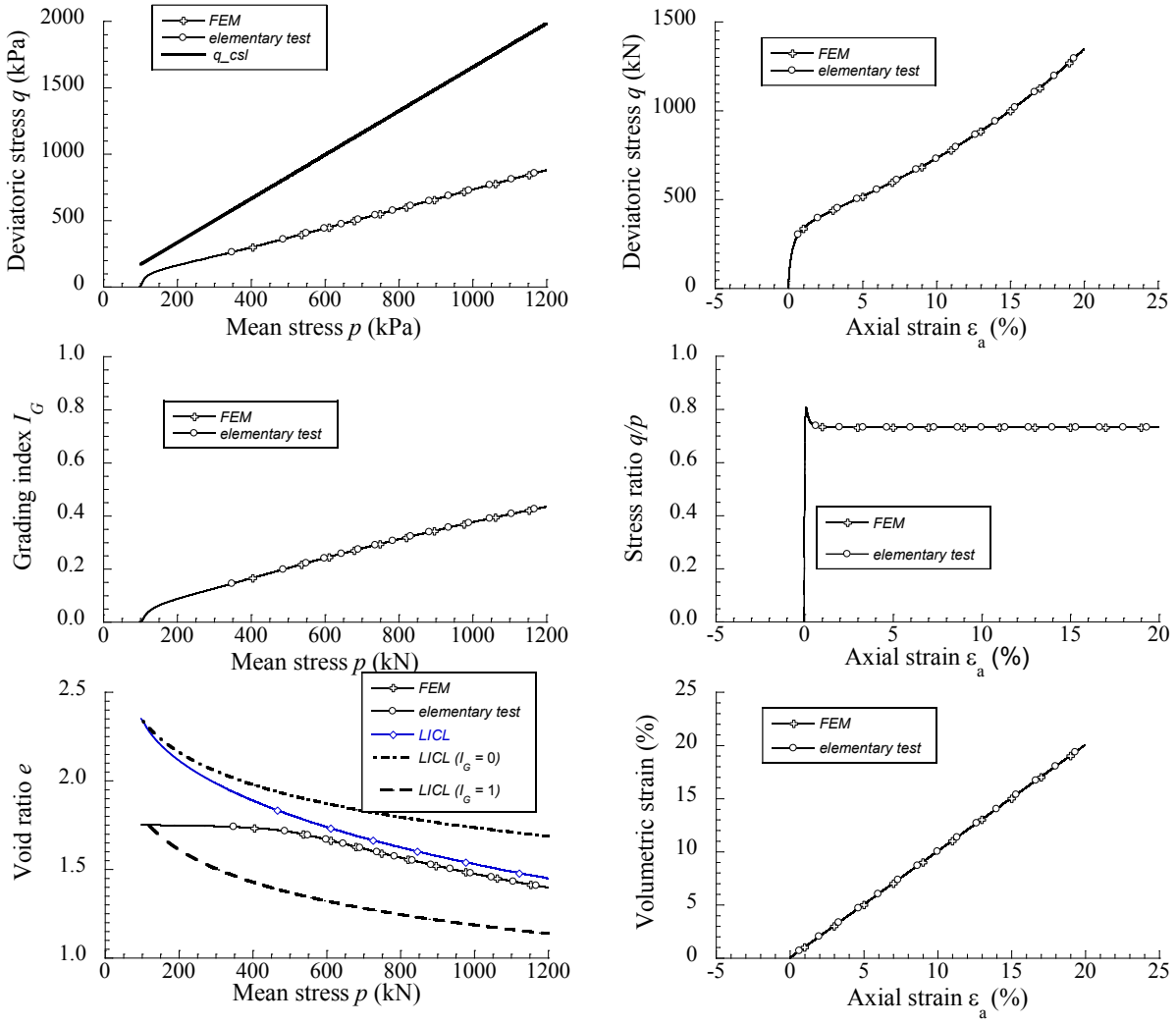

Figure 5-1: Comparison of elementary test and FEM simulation of oedometer test using particle crushing constitutive model

As can be observed from Figure 5-1, the simulations of oedometer test from both elementary simulations and FEM simulations generated the same results in stress-strain behavior. Also, the same evolution of I_G when mean stress increases were observed in this figure. Thus, our proposed soil constitutive model considering particle crushing has been successfully implemented into FEM code.

5.2. Analysis of strip footing bearing capacity on crushable soil

The bearing capacity analysis is carried out by using our proposed model for soil considering particle crushing, and the finite element method is used for solving nonlinear equations with boundary conditions. The soil medium is discretized by Quad4 element. A typical finite element mesh used is shown in Figure 5-2. It consists of 1080 Quad4 elements with the courser mesh near the edge of the footing. The nodes representing the footing width are incrementally displaced by an equal amount in the vertical direction, simulating a rigid footing condition with a uniform vertical settlement but without any rotation. Smooth footing conditions are simulated by not restraining horizontal movement of these nodes. The footing load for each increment is the summation of the nodal forces back-computed from the conversed stress field after each increment.

*Table 5-2: Material parameters of Dogs Bay sand and its initial condition for strip footing bearing capacity analysis**

Parameter	Description	Classification	Value
λ	Compression index	Modified Cam Clay	0.265
κ	Recompression index		0.0015
N	Specific volume on NCL at p = 98 kPa		1.8
M	Critical stress ratio		1.65
ν	Poisson ratio		0.2
a	Parameter controlling density effect	Subloading Concept	500
p_r	Parameter controlling crushing resistance	Particle Crushing	5000
M_x	Parameter controlling the shape of crushing surface		0.58
ξ	Volumetric distance between NCL of I_G = 0 and I_G = 1		0.55
p_{x0}	Crushing stress when I_G = 0: (kN/m^2)		98

* These material parameters of Dogs Bay Sand were calibrated from the validation of elementary tests. The unit weight (γ = 18 kN/m^3) is applied by the gravity load with the initial soil state (e_0 = 2.5, p_0 = 0.01 kPa, I_{G0} = 0) before applying the loading process.

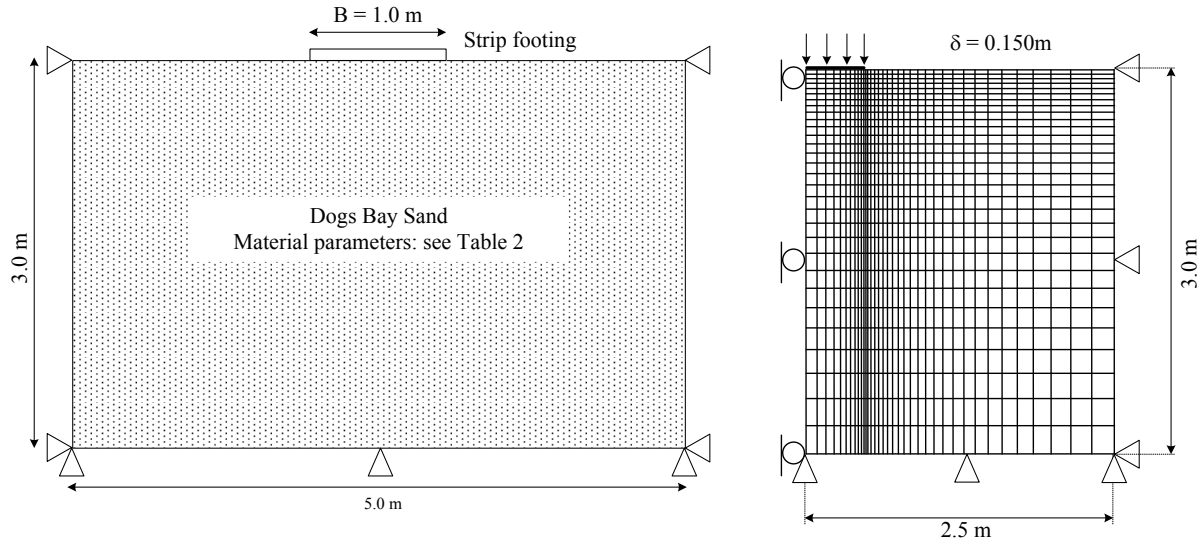

Figure 5-2: Analytical domain, boundary conditions, and grid mesh (1080 elements) of strip footing

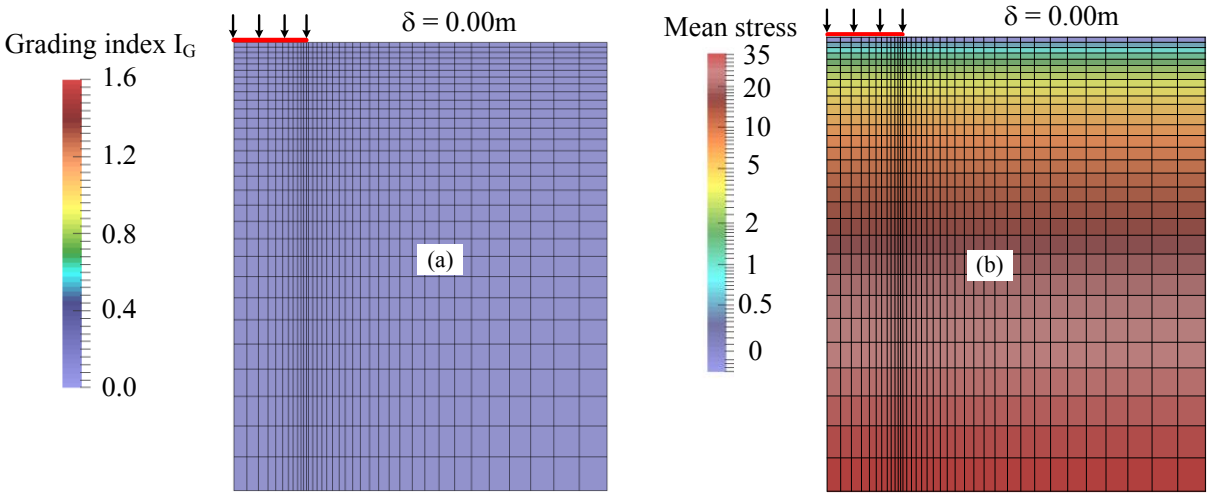

Figure 5-3: Stress generalization before loading and distribution of the initial value of I_G

5.2.1 Soil self-weight generation

In this simulation, the soil unit weight (γ = 18 kN) was applied by the gravity load with the initial soil state (e_0 = 2.5, p_0 = 0.01 kPa, I_{G0} = 0) before applying the loading process to the footing. The phase after generating soil self-weight was shown in Figure 5-3 with the initial uncrushed state I_{G0} = 0 at all elements and the mean stress variation with depth). The soil self-weight generation process was checked by comparing the sum of the reaction forces in the vertical axis with the magnitude of $\gamma.S$, in which S is the area of the domain.

5.2.1 Mesh density and number of calculation steps

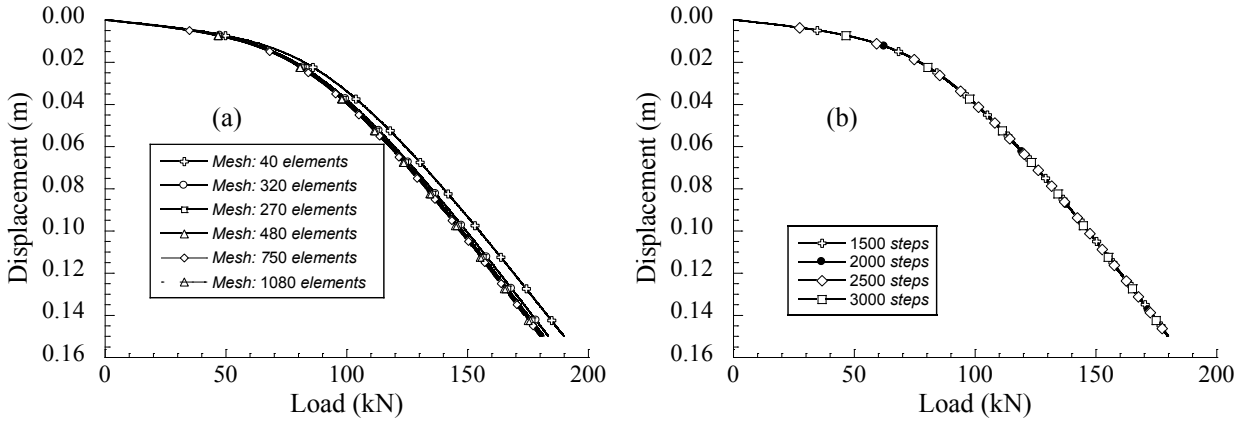

Figure 5-4 : Load-displacement curve of strip footing B = 1m, with a variation of (a) The number of elements (with 2500 calculation steps) (b) The number of steps (with 1080 elements)

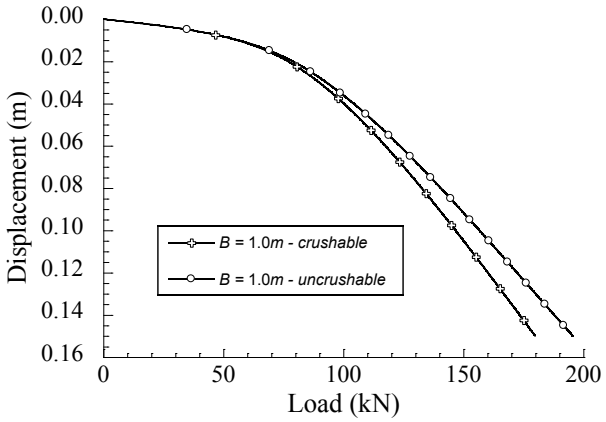

Figure 5-5: A comparison of the load-displacement curve of strip footing on crushable and uncrushable soil

The load-displacement curve was analyzed with the same 2500 calculation steps with a variety of meshes in which the number of elements varies from 40 to 1080, are shown in Figure 5-4a. It could be seen from this figure that the simulation result was converging as the number of elements is large enough. Furthermore, the number of steps also vary from 1500 to 3000 with 1080 elements, and they still showed the same result (Figure 5-4b). The same result was due to the effect of subloading concept, in which plastic strain occurs immediately at the loading time, which was much more stable than that of the VonMises model where there is a sudden change between elastic and plastic region. Thus, the number of calculation steps does not have a significant effect on the calculation result of our model.

5.2.3 Strip footing bearing capacity analysis of Dogs Bay Sand

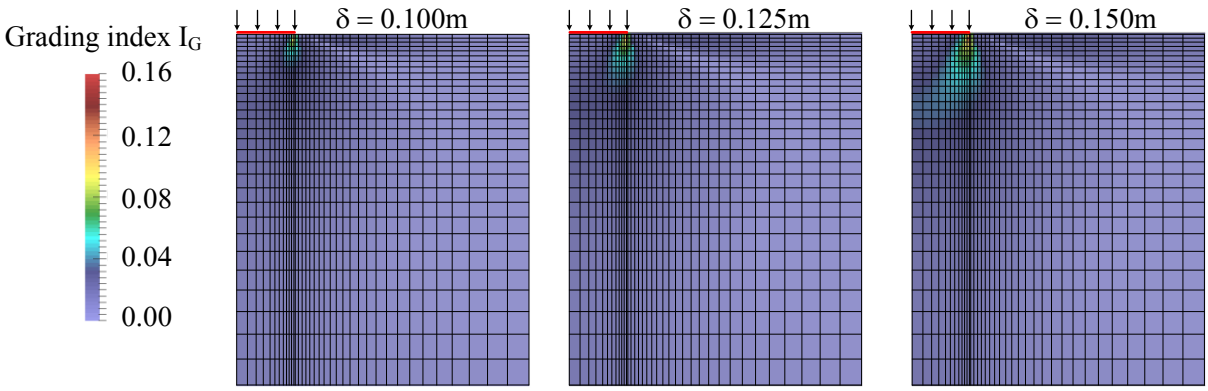

Figure 5-6: I_G distribution with the variation of settlement δ

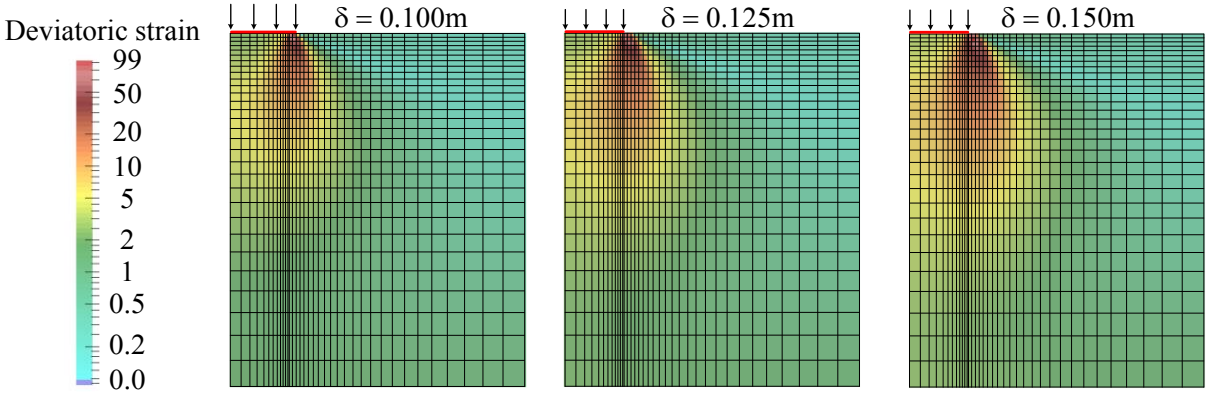

Figure 5-7: Deviatoric stress distribution with the variation of settlement δ

The bearing capacity of strip footing on Dogs Bay sand when considering and not considering particle crushing behavior was shown in Figure 5-5. It can be observed from the figure that bearing capacity reduced when particle crushing phenomenon occurred, and a larger load application resulting more crushing.

Figure 5-6 showed the distribution of grading index, I_G within the considered domain with different level of displacements. We can see that, the more displacement of the footing resulted in the clear evolution of I_G. Furthermore, the area at the edge of the footing exhibit the highest magnitude of I_G. Figure 5-7 revealed the deviatoric strain distribution in the domain with different settlement level of strip footing. The simulation results showed that only punching failure was observed with Dogs Bay sand parameters. As a result, the ultimate bearing capacity was not obtained in these simulations, but the bearing capacity only increased with the increase in displacement. The grid displacement, displacement vector of element nodes and the direction of principle stresses were shown in Figure 5-8.

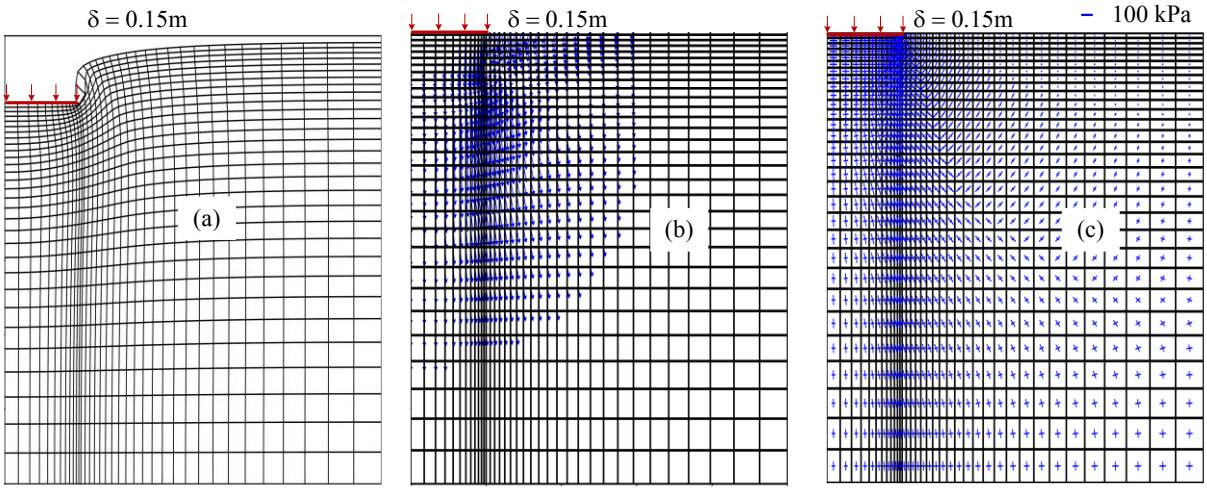

Figure 5-8: Displacement and principle stress result with 1080 elements. (a) Grid displacement (scale 4 times) (b) Displacement vector and nodes of elements (c) Principle stress: direction and magnitude

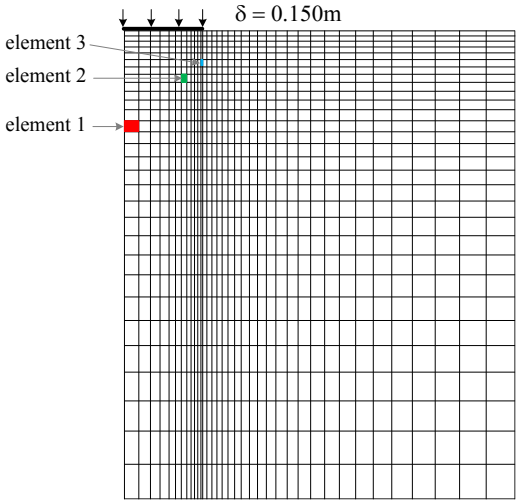

Figure 5-9: Grid mesh and position of analyzed elements 1, 2 and 3 under loading

To further explore the behavior of strip footing bearing analysis, the stress-strain and stress-grading index of element 1, 2, and 3 (Figure 5-9) were examined. Element 3 was near the edge of strip footing, while element 1 was located in the middle of the footing. Firstly, from Figure 5-10, element 3 near the footing suffered the highest shearing stress among the three elements. Element 2 has the largest mean stress among the three. Even though the soil state before the loading simulation is overconsolidated soil (Figure 5-11), all of the elements did not reach the critical state when the settlement reached 0.15 m (Figure 5-10). Thus, the soil element is still being compressed under loading condition, and the ground failure is just a punching failure mode, not general failure mode. In this Dogs Bay sand, the effect of shearing stress to particle crushing was more significant than the mean stress ($M_x = 0.58$).

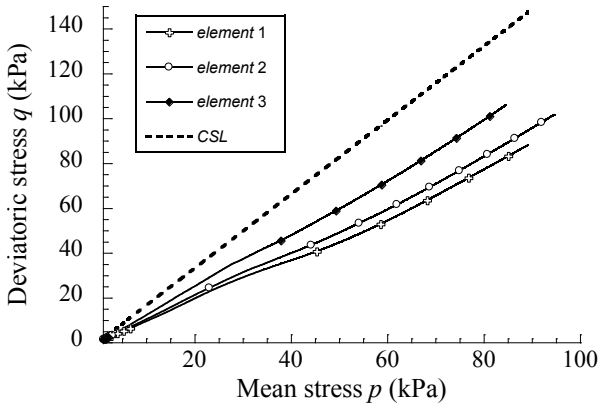

Figure 5-10: Stress paths of elements 1, 2 and 3 under loading

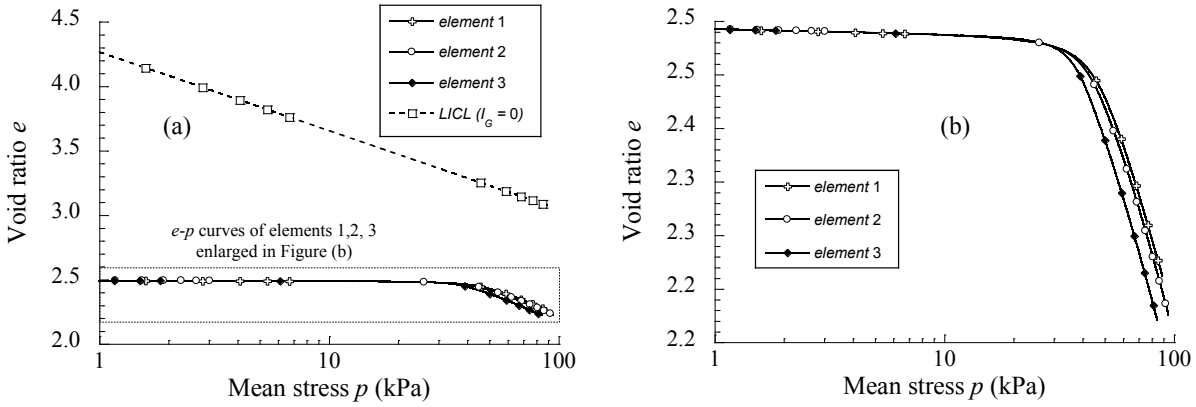

Figure 5-11: Variation of void ratio e and mean stress p of elements 1, 2, 3 under loading

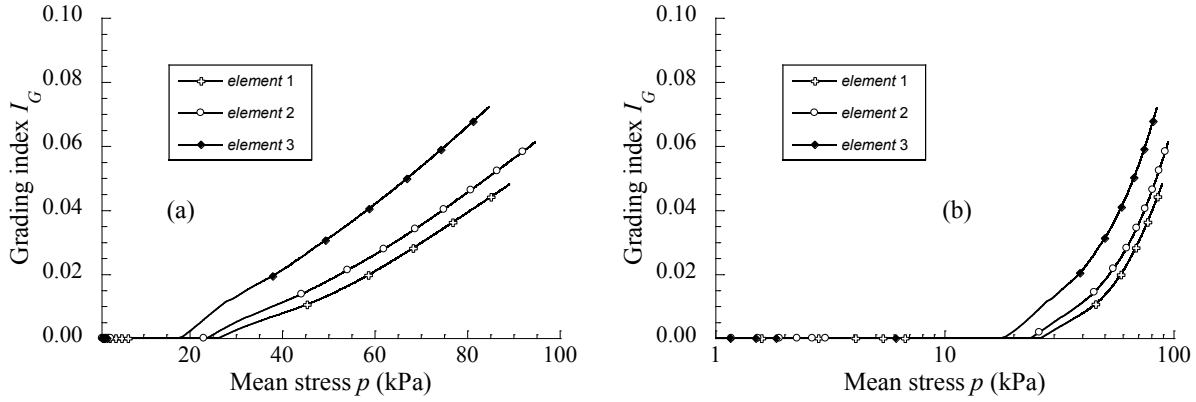

Figure 5-12: Variation of grading index I_G versus mean stress p of elements 1, 2 and 3 under loading

Figure 5-12 showed that I_G of element 3 was the largest among the three elements. Furthermore, due to the highest crushing suffering, the void ratio in element 3 decreases smallest at the final step of simulation. In other words, element 3 had the highest density because of the most serious crushing exposure.

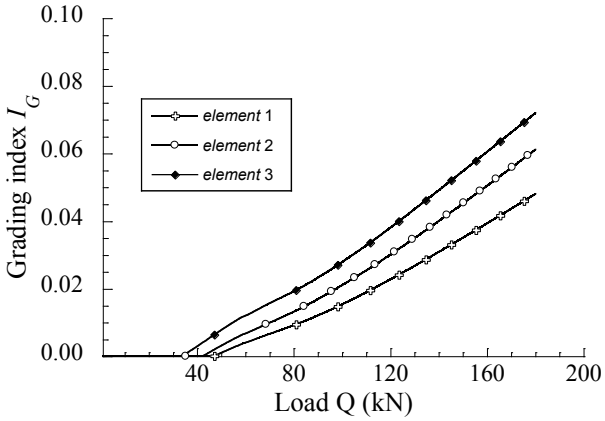

Figure 5-13: Variation of grading index I_G at element 1, 2, 3

Figure 5-13 showed the relation between the bearing capacity and grading index, I_G at element 1, 2 and 3. It could be seen from the figure that after particle crushing has been initiated, the more crushing is observed when more load is applied. Also, the point located near the edge of strip footing exhibited more crushing than the elements far away from the footing edges.

5.3 Parametric studies of the material parameters

In the parametric studies below, the material parameters for Modified Cam clay, subloading effect, self-weight γ are kept constant. Only the parameters controlling particle crushing mechanism are varied systematically.

5.3.1 Initial crushing under isotropic compression stress

Regarding the unit grading of soil (I_G = 0), under isotropic confining pressure, the magnitude of stress required for the onset of crushing depends on the parameter p_{x0}. Thus, soils that are sensitive to crushing when suffering confining pressure will possess a small value of p_{x0}. With a smaller value of p_{x0}, the crushing phenomenon occurs earlier (during the loading process), which leads to the reduction of the strength or stiffness of the soil sooner. Similar case occurs in the simulation of strip footing bearing capacity, a smaller value of p_{x0} will lead to the sooner occurrence of particle crushing, which leads to the sooner reduction in the soil strength during the loading. This results in a smaller bearing capacity in case of a smaller value of p_{x0} (Figure 5-14). In our model, when p_{x0} is sufficiently large, the bearing capacity of soil considering crushing effect will approach the bearing capacity of soil when not considering particle crushing effect.

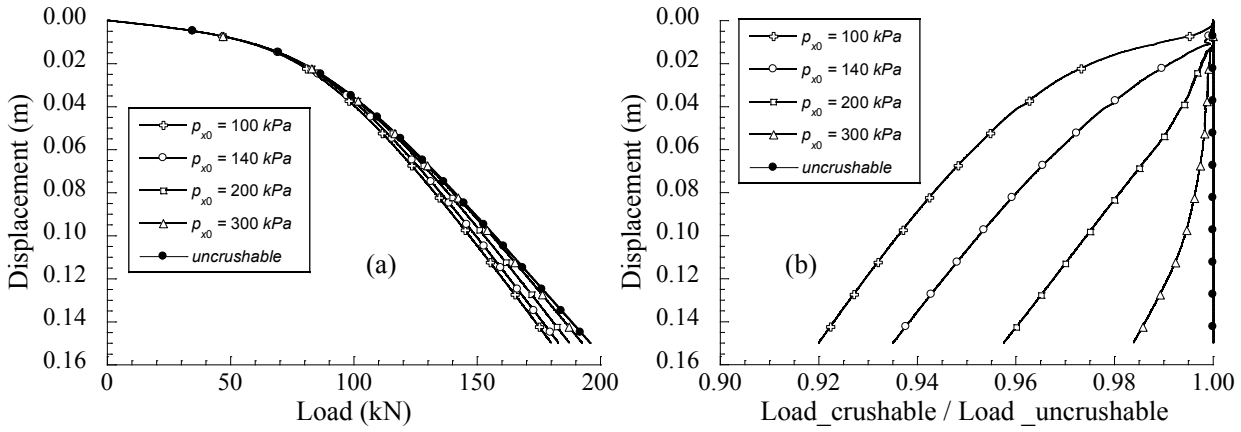

Figure 5-14: The effect of p_{x0} parameter (crushing stress corresponding to I_G = 0) on the bearing capacity of strip footing on crushable soil (a) Load-displacement curve (b) Normalization of bearing capacity considering and not considering crushing effect

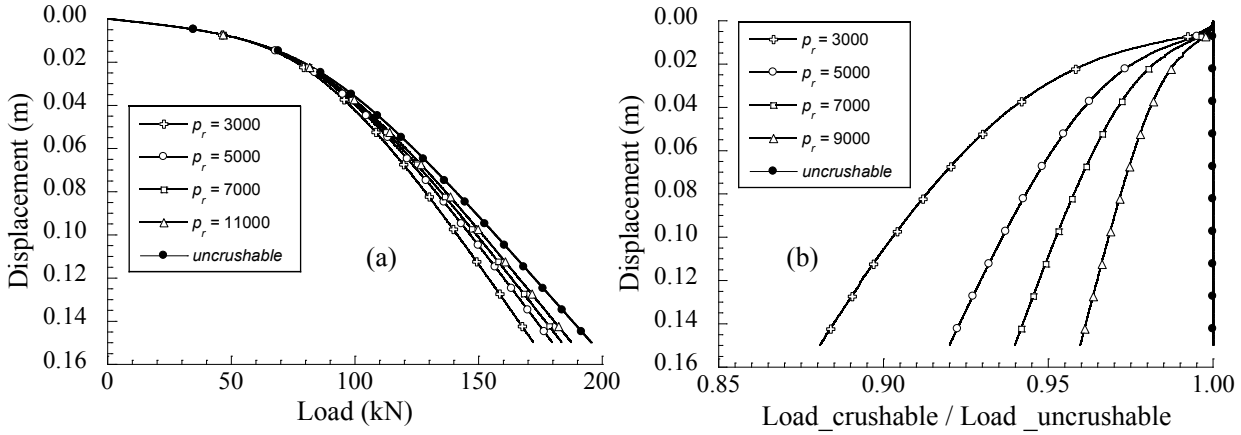

Figure 5-15: The effect of p_r parameter on the bearing capacity of strip footing on crushable soil (a) Load-displacement curve (b) Normalization of bearing capacity considering and not considering crushing effect

5.3.2 Particle crushing resistance

Figure 5-15 shows the effect of particle crushing resistance parameter p_r to the bearing capacity of strip footing on crushable soil by variating a wide range of p_r from 3000 to 9000. In our constitutive model, After the crushing phenomenon has been initiated, the resistance to crushing parameter p_r, controls the evolution rate from the original PSD to the critical PSD. In other words, p_r governs the speed of crushing in the soil. A larger the value of p_r results in a slower rate of crushing occurs. High level of crushing the weakens the soil; therefore, the larger the value of p_r is, the closer the bearing capacity considering particle crushing effect is to the bearing capacity when particle crushing is not

considered. Regarding Dogs Bay sand, p_r is calibrated to be 5000, and the bearing capacity of Dogs Bay sand when considering crushing
effect is approximately 86% to 96% of the bearing capacity when not considering crushing effect. However, when p_r is large enough, crushing effect is prevented and bearing capacity will approach the bearing capacity when not considering crushing effect.

5.3.3 Effect of shearing stress on the initiation of crushing

Figure 5-16 showed how M_x, the parameter controls the simultaneous effect of shearing and compression stresses, through crushing surface shape, on the bearing capacity of strip footing on the crushable soils. It should be noticed that the onset of crushing depends on the simultaneous effect of mean stress and deviator stress. In our crushing soil model, this combination effect is simply but effectively implemented via the crushing surface: under the same mean stress, the larger M_x is, the more significant deviator stress needs to be applied to initiate crushing. Therefore, under the same confining pressure, the soils that are strong in crushing resistance to deviator stress will have a larger magnitude of M_x compared to that of the weak one. From the above analysis, the larger the value of M_x, the larger bearing capacity the soil can sustain. It should be noticed that even for an infinitely large number of M_x, the bearing capacity when considering crushing effect also cannot reach the bearing capacity when not considering crushing effect. A large value of M_x means that the deviatoric stress is not dominant in the initiation of crushing. However, due to the effect of mean stress in the crushing surface, when the small value of p_{x0} is set to a small value, then crushing will always occur irrespective of M_x.

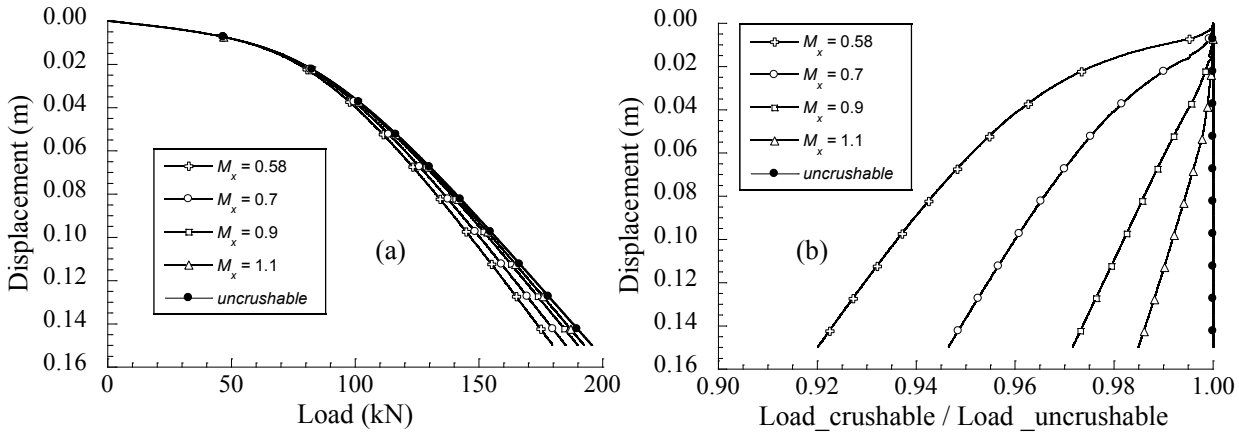

Figure 5-16: The effect of M_x parameter on the bearing capacity of strip footing on crushable soil. (a) Load-displacement curve (b) Normalization of bearing capacity of crushable over uncrushable soil

5.4 Effect of the width of strip footing

The particle crushing effect significantly influences the strip footing bearing capacity. To be more specific, the bearing capacity of the crushed soil was around 90-92% of the bearing capacity of uncrushed soil (Figure 5-17, Figure 5-18), in case of using Dogs Bay sand parameters.

As seen in Figure 5-17 and Figure 5-18, within the assumed limit allowable settlement (0.15 m), to achieve a higher bearing capacity, we can increase the size of strip footing. Also, noticed from (Figure 5-18), when the width of the foundation was increased 2.5 times (from 1 1.0 m to 2.5 m), the bearing capacity of strip footing on crushable soil was only reduced around 2% when being normalized with the bearing capacity of strip footing on crushable soil. Thus, the particle crushing effect was slightly reduced when the footing size increased.

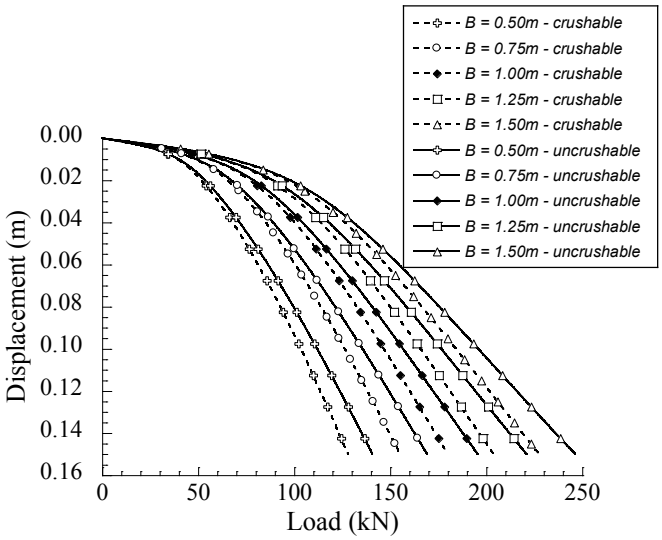

Figure 5-17: The bearing capacity of the strip footing with variation footing sizes on crushable and uncrushable soils

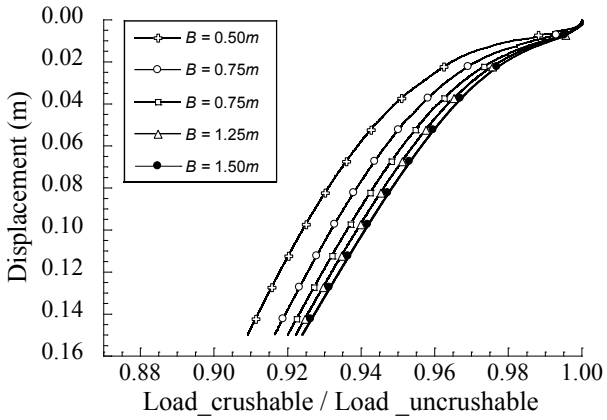

Figure 5-18: Normalization of the bearing capacity of the strip footing on crushed soil with that of uncrushed soil with various widths of foundation

5.5 Scale effect

Experimental data collected by De Beer (1965) have clearly shown that the bearing capacity factor N_γ decreases with an increase in the size of foundation. Experiments carried out in a centrifuge demonstrated that the magnitude of N_γ increased almost linearly with a decrease in footing size on a *log-log* scale (Kutter, Abghari et al. (1988); Clark (1998); Ueno (1994)). As a result, model footings always overpredict the bearing capacity factor N_γ as compared to field footings. The dependency of N_γ on footing width (B) was found to be primarily due to the pressure level effect (Tatsuoka (1991), Tatsuoka (1994)), which caused the reduction of peak friction angle (which is the arcsine of the peak value of $(\sigma_1 - \sigma_3)/(\sigma_1 - \sigma_3)$ when the applied pressure becomes larger. In this simulation of Dogs Bay sand with a high value of critical state ratio (M = 1.65), the general failure did not occur, but only punching failure mode did. In this work, we tried to analyze the bearing capacity factor in the same manner, when choosing the bearing capacity at the displacement of 0 15m as the "ultimate" bearing capacity.

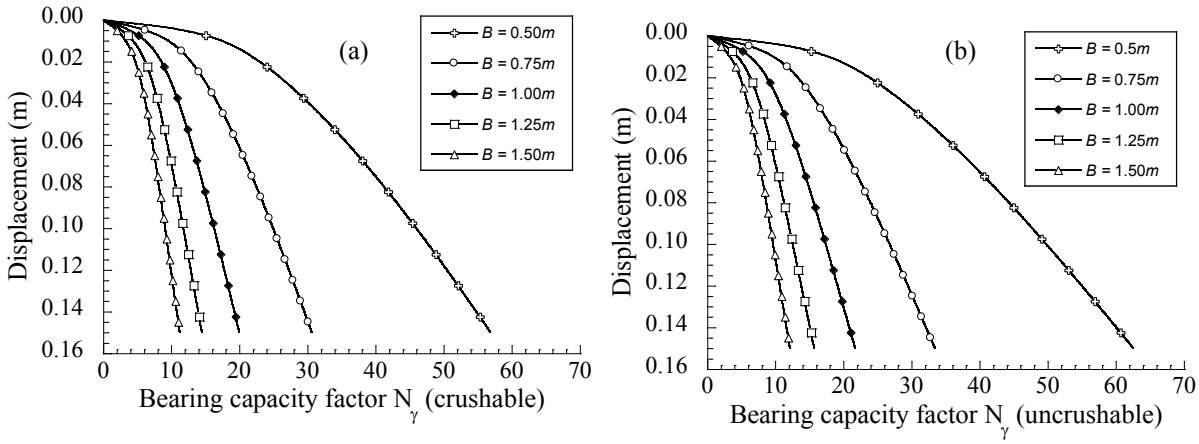

Figure 5-19: Variation with depth of bearing capacity factor N_γ on: (a) uncrushable soil (b) crushable soil

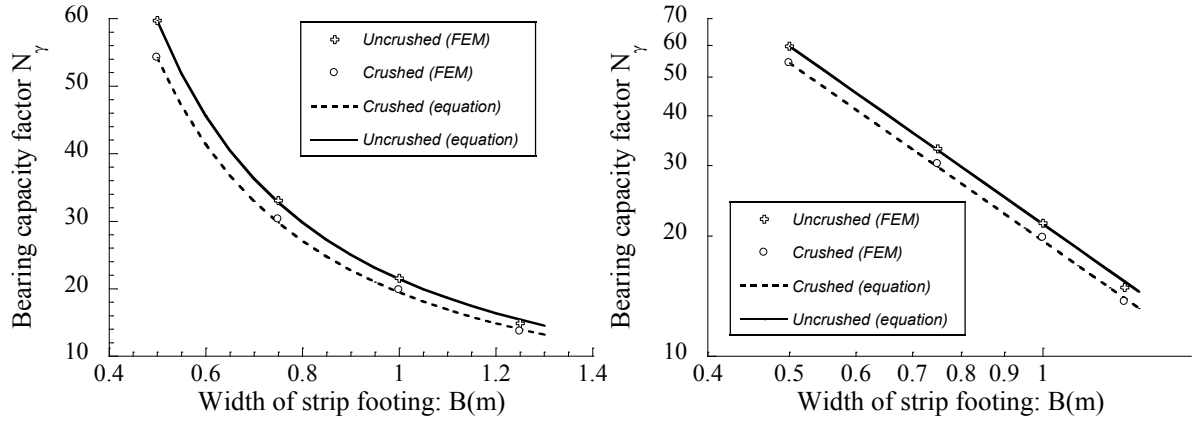

Figure 5-20 : Comparison of the variation of bearing capacity factor N_γ with footing width B between FEM simulation and equation. (a) linear-linear scale (b) log_{10}-log_{10} scale

Shiraishi (1990) developed the following empirical expression for determining N_γ

$$N_\gamma = N_\gamma^* \left(\frac{B}{B^*}\right)^{-\beta}$$

where, N_γ = reference bearing capacity factor; B^*= reference footing width; and β = factor to account for the dependency of N_γ on the confining stress level. In this simulation with Dogs Bay sand, B^*= 0.5m, β = 1.49 are the optimum parameters to obtain appropriate results. (Figure 5-20).

An interesting finding was that the bearing capacity factors N_γ of crushable soil and uncrushable soil were almost straight lines in log-log scale of N_γ -B (same as the other researcher findings). Furthermore, these lines were parallel to each other, which suggest a downward shift of N_γ on crushable to N_γ of uncrushable soil. This finding was useful for the design of strip footing because the ratio between the bearing capacity of strip footing on crushable soil can be conveniently calculated from the bearing capacity on uncrushable soil by multiplying a factor (N_γ crushable/ N_γ uncrushable).

=

Chapter 6 : Active and passive earth pressure coefficient analysis on crushable soils

In this chapter, we will examine the effect of particle crushing on the active and passive earth pressure coefficients through the simulation of retaining wall using our proposed model for crushable soils. To achieve this purpose, firstly, our FEM code to simulate the active and passive earth pressure problem is validated with Drucker-Prager model and then compared the results with analytical results by Rankine. Then, the proposed soil model for crushable soil is used to study the effect of particle crushing on the variation of active and passive earth pressure.

6.1 Validation of the FEM code to the problem of active and passive earth pressure analysis by Drucker-Prager criteria

6.1.1 Drucker-Prager yield function:

A yield function of Drucker Prager:

$$f = -\alpha J_1 + J_2^{1/2} - k \tag{6-1}$$

where α and k are positive constants. J_1 is the sum of principle stresses:

$$J_1 = \sigma_{11} + \sigma_{22} + \sigma_{33} \tag{6-2}$$

J_2 is the second invariant of the stress deviation:

$$J_2 = \frac{1}{6}[(\sigma_{11} - \sigma_{22})^2 + (\sigma_{22} - \sigma_{33})^2 + (\sigma_{33} - \sigma_{11})^2] + \sigma_{12}^2 + \sigma_{23}^2 + \sigma_{31}^2 \tag{6-3}$$

6.1.2 Calibrate Drucker-Prager model parameters for Mohr-Coulomb criteria in plane strain condition

To be able to compared with Rankine earth pressure, we need to use Mohr Coulomb yield criteria. However, the yield function of Drucker-Prager can be reduced to the Mohr Coulomb rule in the case of plane strain condition (Drucker and Prager, 1952 or Appendix C in this thesis)

$$\alpha = \frac{sin\phi}{\sqrt{3}\sqrt{3 + sin^2\phi}} \tag{6-4}$$

$$k = \frac{\sqrt{3}c.cos\phi}{\sqrt{3 + sin^2\phi}} \tag{6-5}$$

6.1.3 Domain & boundary condition

The domain considered in this research is a rectangle area of 4x14m (Figure 6-1). The material parameters are displaced in Table 6.1 The bottom of the domain is restrained with the horizontal and vertical displacements. The left hand side of the domain is restrained by the horizontal displacement. The active and passive earth pressure coefficient analysis are carried out by using Drucker Prager model with material parameters calibrated from Mohr Coulomb model for plane strain condition. FEM is used for solving nonlinear equations with boundary conditions. The analysis domain is discrete by Quad4 element. A finite element mesh of 400 elements is shown in Figure 6-1. The nodes representing the retaining wall are incrementally displaced by an equal amount in the horizontal direction, simulating a rigid wall condition with uniform horizontal displacement. Smooth retaining wall conditions are simulated by not restraining vertical movement of these nodes. The initial stress in the soil elements are generated by k0 initialization. The mean stress distribution is shown in Figure 6-2

The total of pressure acting on the retaining wall is calculated as the integration of the average horizontal stress acting on the wall. To be convenient for calculation, we use passive or active coefficients K_p, K_a, respectively.

$$P_{p,a} = \frac{1}{2} K_{p,a} \gamma H^2, or\ K_{p,a} = 2P_{p,a}/(\gamma H^2) \tag{6-6}$$

Analytical solution of Rankine active and passive earth pressure coefficients:

$$K_p = \tan^2\left(45^0 + \frac{\phi}{2}\right) = 3 \tag{6-7}$$

$$K_a = \tan^2\left(45^0 - \frac{\phi}{2}\right) = \frac{1}{3} \tag{6-8}$$

Table 6-1: Material parameter for Drucker Prager model

Parameter	Description	Value
E	Young's modulus	70000
ν	Poisson ratio	0.499
c	Cohesion	0
ϕ	Friction angle	30^0

* The unit weight (γ = 18 kN/m^3) is applied by k_0 distribution with k_0 = 0.5 before applying the loading process.

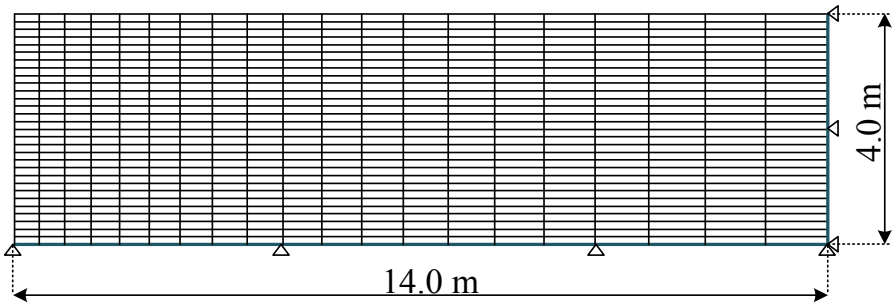

Figure 6-1: A mesh of 400 elements

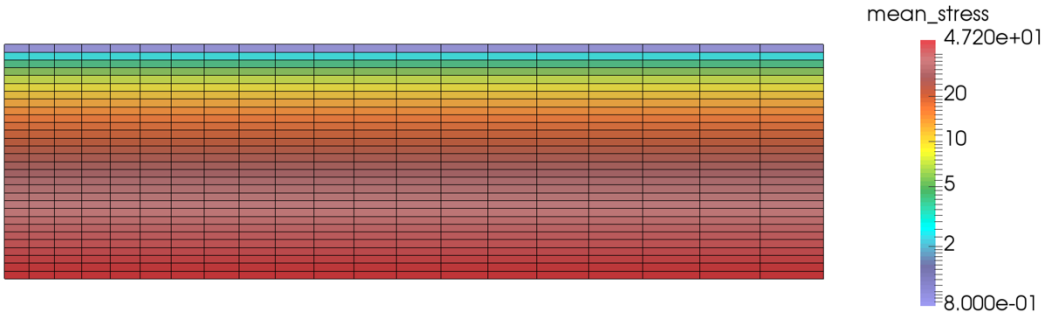

Figure 6-2: Distribution of mean stress due to self-weight with k0 initialization

Analytical solution of Rankine active and passive earth pressure coefficients:

$$K_p = \tan^2\left(45^0 + \frac{\phi}{2}\right) = 3 \tag{6-11}$$

$$K_a = \tan^2\left(45^0 - \frac{\phi}{2}\right) = \frac{1}{3} \tag{6-12}$$

6.1.4 Simulation results

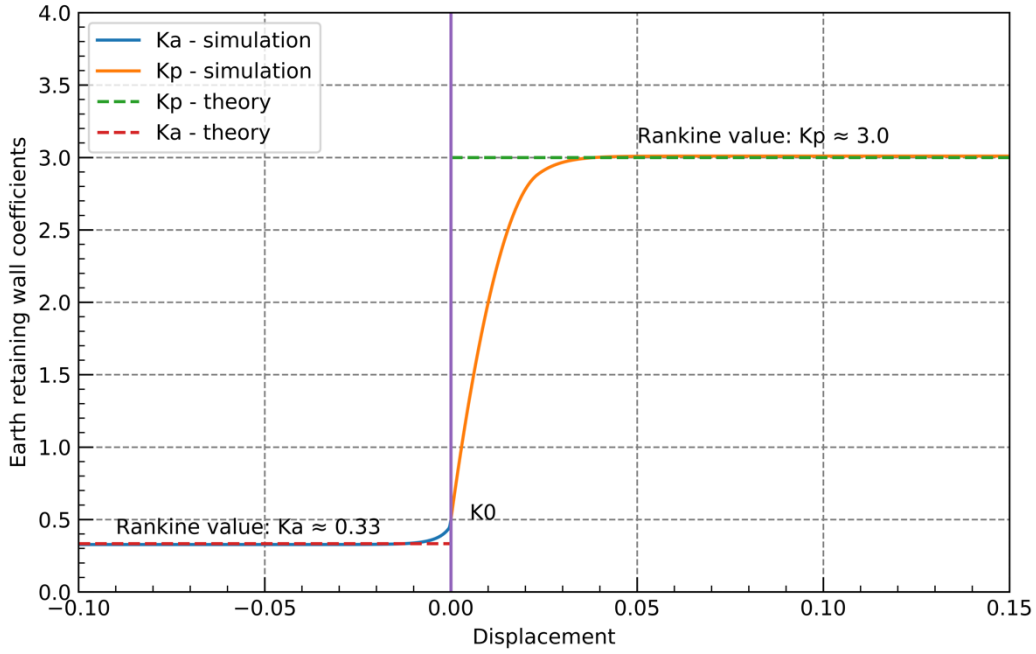

Figure 6-3: Active and passive coefficient earth pressure analysis with Drucker Prager model

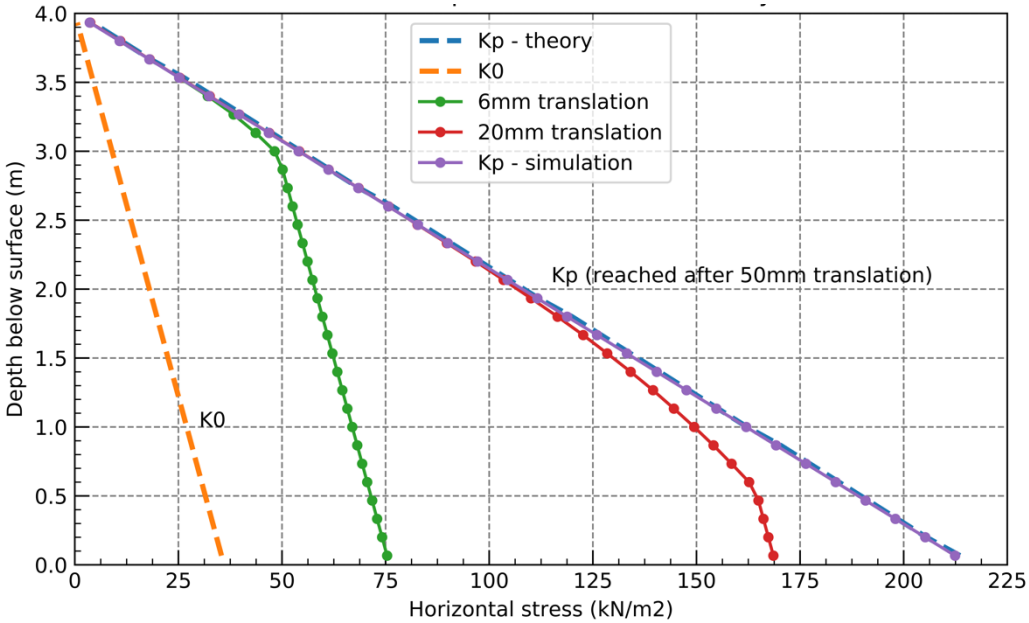

Figure 6-4: Earth pressure distribution for Drucker-Prager, passive case

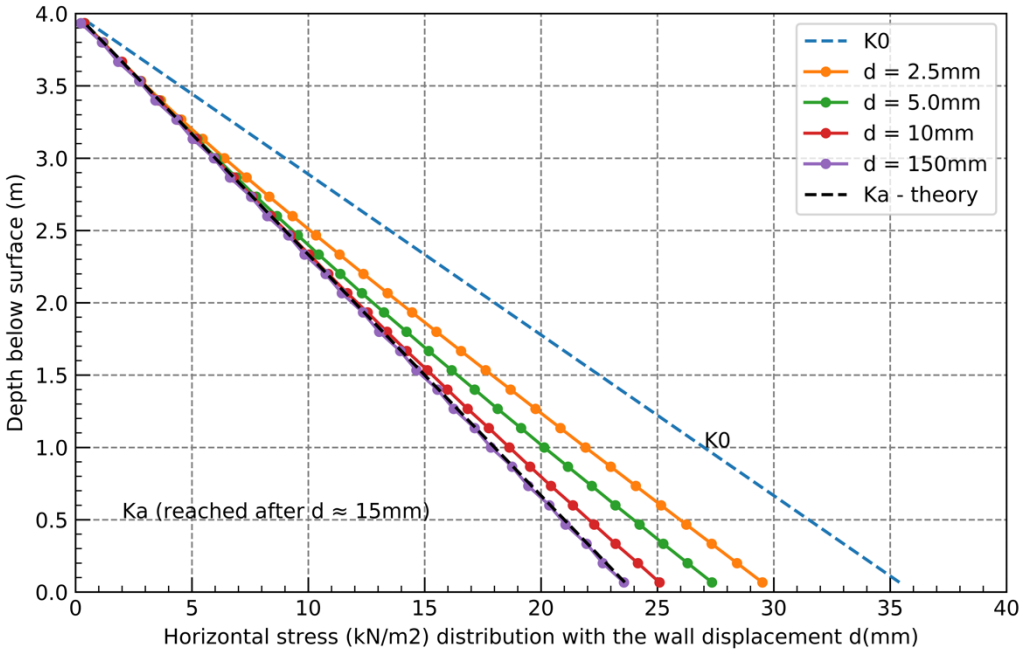

Figure 6-5: Earth pressure distribution for Drucker-Prager, active case

As can be seen in Figure 6-3, the simulation results matched well with analytical solution by Rankine active and passive earth pressure. This confirm the accuracy of our FEM code regarding the active and passive earth pressure analysis problem.

To have a deeper understanding of the simulation results, we can observe the distribution of earth pressure in the passive and active case in Figure 6-4 and Figure 6-5, respectively. It is seen that after a displacement of about 4cm, the passive earth pressure coefficients has reached at all of the elements. On the other hand, with only 1cm of displacement, al of elements has reached K_a.

In this calculation, explicit method is used, so, the convergence of simulation results can be confirmed via Figure 6-6 and Figure 6-7 for passive and active case, respectively. As expected, the higher the number of calculation steps is, the closer it is to the analytical solution.

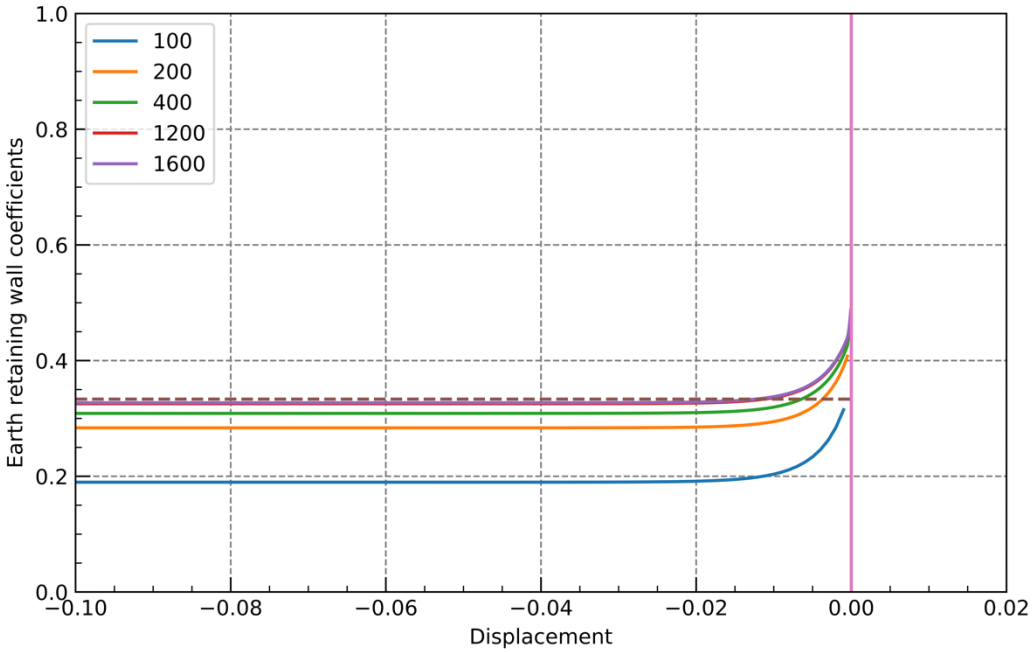

Figure 6-6 The convergence of earth pressure coefficient analysis for Drucker-Prager model, active case

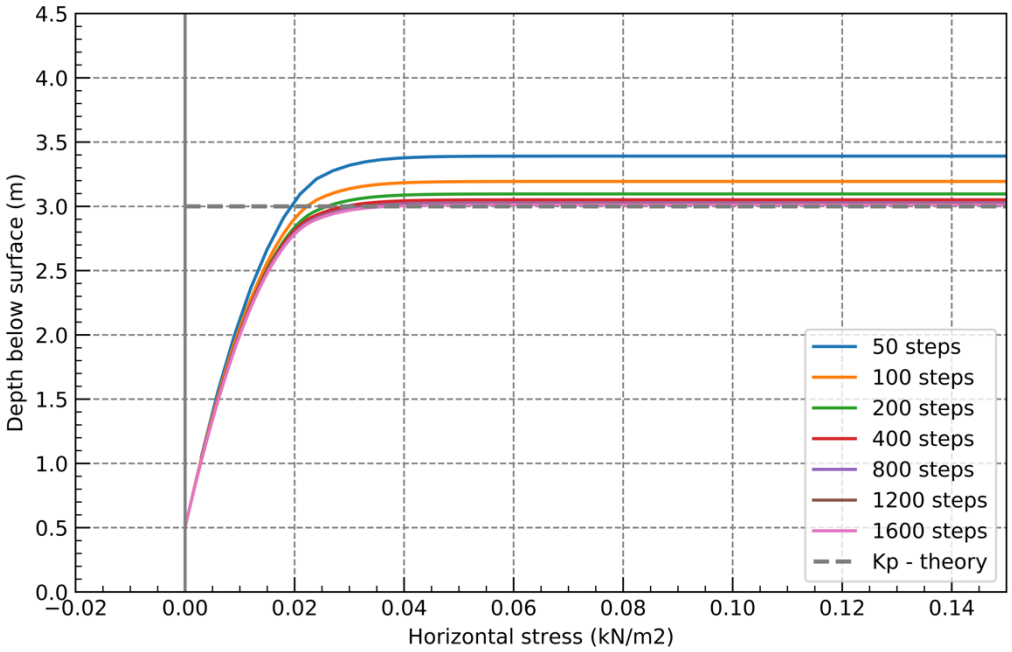

Figure 6-7: The convergence of earth pressure coefficient analysis for Drucker-Prager model, passive case

6.1.5 Conclusion

Our FEM code has been validated for the case of active and passive earth pressure analysis using Drucker-Prager criterial. The FEM simulation results matched well with the analytical results by Rankine. Thus, in the next section, we will use our developed FEM code for the analysis of active and passive earth pressure on crushable soil using our proposed model.

6.2 Analysis of active and passive eath pressure coefficients on crushable soils

6.2.1 Material parameters & initial condition of soils

Dogs Bay sand with the material parameter described in Table 6.2 is used in these analysis. The detail of initial soil state condition used in these simulations is also described in Table 6.2.

The active and passive earth pressure coefficient analysis are carried out by using our proposed model for soil considering particle crushing. FEM is used for solving nonlinear equations with boundary conditions. The analysis domain is discrete by Quad4 element. A finite element mesh of 833 elements is shown in Fig. The nodes representing the retaining wall are incrementally displaced by an equal amount in the horizontal direction, simulating a rigid wall condition with uniform horizontal displacement. Smooth retaining wall conditions are simulated by not restraining vertical movement of these nodes.

Table 6-2: Materials parameters for Dogs Bay sand and initial soil condition

Parameter	Description	Classification	Value
λ	Compression index	Modified Cam Clay	0.265
κ	Recompression index		0.0015
N	Specific volume on NCL at p = 98 kPa		1.8
M	Critical stress ratio		1.65
ν	Poisson ratio		0.2
a	Parameter controlling density effect	Subloading Concept	500
p_r	Parameter controlling crushing resistance	Particle Crushing	5000
M_x	Parameter controlling the shape of crushing surface		0.58
ξ	Volumetric distance between NCL of $I_G = 0$ and $I_G = 1$		0.55
p_{x0}	Crushing stress when $I_G = 0$: (kN/m^2)		98

* These material parameters of Dogs Bay Sand were calibrated from the validation of elementary tests. The unit weight (γ = 18 kN/m^3) is applied by k_0 distribution with $k_0 = 0.75$ ($e_0 = 2.5$, $I_{G0} = 0$) before applying the loading process.

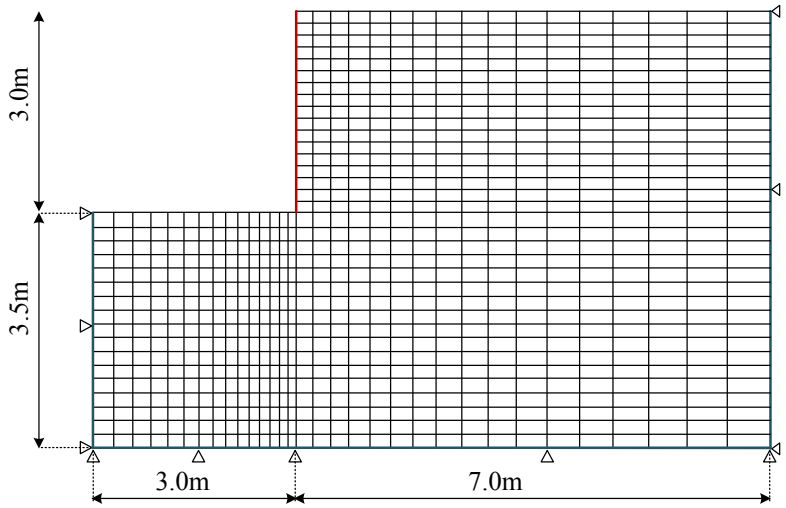

Figure 6-8: Analytical domain, boundary condition and grid mesh with 833 Quad4 elements

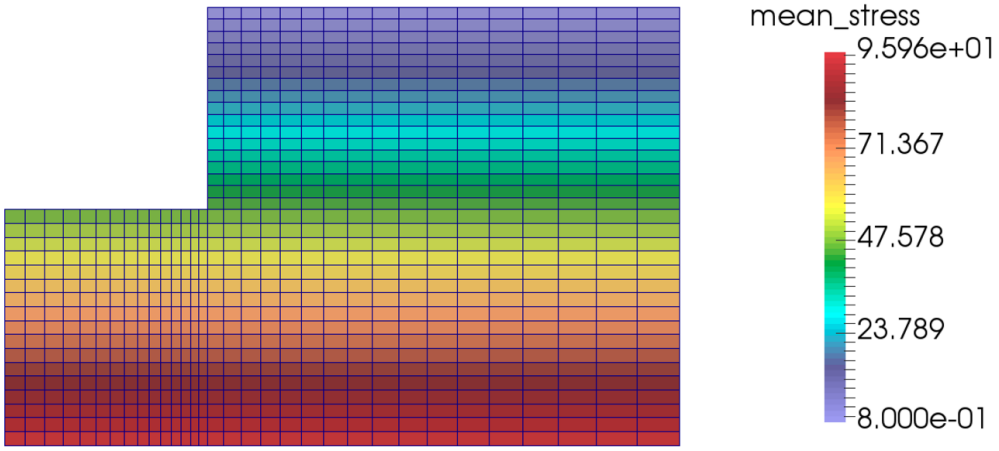

Figure 6-9: Distribution of mean stress before loading

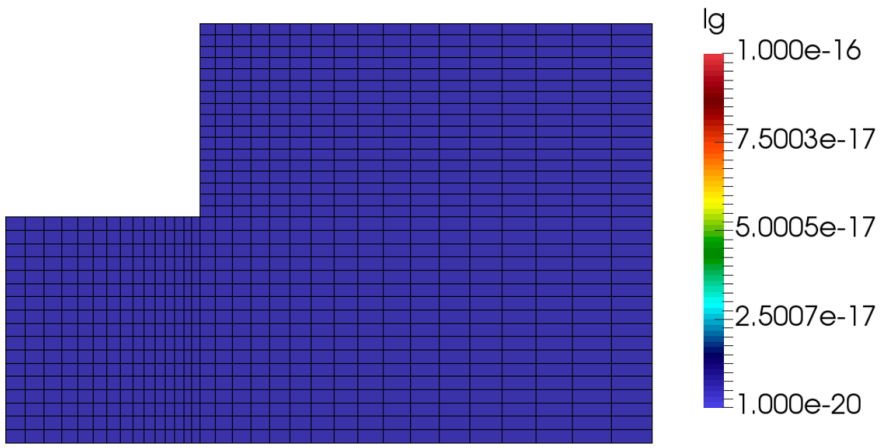

Figure 6-10: Distribution of grading index I_G before loading

6.2.2 Simulation results:

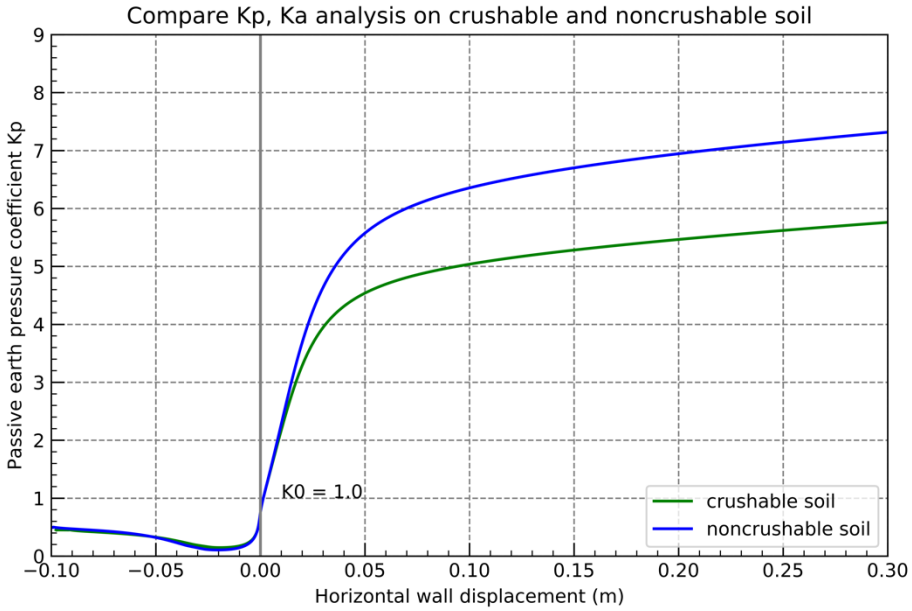

Figure 6-11: Passive and active earth pressure coefficients analyasis on crushable and noncrushable soil (3000 calculation steps)

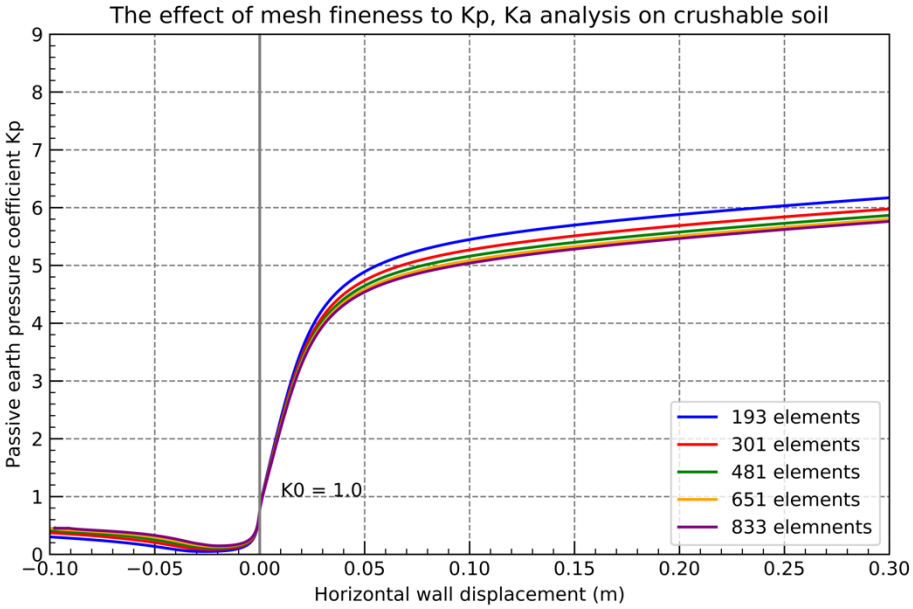

Figure 6-12: The effect of mesh fineness to K_p, K_a analysis on crushable soil

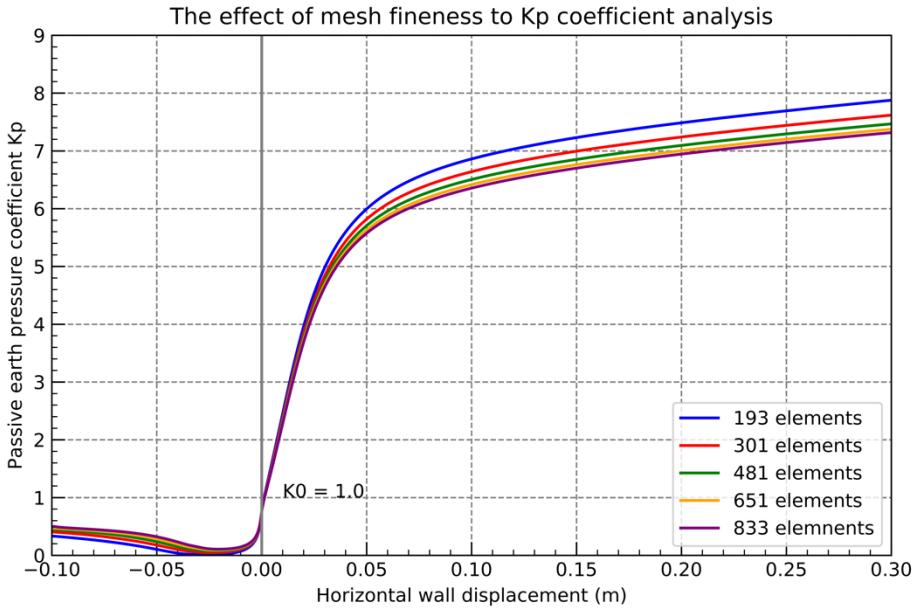

Figure 6-13: The effect of mesh fineness to K_p, K_a analysis on noncrushable soil

Figure 6-12 and Figure 6-13 shows the convergence of simulation results when the number of elements increased, we can observed the convergence of the results. Thus the simulation is stable. With the number of elements of 833, the results almost reached their ultimate convergence values.

6.2.3 Simulation results of K_p analysis

❖ **Crushable soil**

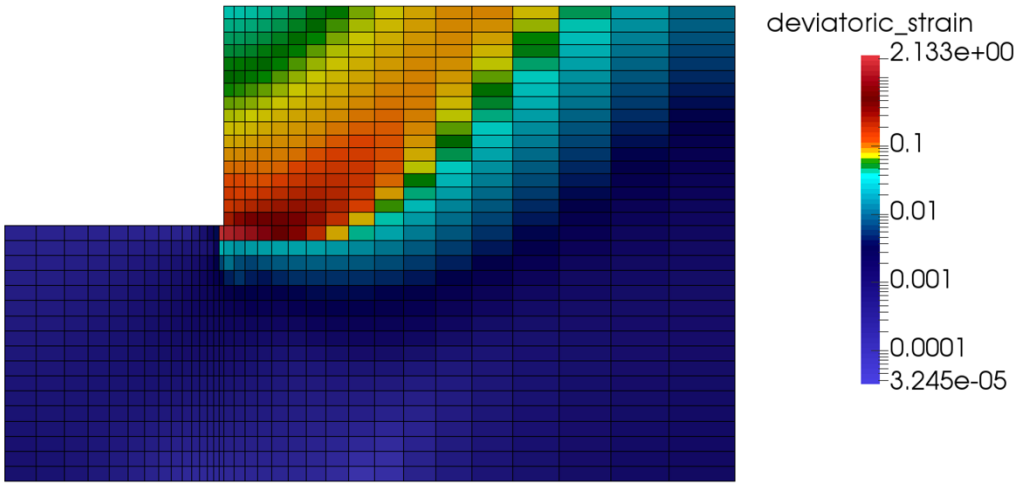

Figure 6-14: Deviatoric strain distribution of K_p analysis on crushable soil

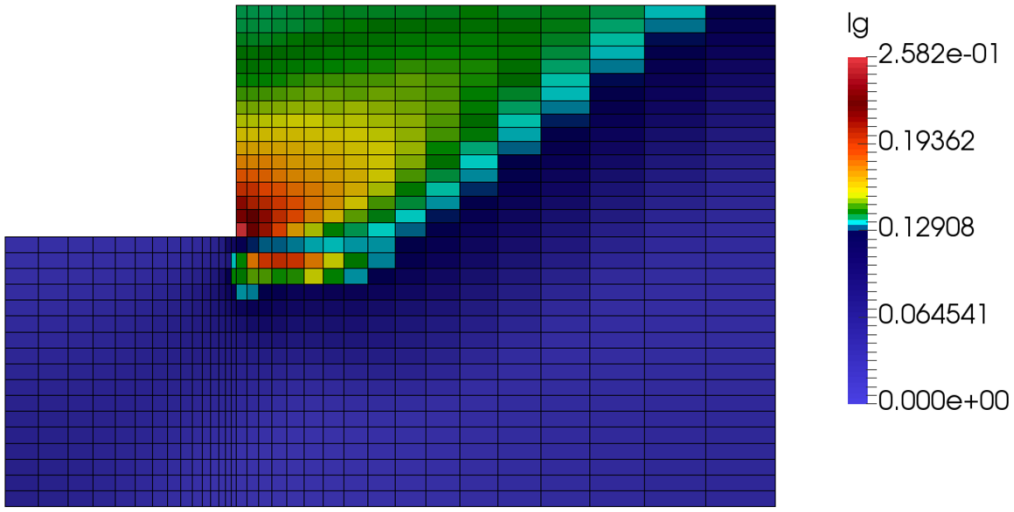

Figure 6-15: Grading index IG distribution of K_p analysis on noncrushable soil

The highest shear strain is observed at the bottom of the retaining wall due to strain localization. The ocurence of particle crushing is observed based on the distribution of I_G as in Figure 6-15, with the highest value of I_G at the bottom of the wall

❖ Noncrushable soil

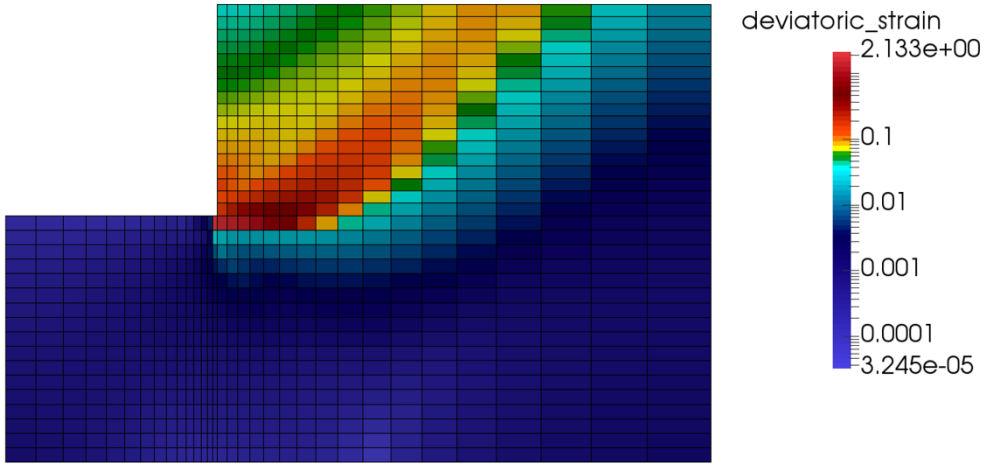

Figure 6-16: Deviatoric strain distribution of K_p analysis on noncrushable soil

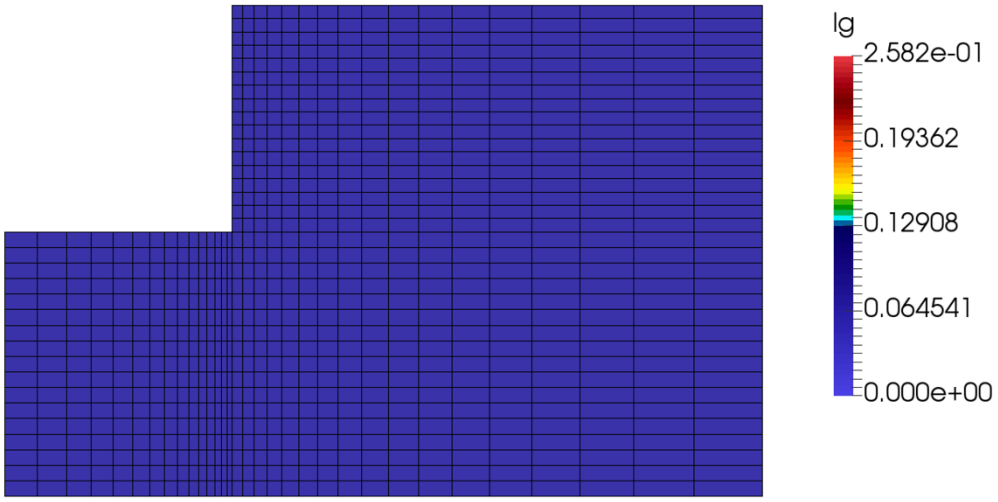

Figure 6-17: Grading index I_G distribution of K_p analysis on noncrushable soil

Particle crushing reduced soil strength, which leads to the reduction of K_p in comparison with K_p of uncrushable soil. Also, shear band in case of crushable soil (Figure 6-14)is smaller than that of noncrushable soil (Figure 6-16). This is likely due to the decrease of dilation when crushing occurs. The decrease of area in shear band can explain why K_p in crushable soil is smaller than that of noncrushale soil.

6.2.4 Simulation results of K_a analysis

❖ **Crushable soil**

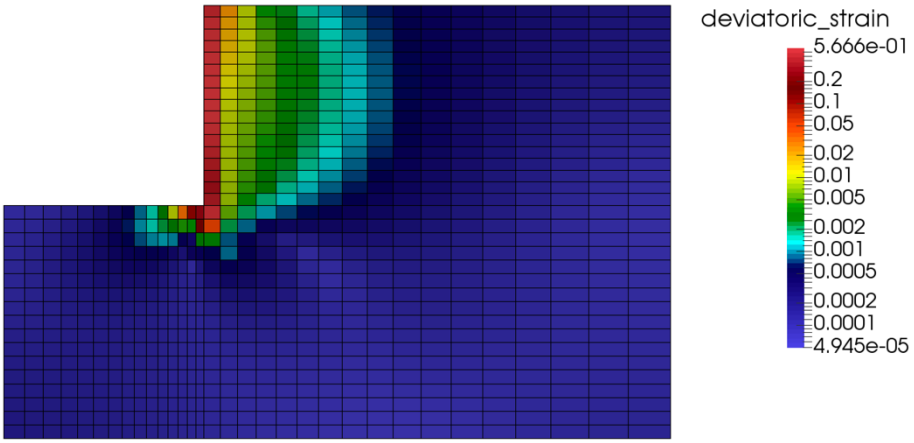

Figure 6-18: Deviatoric strain distribution of K_a analysis on crushable soil

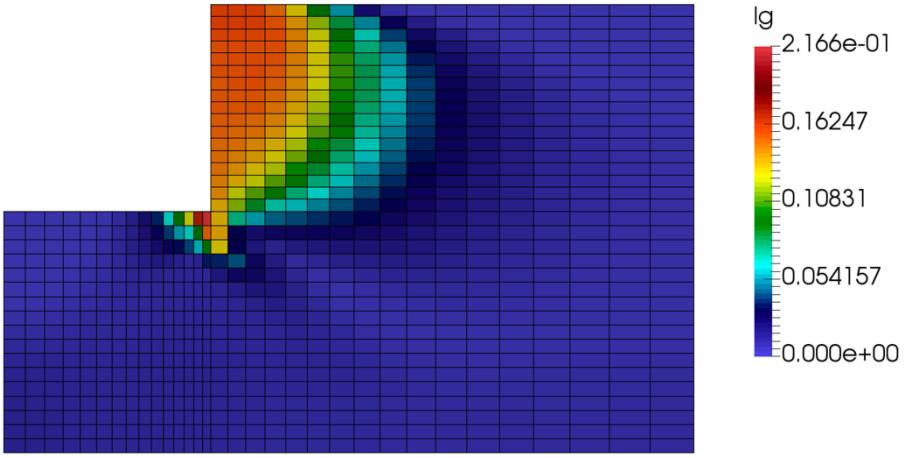

Figure 6-19: Grading index I_G distribution of K_a analysis on noncrushable soil

Figure 6-18 and Figure 6-19 show the distribution of deviatoric stress and grading index I_G in the analysis of K_a coefficient, respectively. As can be seen, the slip zone of passive earth pressure analysis (Figure 6-14) is much wider than that of active earth pressure analysis (Figure 6-18). This has been widely recognized in the literature, and this is confirmed in our simulation results.

❖ **Noncrushable soil**

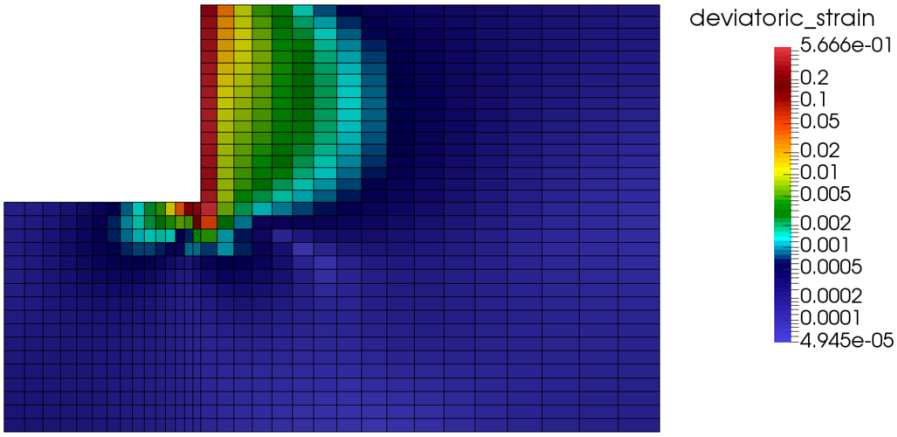

Figure 6-20: Deviatoric strain distribution of K_a analysis on noncrushable soil

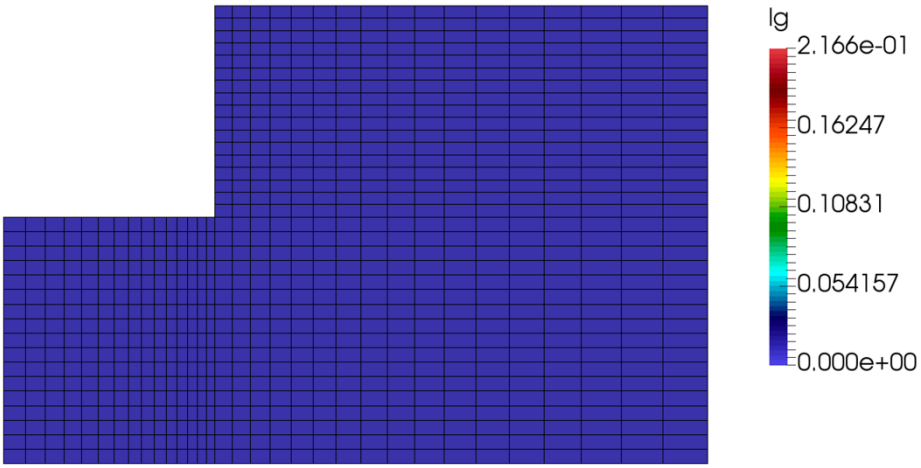

Figure 6-21: Grading index I_G distribution of K_a analaysis on noncrushable soil

6.3 Conclusion:

In the first part of this chapter, the validation of FEM code on the analysis of passive and active earth pressure coefficient was confirmed by comparing simulation results using Drucker-Prager model and Rankine solutions.

The second part of this chapter focused on the effect of particle crushing on the analysis of passive and active earth pressure coefficient. Based on the simulation results using Dog Bays sand,

passive earth pressure K_p significantly decreased together with the occurrence of particle crushing, from 7.8 to 5.8 when crushing occurs. On the other hand, K_a almost remains constant when crushing occurs. This suggests that it is necessary to consider particle crushing when design retaining wall on crushable soil because the stability of the wall may be put in danger when crushing is not properly considered.

Chapter 7 : Concluding remarks and future research

In this dissertation, a critical state constitutive model considering particle crushing was developed and validated. Also, the bearing capacity of strip footings on crushable soils was analyzed. In this final chapter, the principles findings and novelties of this research are summarized and prospect for future researches are discussed.

7.1 Contributions

The key findings and the novelty of the dissertation are summarized as follows:

Firstly, the mutual relationship between PSD curve and grading index was clarified. This can also help us further improve the accuracy in capturing soil behavior in elementary laboratory test by using soil constitutive model.

Secondly, a new soil constitutive model considering particle crushing was developed in critical state framework. The particle crushing phenomenon was implemented by using the evolution law of grading index I_G. An advantage of this model is that, not only compression and shearing effects, but also consolidation effect to particle crushing is also considered in this model. Also, the performance of the proposed model has been validated by a number of laboratory triaxial tests under isotropic consolidation, consolidated drained, and consolidated undrained condition.

Finally, one simple method to overcome the volumetric locking problem in FEM when using Quad4 elements has been validated with examples of elastic bending problems and strip footing bearing capacity analysis using VonMises model. As a first application of the proposed model for particle crushing, I performed the analysis of the bearing capacity of strip footing on Dog Bay sand. It was found that (1) with 15 cm settlement, bearing capacity of strip footing slightly reduced around 10% due to particle crushing in case of Dogs Bay sand, (2) under a specific allowable settlement, the effect of crushing on bearing capacity decreased when the footing size increases. (3) scale effect was also observed in our simulation; however, the ultimate bearing capacity was not observed in the simulation of Dogs Bay sand. (4) when assuming the bearing capacity under a certain settlement is “ultimate”, one interesting finding was that (the bearing capacity factor N_γ – strip footing width B) line of crushable soil in (log_{10}-log_{10}) scale was a straight line which shifted downwards from the (N_γ-B) line of uncrushable soil.

Another application of the proposed model was the analysis of passive and active earth pressure coefficient on crushable soils. It was found that the occurrence of particle crushing phenomenon reduced the passive earth pressure coefficient from 7.4 to 5.8 (corresponding to 0.3m displacement of the wall).

On the other hand, active earth pressure coefficient Ka is not significantly effected by particle crushing phenomenon

7.2 Future research

In this dissertation, the constitutive model considering particle crushing was developed based on the implementation of the changing of particle crushing curve. For future research activities, the particle shape effect on particle crushing is an interesting topic that can be further implemented. Also, the time effect of crushing is also an interesting topic to be observed in the long-term settlement of geotechnical structures. The third application is the modeling of the behavior of very coarse granular materials (diameter up to ~30cm), by considering the size effect of particle, which is similar to the research by Yin et al, (2016). Thus, I expect to obtain information about the effect of particle shape to crushing and the time effect to particle crushing in practical or experimental tests.

In the near future, I would like to analysis the effect of the height of the wall to the analysis of passive and active earth pressure coefficient. This maybe similar to the scale effect in strip footing bearing capacity. Furthermore, the effect of the mode of wall movement on K_a and K_p of retaining wall on crushable soil is also an interesting topic when considering. Regarding the speed of calculation in numerical method, instead of explicit method in FEM, an implicit method will both reduce accumulated errors as well as save computation time

REFERENCES

Alba, J. and J. Audibert (1999). Pile design in calcareous and carbonaceous granular materials, and historic review. Proceedings of the 2nd International Conference on Engineering for Calcareous Sediments. Rotterdam: AA Balkema.

Andreasen, A. M. and J. Andersen (1930). "Relation between grain size and interstitial space in products of unconsolidated granules." Kolloid-Zeitschrift **50**(3): 217-228.

Bandini, V. and M. R. COOP (2011). "The influence of particle breakage on the location of the critical state line of sands." Soils and Foundations **51**(4): 591-600.

Been, K. and M. G. Jefferies (1985). "A state parameter for sands." Géotechnique **35**(2): 99-112.

Belytschko, T. and L. Bindeman (1991). "Assumed strain stabilization of the 4-node quadrilateral with 1-point quadrature for nonlinear problems." Computer Methods in Applied Mechanics and Engineering **88**(3): 311-340.

Chandler, H. (1985). "A plasticity theory without Drucker's postulate, suitable for granular materials." Journal of the Mechanics and Physics of Solids **33**(3): 215-226.

Cheng, Y., et al. (2005). "Grain crushing and critical states observed in DEM simulations." P&G05 **2**: 1393-1397.

Clark, J. I. (1998). "The settlement and bearing capacity of very large foundations on strong soils: 1996 RM Hardy keynote address." Canadian Geotechnical Journal **35**(1): 131-145.

Commend, S., et al. (2004). "Stabilized finite elements applied to elastoplasticity: I. Mixed displacement–pressure formulation." Computer Methods in Applied Mechanics and Engineering **193**(33-35): 3559-3586.

Coop, M. (1990). "The mechanics of uncemented carbonate sands." Géotechnique **40**(4): 607-626.

Coop, M. and I. Lee (1993). "The behaviour of granular soils at elevated stresses." Predictive soil mechanics: 186-198.

Coop, M., et al. (2004). "Particle breakage during shearing of a carbonate sand." Géotechnique **54**(3): 157-164.

Daouadji, A., et al. (2001). "An elastoplastic model for granular materials taking into account grain breakage." European Journal of Mechanics-A/Solids **20**(1): 113-137.

Datta, M., et al. (1980). An appraisal of the existing practice of determining the axial load capacity of deep penetration piles in calcareous sands. Offshore Technology Conference, Offshore Technology Conference.

De Beer, E. (1965). Bearing capacity and settlement of shallow foundations on sand. Proc. of Symp. Bearing Capacity and Settlement of Foundation.

Dinger, D. and J. Funk (1994). Predictive process control of crowded particulate suspensions, USA, Kluwer academic publishers.

Einav, I. (2007a). "Breakage mechanics—Part I: Theory." Journal of the Mechanics and Physics of Solids **55**(6): 1274-1297.

Flanagan, D. and T. Belytschko (1981). "A uniform strain hexahedron and quadrilateral with orthogonal hourglass control." International journal for numerical methods in engineering **17**(5): 679-706.

Gajo, A. and D. Muir Wood (1999). "A kinematic hardening constitutive model for sands: the multiaxial formulation." International Journal for Numerical and Analytical Methods in Geomechanics **23**(9): 925-965.

Ghafghazi, M., et al. (2014). "Particle breakage and the critical state of sand." Soils and Foundations **54**(3): 451-461.

Golightly, C. and A. Hyde (1988). "Some fundamental properties of carbonate sands." Engineering for calcareous sediments **1**: 69-78.

Hardin, B. O. (1985). "Crushing of soil particles." Journal of geotechnical engineering **111**(10): 1177-1192.

Hashiguchi, K. and M. Ueno (1977). "Elastoplastic constitutive laws of granular materials." Constitutive Equations of Soils (Proc. 9th ICFSME, Spec. Session 9): 73-82.

Hattamleh, O. H. A., et al. (2013). "The Consequence of Particle Crushing in Engineering Properties of Granular Materials." International Journal of Geosciences **04**(07): 1055-1060.

Hughes, T. J. (1980). "Generalization of selective integration procedures to anisotropic and nonlinear media." International journal for numerical methods in engineering **15**(9): 1413-1418.

Hughes, T. J. (2012). The finite element method: linear static and dynamic finite element analysis, Courier Corporation.

Hughes, T. J., et al. (1978). "Reduced and selective integration techniques in the finite element analysis of plates." Nuclear Engineering and Design **46**(1): 203-222.

Jaky, J. (1944). "Soil mechanics (in Hugarian)."

Kikumoto, M., et al. (2010). "Particle crushing and deformation behaviour." Soils and Foundations **50**(4): 547-563.

Kutter, B. L., et al. (1988). "Strength parameters for bearing capacity of sand." Journal of geotechnical engineering **114**(4): 491-498.

Kuwajima, K., et al. (2009). "Pile bearing capacity factors and soil crushabiity." Journal of geotechnical and geoenvironmental engineering **135**(7): 901-913.

Lade, P. V., et al. (1996). "Significance of particle crushing in granular materials." Journal of geotechnical engineering **122**(4): 309-316.

Lee, K. L. and I. Farhoomand (1967). "Compressibility and crushing of granular soil in anisotropic triaxial compression." Canadian Geotechnical Journal **4**(1): 68-86.

Lees, A., et al. (2013). "Palm Jumeirah, Dubai: cone penetrometer testing data from the carbonate sand fill." Proceedings of the Institution of Civil Engineers-Geotechnical Engineering **166**(3): 253-267.

Luzzani, L. and C. MR (2002). "On the relationship between particle breakage and the critical state of sands." Soils and Foundations **42**(2): 71-82.

Marsal, R. J. (1967). "Large-scale testing of rockfill materials." Journal of the Soil Mechanics and Foundations Division **93**(2): 27-43.

McDowell, G. and M. Bolton (2000). "Effect of particle size distribution on pile tip resistance in calcareous sand in the geotechnical centrifuge." Granular Matter **2**(4): 179-187.

Miura, S., et al. (2003). "Deformation-strength evaluation of crushable volcanic soils by laboratory and in-situ testing." Soils and Foundations **43**(4): 47-57.

Muir Wood, D. (1990). Soil behaviour and critical state soil mechanics, Cambridge university press.

Muir Wood, D. (2007). "The magic of sands— The 20th Bjerrum Lecture presented in Oslo, 25 November 2005." Canadian Geotechnical Journal **44**(11): 1329-1350.

Muir Wood, D. and K. Maeda (2007). "Changing grading of soil: effect on critical states." Acta Geotechnica **3**(1): 3-14.

Poulos, H. G. and E. W. Chua (1985). Bearing capacity of foundations on calcareous sand. International Conference on Soil Mechanics and Foundation Engineering, 11th, 1985, San Francisco, USA (Volume 3).

Prandtl, L. (1920). "Über die härte plastischer körper." Narchr K. Ges. Wiss. Gött., Math.-Phys **K1**: 74–85.

Roscoe, K., et al. (1963). "Yielding of clays in states wetter than critical." Géotechnique **13**(3): 211-240.

Sasitharan, S., et al. (1994). "State-boundary surface for very loose sand and its practical implications." Canadian Geotechnical Journal 31(3): 321-334.

Senders, M., et al. (2013). "Piled foundations on the North West shelf." Australian Geomechanics (this issue).

Shiraishi, S. (1990). "Variation in bearing capacity factors of dense sand assessed by model loading tests." Soils and Foundations **30**(1): 17-26.

Tatsuoka, F. (1991). Progressive failure and particle size effect in bearing capacity of a footing on sand. Proc. of Geotech. Eng. Congress, Special Publication, ASCE.

Tatsuoka, F. (1994). "Link among design, model tests, theories and sand properties in bearing capacity of footing on sand." Proceeding of the 13th International Conference on Soil Mechanics and Foundation Engineering **5**: 57-88.

Terzaghi, K. (1944). Theoretical soil mechanics, Chapman And Hali, Limited John Wiler And Sons, Inc; New York.

Timoshenko, S. P. (1936). Theory of Elastic Stability, by S. Timoshenko, McGraw-Hill Book Company, Incorporated.

Tojo, A., et al. (2009). "Experimental study on the influence of particle crushing on the critical states of sandy soils." Proceeding Annual Conference of Japanese Society for Civil Engineers Seibu Branch **CD_ROM (in Japanese)**.

Tyler, S. W., and Stephen W. W. (1992). "Fractal scaling of soil particle-size distributions: analysis and limitations." Soil Science Society of America Journal **56.2**: 362-369.

Ueno, K. (1994). Initial conditions and their influences on bearing characteristics of sand. Proc. Int. Conf. Centrifuge 94.

Wood, D. M. and K. Maeda (2008). "Changing grading of soil: effect on critical states." Acta Geotechnica **3**(1): 3.

Yang, J. and X. Luo (2018) "The critical state friction angle of granular materials: does it depend on grading?" Acta Geotechnica: 1-13.

Yamada, S. and K. Sato (2007). Effects of Density and Confining Pressure on Mechanical Behavior of Crushable Soil. The Seventeenth International Offshore and Polar Engineering Conference, International Society of Offshore and Polar Engineers.

Yao, Y.-P., et al. (2008). "Constitutive model considering sand crushing." Soils and Foundations **48**(4): 603-608.

Yasufuku, N. and A. Hyde (1995). "Pile end-bearing capacity in crushable sands." Géotechnique **45**(4): 663-676.

Yin, Z.-Y., et al. (2016). "Modeling mechanical behavior of very coarse granular materials." Journal of engineering mechanics **143**(1): C4016006.

Zhang, C., et al. (2013). "The end-bearing capacity of piles penetrating into crushable soils." Géotechnique **63**(5): 341.

Zienkiewicz, O., et al. (1971). "Reduced integration technique in general analysis of plates and shells." International journal for numerical methods in engineering **3**(2): 275-290.

Zlatović, S and K Ishihara (1995) "On the influence of nonplastic fines on residual strength " Proceedings of the IS-Tokyo **9**

APPENDIX

A. Verification of FEM with modified B-bar method approach in 2D plane strain condition

A1. Elastic beam bending problem

As an example to illustrate the performance of modified B-bar method to incompressible material, the behavior of a cantilever shown in Figure A- 1 has been studied. The bending of an incompressible elastic beam is a typical problem in which significant volumetric locking is exhibited (Flanagan and Belytschko (1981) Belytschko and Bindeman (1991)). The boundary condition of cantilever problem is analyzed as in Figure A-A . The cantilever is of dimension H = 60 mm, L = 480 mm, and the applied end load is equivalent to a uniform stress of 1 unit per unit area (P = 6000 kPa). The material properties used are Young modulus $E = 3\times10^7$ kPa, and Poisson ratio $\nu = 0.499$ (nearly incompressible). The 4-node isoparametric element is used in this simulation. Different mesh densities are conducted. The Cartesian coordinates (x, y) are set along the parallel and normal directions to the beam axis, respectively.

The theoretical solution Timoshenko (1936) of the vertical deflection is expressed as:

$$u_y = \frac{P}{6\bar{E}I}\left\{3\bar{\nu}y^2(L-x)+\frac{1}{4}(4+5\bar{\nu})H^2x+(3L-x)x^2\right\} \tag{0-1}$$

in which:

$$I=\frac{1}{12}H^3,\quad \bar{E}=\frac{E}{1-\nu^2},\quad \bar{\nu}=\frac{\nu}{1-\nu} \tag{0-2}$$

Here, the deflection is positive in the y direction, and I is the second moment of area when the unit depth is assumed.

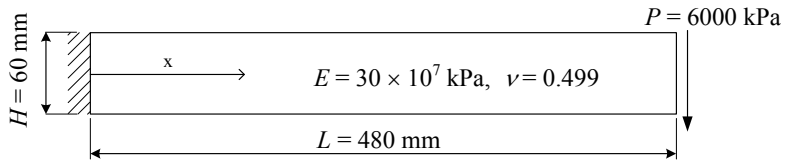

Figure A- 1 Coordinate system for the cantilever beam.

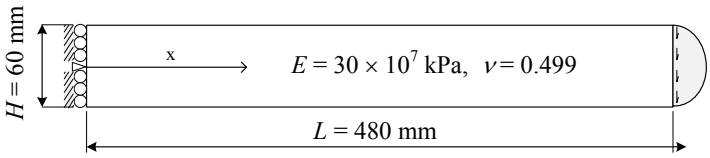

Figure A- 2. Cantilever problem analyzed.

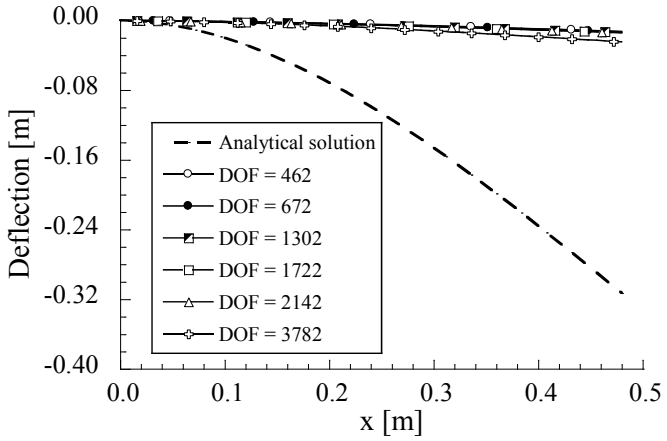

Figure A- 3: Distribution of deflection (traditional FEM)

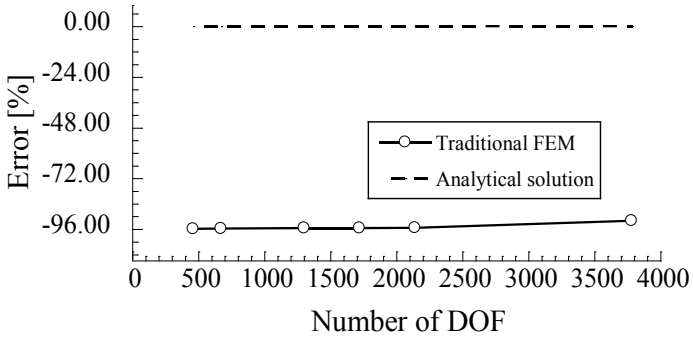

Figure A- 4: Error in tip deflection (traditional FEM)

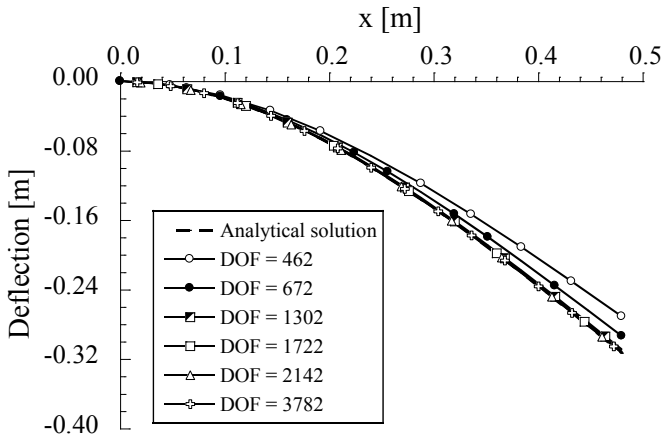

Figure A- 5: Distribution of deflection (FEM with modified B-bar).

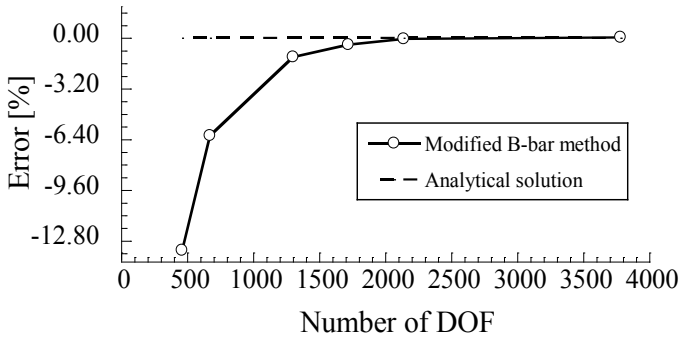

Figure A-6: Error in tip deflection (FEM with modified B-bar method)

It is clearly seen (Figure *A-3* to Figure A-6) that without modified B-bar approach, the beam's displacement is far different from analytical solution. On the other hand, B-bar method has a really good effect on the behavior of nearly incompressible bar as long as the number of DOF is large enough. For a fine mesh of DOF = 3782, the simulation result agrees well with the theoretical solution. Therefore, the results demonstrate that the B-bar approach improved the performance of FEM when dealing with incompressible material or critical state model. Thus this B-bar method will be applied in the analysis of bearing capacity of strip footing.

A2. Finite element analysis of the ultimate bearing capacity of strip footing using von Mises model

A2.1 von Mises yielding criteria

Yield surface

In von Mises model, hydrostatic stress is assumed to have no contribution to plasticity but only deviatoric stress does. Equivalent von Mises stress is defined as:

$$\sigma_{eq} = \sqrt{3J_2} = \sqrt{\frac{3}{2} s_{ij} s_{ij}} \tag{0-3}$$

in which $s_{ij} = \sigma_{ij} - \frac{1}{3}\sigma_{kk}\delta_{ij}$

Assuming that under loading, the material is yielding when $\sigma_{eq} > Y$, yield surface in Figure A-7 is defined as:

$$f(\sigma_{ij}) = \sqrt{3J_2} - Y \tag{0-4}$$

or in terms of the so-called equivalent stress

$$f(\boldsymbol{\sigma}) = \sigma_{eq} - \sigma_y \tag{A-2}$$

$$\sigma_{eq} = \left[\frac{1}{2}(\sigma_1 - \sigma_2)^2 + \frac{1}{2}(\sigma_2 - \sigma_3)^2 + \frac{1}{2}(\sigma_3 - \sigma_1)^2\right]^{\frac{1}{2}}$$

$$= \left[\frac{1}{2}(\sigma_x - \sigma_y)^2 + \frac{1}{2}(\sigma_y - \sigma_z)^2 + \frac{1}{2}(\sigma_z - \sigma_x)^2 + 3\tau_{xy}^2 + 3\tau_{yz}^2 + 3\tau_{zx}^2\right]^{\frac{1}{2}}$$

where 1, 2, 3 are the principle stress directions.

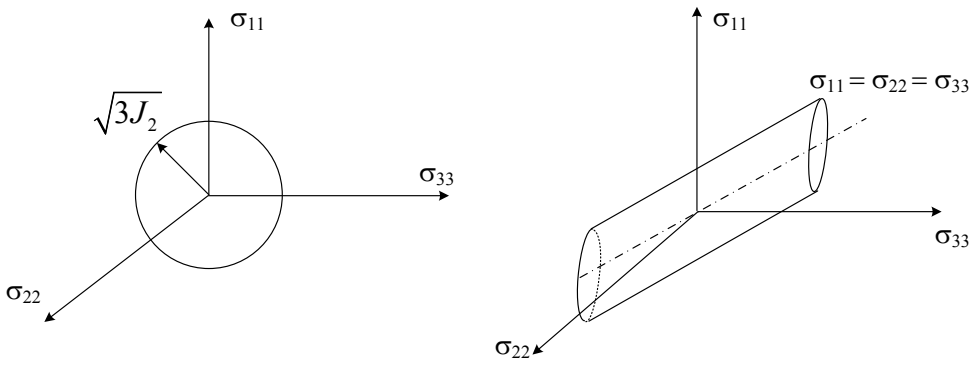

Figure A- 6: Visualization of von Mises yield surface in principle stress state

A2.2 von Mises yield criteria in 2D plane strain problem

In plane strain problems, we have the following conditions:

$$\varepsilon_3 = \gamma_{23} = \gamma_{13} = 0 \tag{A-3}$$

If this is to be valid for all strains, it must hold that:

$$d\varepsilon_3^e = \gamma_{23}^e = \gamma_{13}^e = 0 \tag{A-4}$$

and

$$d\varepsilon_3^p = \gamma_{23}^p = \gamma_{13}^p = 0 \tag{A-5}$$

Meanwhile, when assumed associated flow rule:

$$d\boldsymbol{\varepsilon}^p = \langle d\Lambda \rangle \frac{\partial f}{\partial \boldsymbol{\sigma}'} \tag{A-6}$$

We can derive

$$d\varepsilon_3^p = \langle d\Lambda \rangle \frac{\partial f}{\partial \sigma_e} \left(2\sigma_3 - \sigma_1 - \sigma_2\right) \tag{A-7}$$

When assumed perfect plasticity at failure mode, the increment of plastic strain would be same as the increment of total strain: $d\varepsilon_3^p = d\varepsilon_3$. Then, the expression of $d\varepsilon_3^p$ gives the condition for the normal stresses as:

$$\sigma_3 = \frac{1}{2}\left(\sigma_1 + \sigma_2\right) \tag{A-8}$$

Yield function becomes

$$f(\boldsymbol{\sigma}) = \frac{\sqrt{3}}{2}\left(\sigma_1 - \sigma_2\right) - \sigma_y \tag{A-9}$$

In which $\sigma_1 - \sigma_2 = 2c$, c is soil cohesion. Thus, the condition $f(\boldsymbol{\sigma}) = 0$ will lead to $\sigma_y = c\sqrt{3}$

Finally, yield function of von Mises model in 2D plane strain is written as:

$$f(\boldsymbol{\sigma}) = \sigma_{eq} - c\sqrt{3} \tag{A-10}$$

A2.3 Derivation of elastoplastic stiffness matrix of von Mises model

Elastic stiffness matrix

$$\begin{bmatrix}\sigma_{11}\\ \sigma_{22}\\ \sigma_{33}\\ \sigma_{12}\\ \sigma_{13}\\ \sigma_{23}\end{bmatrix} = \frac{1}{(1+v)(1-2v)}\begin{bmatrix}E(1-v) & Ev & Ev & 0 & 0 & 0\\ Ev & E(1-v) & Ev & 0 & 0 & 0\\ Ev & Ev & E(1-v) & 0 & 0 & 0\\ 0 & 0 & 0 & 1/G & 0 & 0\\ 0 & 0 & 0 & 0 & 1/G & 0\\ 0 & 0 & 0 & 0 & 1/G & 0\end{bmatrix}\begin{bmatrix}\varepsilon_{11}\\ \varepsilon_{22}\\ \varepsilon_{33}\\ \varepsilon_{12}\\ \varepsilon_{13}\\ \varepsilon_{23}\end{bmatrix} \tag{A-11}$$

Assume small strain behavior

$$\boldsymbol{d\varepsilon} = \boldsymbol{d\varepsilon^e} + \boldsymbol{d\varepsilon^p} \tag{A-12}$$

Flow rule:

Associated flow rule is assumed

$$d\boldsymbol{\varepsilon}^p = \left\langle \dot{\Lambda} \right\rangle \frac{\partial f}{\partial \boldsymbol{\sigma}} \tag{A-13}$$

Increment of stress

$$d\boldsymbol{\sigma} = \boldsymbol{D^e} : d\boldsymbol{\varepsilon^e} = \boldsymbol{D^e} : (d\boldsymbol{\varepsilon} - d\boldsymbol{\varepsilon^p}) \tag{A-14}$$

Consistency condition:

$$df = 0 \Leftrightarrow \frac{\partial f}{\partial \boldsymbol{\sigma}} : d\boldsymbol{\sigma} = 0 \tag{A-15}$$

Substituting (A-13) and (A-14) into (A-15), we derive

$$\left\langle \dot{\Lambda} \right\rangle = \left\langle \frac{\frac{\partial f}{\partial \boldsymbol{\sigma}} : \boldsymbol{D}^e : d\boldsymbol{\varepsilon}}{\frac{\partial f}{\partial \boldsymbol{\sigma}} : \boldsymbol{D}^e : \frac{\partial f}{\partial \boldsymbol{\sigma}}} \right\rangle \tag{A-16}$$

Elastoplastic stiffness matrix

Substituting (A-13) and (A-16) into (A-14):

$$\dot{\boldsymbol{\sigma}} = \left[\boldsymbol{D}^e - \left\langle \frac{\boldsymbol{D}^e : \frac{\partial f}{\partial \boldsymbol{\sigma}} : \frac{\partial f}{\partial \boldsymbol{\sigma}} : \boldsymbol{D}^e}{\frac{\partial f}{\partial \boldsymbol{\sigma}} : \boldsymbol{D}^e : \frac{\partial f}{\partial \boldsymbol{\sigma}}} \right\rangle \right] : \dot{\boldsymbol{\varepsilon}} \tag{A-17}$$

When the rate of the plastic multiplier $\dot{\Lambda} = 0$, the soil's behavior is purely elastic with the elastic stiffness. On the contrary, when the rate of the plastic multiplier the soil exhibits deformation under elastoplastic deformation with the elastoplastic stiffness:

$$\boldsymbol{D}^{ep} = \boldsymbol{D}^{e} - \frac{\boldsymbol{D}^{e} : \frac{\partial f}{\partial \boldsymbol{\sigma}} : \frac{\partial f}{\partial \boldsymbol{\sigma}} : \boldsymbol{D}^{e}}{\frac{\partial f}{\partial \boldsymbol{\sigma}} : \boldsymbol{D}^{e} : \frac{\partial f}{\partial \boldsymbol{\sigma}}} \tag{A-18}$$

A2.4 Validation of the implementation of von Mises model into FEM

Before moving to the bearing capacity analysis under 2D plane strain condition using von Mises yielding criteria, in this section, the simulation of oedometer test under both elementary level test and FEM simulation is conducted with the material described in Table A.1

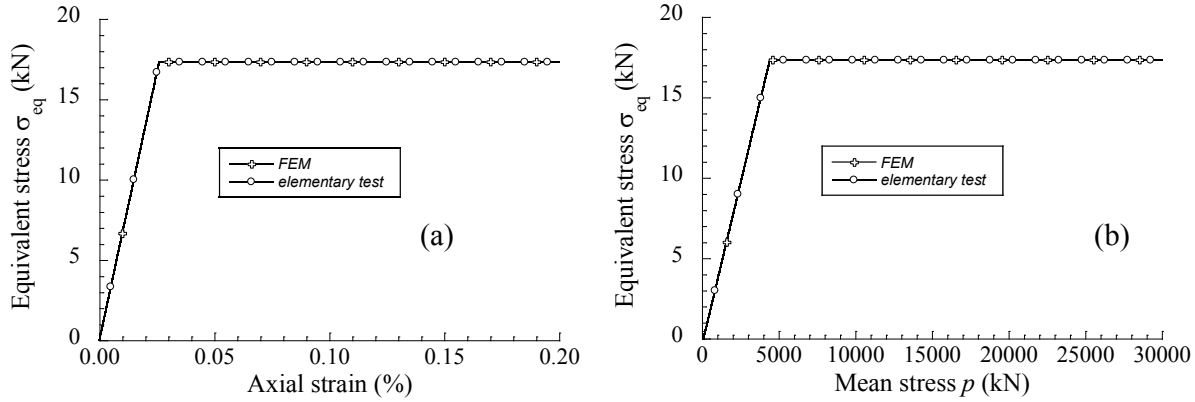

Figure A- 7: Comparison of FEM and elementary test under oedometer test condition

Table A- 1: Materials parameters for von Mises model

Parameter	Discription	Value
E	Young modulus (kPa)	100000
ν	Poisson's ratio	0.499

By observing the exact simulation result between elementary test simulation and our FEM simulation in 2D plane strain (Figure A- 7), we can confirm that the von Mises model has been successfully implemented into our FEM code.

A2.5 Verification of modified B-bar method to the ultimate bearing capacity of strip footing using von Mises model

In this section, the performance of FEM with modified B-bar method applied to elastoplastic analyses of soils is examined through the bearing capacity analysis of the vertically loaded strip footing on cohesive soil using Von-Mises model. This problem usually suffers from volumetric locking because the volumetric strain of soil during failure is governed by plastic flow regardless of the setting of the elastic parameters as Poisson's ratio. Figure A- 8 shows the analytic domain, boundary condition and mesh grid of the current problem. The analytical domain is set to be sufficiently large so that the boundary conditions do not affect the simulation results. The lateral side of the ground is fixed in the horizontal direction, and the bottom of the ground is fixed in all directions. Meshes with different fineness, with the finer meshes elements near the footing position are considered. Explicit method with sufficient large number of calculation steps (6000) to reach to convergence solution has been performed.

The ground is modeled as elasto-perfectly plastic material using von Mises's failure criterion, assuming associated flow rule. It should be noted that the weight of the material are ignored to compare the simulation result with theoretical solution (Prandtl (1920)) of the bearing capacity of a strip footing on a weightless cohesive ground.

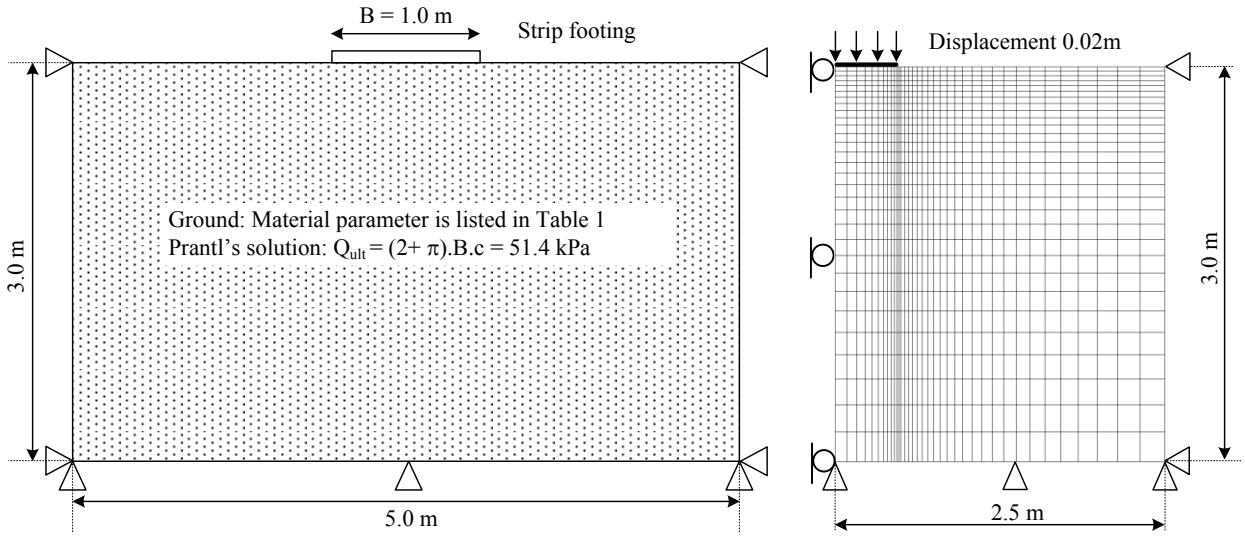

Figure A- 8: Analytical domain, boundary condition, and mesh (1080 elements) of strip footing & material parameters

A-2: Material parameters for von Mises model

Parameter	Discription	Value
E	Young modulus (kPa)	100000
ν	Poisson's ratio	0.499
c	Cohesion (kPa)	10

* The weight of the material is ignored to compare the simulation results with Prandtl's theoretical solution

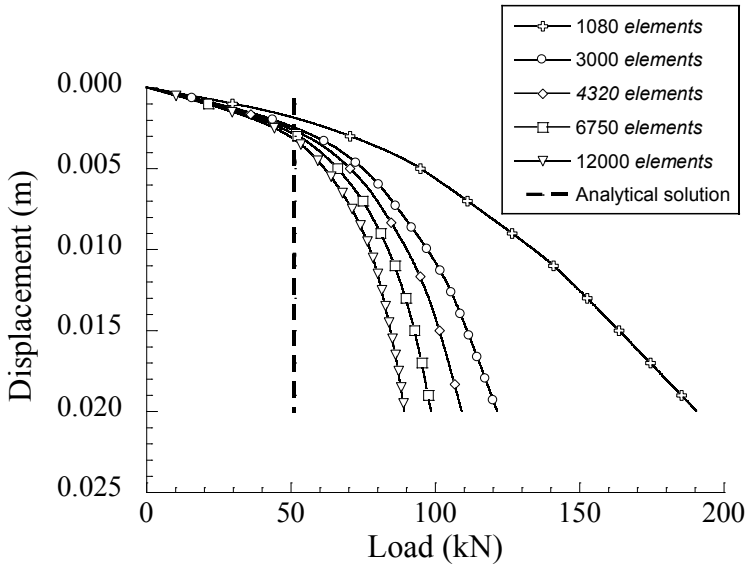

Figure A- 9: Bearing capacity of strip foundation using von Mises model by traditional FEM with 6000 calculation steps

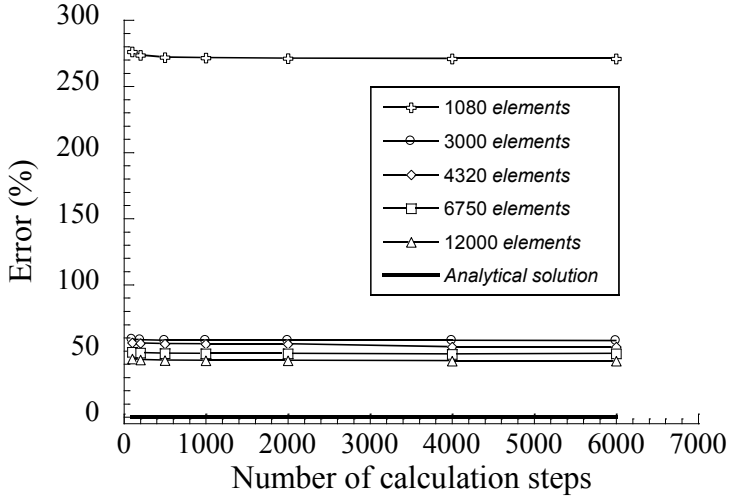

Figure A- 10: Error of bearing capacity when compared with Prandtl's solution by von Mises model & traditional FEM

The computed relationships between the footing displacement and the applied force with respect to the traditional FEM and FEM with modified B-bar approach are shown in Figure A- 9 and Figure A- 11. In these the figures, Prandtl's solution is indicated by the straight line.

$$Q = (2 + \pi).c.B \tag{0-5}$$

in which, c is the cohesion of the soil, B is the footing width. Thus, Q ≈ 51 4 kN in the current problem, where c = 10.0 kPa, and B = 1.0 m. When using the B-bar method, the vertical load converged to an almost constant value, and the ultimate load could be easily determined.

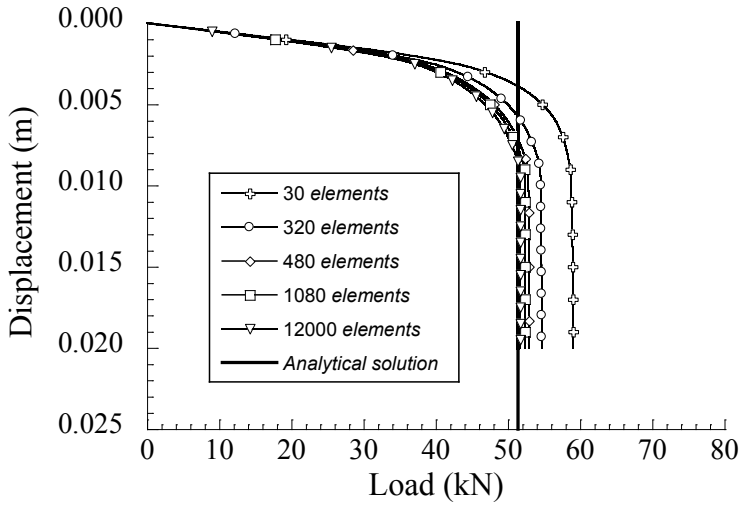

Figure A- 11: Bearing capacity of strip foundation using von Mises model by FEM with modified B-bar method

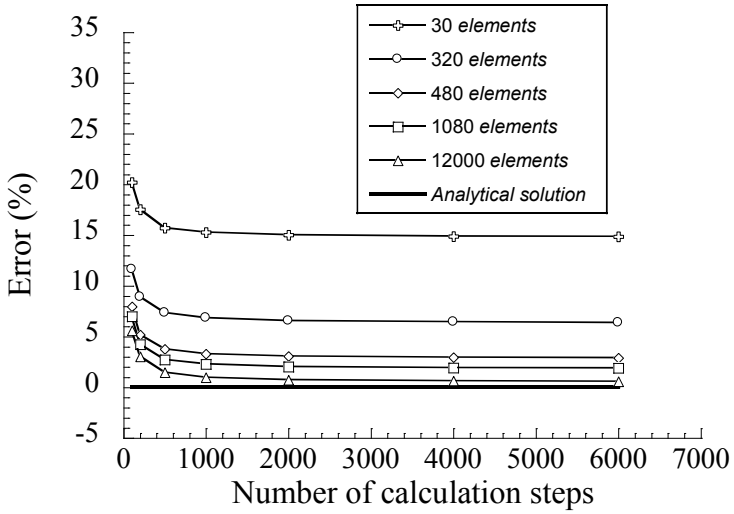

Figure A- 12: Error of ultimate bearing capacity when compared with Prandtl's solution by von Mises model & FEM with modified B-bar method

First of all, the performance of the traditional FEM when using quadrature 4nodes isoparametric element is analyzed with the strip footing bearing capacity problem. As can be observed from Figure A- 9, the bearing capacity is continuously increased along with the footing displacement. Although the number of elements is significantly increased form 1080 elements to 12000 elements, the error

compared to the analytical solution is reduced from 275% to on around 45% compared to the exact solution (Figure A-11). Even though up to 12000 elements is used, the solution is still far away from the analytical solution. This is due to volumetric locking problem as presented in Chapter 4. Thus, from this analysis, we can see that the traditional FEM cannot be used to observe the ultimate bearing capacity as well as the correct failure surface.

On the other hand, modified B-bar approach in FEM significantly improved the calculation result, in which the ultimate bearing capacity showed a good convergence to the analytical solution (Figure A- 11) as the number of elements increased. The simulation results were only around 2% and 0.5% different from the analytical result corresponding to the number of elements 1080, 12000, respectively (Figure A- 12). Furthermore, the failure surface in general failure model as shown by Prandtl could also be obtained by this B-bar method as seen in Figure A- 13. The displacement of the ground, as well as the principle stresses, was shown in Figure A- 14.

The above FEM simulation results proved the effectiveness of modified B-bar method in solving the volumetric locking problem of bearing capacity of strip footing with elastoplastic model. Simulation results were in good agreement with Prandtl's analytical solution

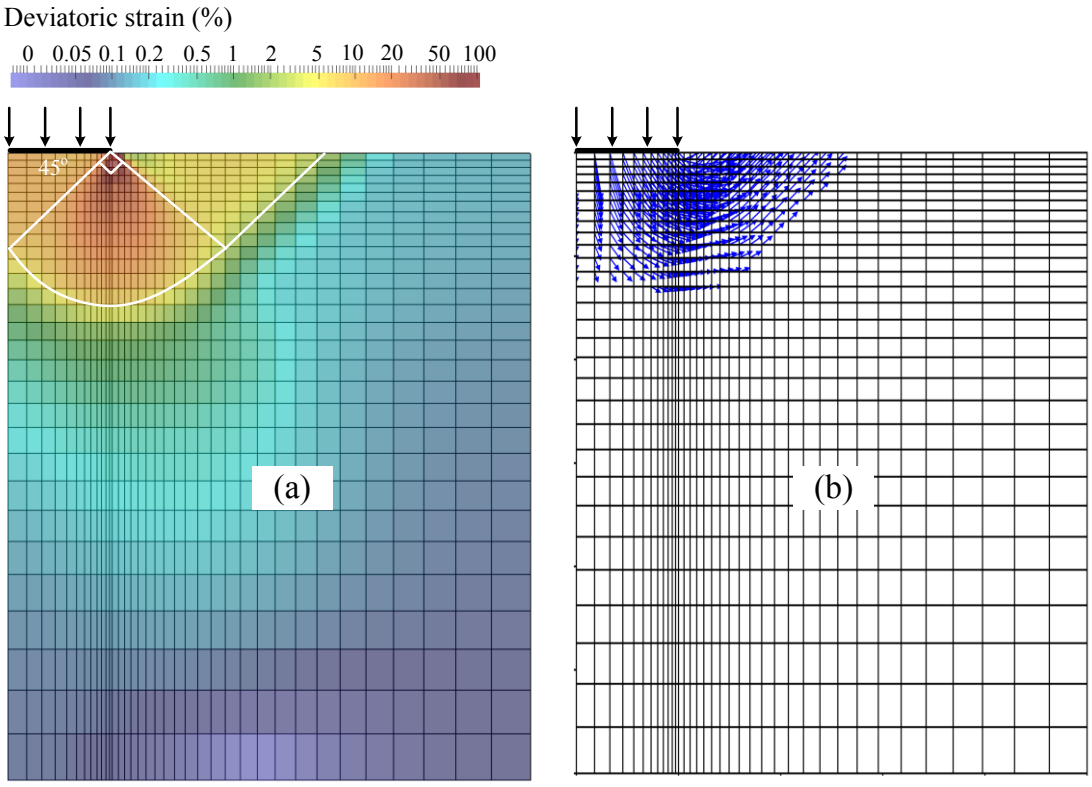

Figure A- 13. FEM analysis result of strip footing bearing capacity using von Mises criteria with a mesh of 1080 elements:
(a) Deviatoric strain distribution (b) Displacement vector (scale 4 times)

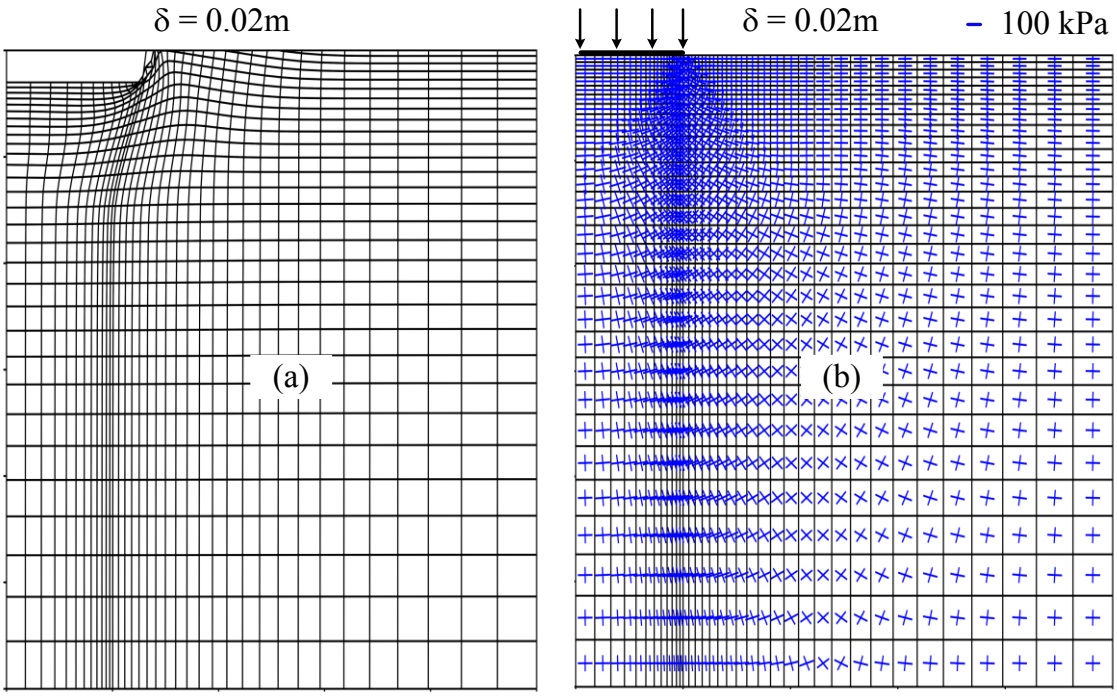

Figure A- 14: FEM analysis result of strip footing bearing capacity using von Mises criteria with a mesh of 1080 elements:
(a) Grid displacement after loading (scale 4 times)(b) Principle stresses distribution

B- Calculating grading index I_G based on stress values:

We can directly obtain grading index I_G value from the soil's stress values after crushing has been occured.

Equation of crushing surface (Equation 2-10):

$$f_x = lnp + \frac{2}{\alpha} ln\left\{1 + \left(\frac{q}{pM_x}\right)^{\alpha}\right\} - lnp_x \tag{B-1}$$

When particle crushing occurs, $f_x = 0$, which leads to :

$$p_x = p\left[1 + \left(\frac{q}{pM_x}\right)^{\alpha}\right]^{\frac{2}{\alpha}} \tag{B-2}$$

At the time of loading, unloading and reloading process, stress magnitude can fluctuate. Crushing stress can be calculated as the maximum of the left hand side of Eq. (B-2):

$$p_x = Max\left(p\left[1 + \left(\frac{q}{pM_x}\right)^{\alpha}\right]^{\frac{2}{\alpha}}\right) \tag{B-3}$$

Then, from the equation of I_G:

$$I_G = 1 - exp\left(-\frac{p_x - p_{x0}}{p_r}\right) \tag{B-4}$$

Therefore, after the initialization of crushing, I_G can be calculated directly from stress magnitude:

$$I_G = 1 - exp\left(-\frac{Max\left(p\left[1 + \left(\frac{q}{pM_x}\right)^{\alpha}\right]^{\frac{2}{\alpha}}\right) - p_{x0}}{p_r}\right) \tag{B-5}$$

In which p_{x0}, p_r, M_x, α are constant material parameters for a specific soil.

C- Matching Drucker-Prager a d Mohr Coulomb criteria in plane strain condition:

C1. Extended Coulomb's criteria:

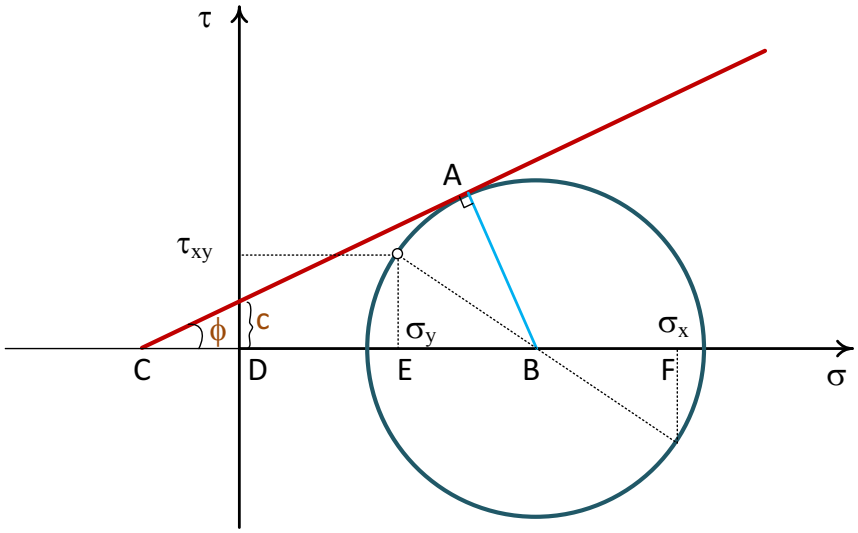

Figure C-1: Mohr-Coulomb yield criteria

We can derive the extended Coulomb's criteria by calculating $sin\Phi$ from Figure C-1:

$$sin\Phi = \frac{AB}{CD + DB} = \frac{\left[\left(\frac{\sigma_x - \sigma_y}{2}\right)^2 + \tau_{xy}^2\right]^{1/2}}{c\frac{cos\Phi}{sin\Phi} + \frac{\sigma_x + \sigma_y}{2}} \tag{C-1}$$

Thus, the extended Coulomb's criteria can be written in this form

$$\left[\left(\frac{\sigma_x - \sigma_y}{2}\right)^2 + \tau_{xy}^2\right]^{\frac{1}{2}} = \mathrm{c}.cos\phi + \frac{\sigma_x + \sigma_y}{2} sin\Phi \tag{C-2}$$

C2. Drucker-Prager:

C2.1 Yield criteria:

$$f = -\alpha I_1 + J_2^{1/2} - k \tag{C-3}$$

Where α and k are positive constants of the material.

$I_1$is the sum of principle stresses: (note that in soil mechanics, compressive stress is assumed to be positive)

$$I_1 = \sigma_{xx} + \sigma_{yy} + \sigma_{zz} \tag{C-4}$$

$J_2$is the second invariant of the stress deviation:

$$J_2 = \frac{1}{6}\left[\left(\sigma_{xx} - \sigma_{yy}\right)^2 + \left(\sigma_{yy} - \sigma_{zz}\right)^2 + (\sigma_{zz} - \sigma_{xx})^2\right] + \tau_{xy}^2 + \tau_{yz}^2 + \tau_{zx}^2 \tag{C-5}$$

C2.2 Flow rule:

Associated flow rule is assumed in this model.

$$\dot{\varepsilon}_{ij}^p = \Lambda \frac{\partial f}{\partial \sigma_{ij}} \tag{C-6}$$

Substituting (C-4) into (C-7)

$$\dot{\varepsilon}_{ij}^p = \Lambda \left[\alpha \delta_{ij} + \frac{s_{ij}}{2} J_2^{1/2}\right] \tag{C-7}$$

C3 Matching Drucker Prager and to Mohr Coulomb criteria in plane strain:

If the Drucker-Prager and Coulomb criteria are expected to give identical plastic collapse loads for the plane strain case, then two conditions need to be met: (1) same limit load, and (2) plane strain. In the case of plane strain condition, with the out of plane direction "z", then $\varepsilon_{zz}, \varepsilon_{xz}, \varepsilon_{yz}$ vanish. Furthermore, to derive the form of Drucker-Prager criterion in a plane strain condition, perfectly plastic behavior is assumed. This means that at the instant of collapse, the strain rates are purely plastic. This is because, in most problems of elasticity, that changes in geometry are negligible.

From Eq. (C-7):

$$\dot{\varepsilon}_{xz} = \lambda\left(\alpha\delta_{xz} + \frac{s_{xz}}{2J_2^{1/2}}\right) = 0 \;;\; (\delta_{xz} = 0) \Rightarrow s_{xz} = \tau_{xz} = 0 \tag{C-8}$$

$$\dot{\varepsilon}_{yz} = \lambda\left(\alpha\delta_{yz} + \frac{s_{yz}}{2J_2^{1/2}}\right) = 0;\; \left(\delta_{yz} = 0\right) \Rightarrow s_{yz} = \tau_{yz} = 0 \tag{C-9}$$

$$\dot{\varepsilon}_{zz} = \left(\alpha\delta_{zz} + \frac{s_{zz}}{2J_2^{1/2}}\right) = 0;\; (\delta_{zz} = 1) \Rightarrow s_{zz} = 2\alpha J_2^{1/2} \tag{C-10}$$

From the definition of s_{zz}:

$$s_{zz} = \sigma_{zz} - \frac{\sigma_{xx} + \sigma_{yy} + \sigma_{zz}}{3} \tag{C-11}$$

From (C-11) and (C-10):

$$\sigma_{zz} = -3\alpha J_2^{\frac{1}{2}} + \frac{\sigma_{xx} + \sigma_{yy}}{2} \tag{C-12}$$

Substituting (C-12) into (C-4):

$$I_1 = \frac{3}{2}(\sigma_{xx} + \sigma_{yy}) - 3\alpha J_2^{1/2} \tag{C-13}$$

Substituting (C-8), (C-9) and (C-12) into (C-5):

$$J_2 = \left[\left(\frac{\sigma_{xx} - \sigma_{yy}}{2}\right)^2 + \tau_{xy}^2\right]/(1 - 3\alpha^2) \tag{C-14}$$

Substituting (C-13) and (C-14) into the yield function (C-3):

$$f = -3\alpha\frac{\sigma_x + \sigma_y}{2} + (1 - 3\alpha^2)J_2^{1/2} - k \tag{C-15}$$

At failure state, $f = 0$, Eq. (C-15) becomes:

$$\frac{k}{(1 - 3\alpha^2)^{1/2}} = -\frac{3\alpha}{(1 - 3\alpha^2)^{1/2}}\frac{\sigma_x + \sigma_y}{2} + \left[\left(\frac{\sigma_x - \sigma_y}{2}\right)^2 + \tau_{xy}^2\right]^{1/2} \tag{C-16}$$

Or we can rewrite Eq. (C-16) in the following form:

$$\left[\left(\frac{\sigma_x - \sigma_y}{2}\right)^2 + \tau_{xy}^2\right]^{1/2} = \frac{k}{(1 - 3\alpha^2)^{1/2}} + \frac{3\alpha}{(1 - 3\alpha^2)^{1/2}}\frac{\sigma_x + \sigma_y}{2} \tag{C-17}$$

Yield function of Drucker-Prager(Eq. C-17) becomes identical with Yield function of Mohr-Coulomb (Eq. C-2) we set:

$$sin\Phi = \frac{3\alpha}{(1 - 3\alpha^2)^{1/2}} \tag{C-18}$$

$$c\ cos\Phi = \frac{k}{(1 - 3\alpha^2)^{1/2}} \tag{C-19}$$

Solving (C-18, C-19), we get:

$$\alpha = \frac{sin\phi}{\sqrt{3}\sqrt{3 + sin^2\phi}} \tag{C-21}$$

Substituting (C-20) into (C-19), k is obtained:

$$k = \frac{\sqrt{3}c.cos\phi}{\sqrt{3 + sin^2\phi}} \tag{C-22}$$